

Self-assembly of amino acids on noble metal surfaces:
morphological, chemical and electronic control of matter
at the nanoscale

by

Agustin Schiffrin

Physics Diploma, Ecole Polytechnique Fédérale de Lausanne, 2003

A THESIS SUBMITTED IN PARTIAL FULFILMENT OF
THE REQUIREMENTS FOR THE DEGREE OF
DOCTOR OF PHILOSOPHY

in

The Faculty of Graduate Studies

(Chemistry)

THE UNIVERSITY OF BRITISH COLUMBIA

April 30, 2008

© Agustin Schiffrin, 2008

Abstract

Designing novel nanostructures which exploit the self-assembly capabilities of biomolecules yields a promising approach to control matter at the nanoscale. Here, the homochiral molecular self-assemblies of the methionine and tyrosine amino acids on the monocrystalline Ag(111) and Cu(111) surfaces are characterized by means of scanning tunneling microscopy (STM) and spectroscopy (STS), helium atom scattering (HAS), x-ray photoelectron spectroscopy (XPS) and near-edge x-ray absorption fine structure (NEXAFS) in ultrahigh vacuum (UHV). On Ag(111), methionine self-assembles into supramolecular chains following the $\langle 110 \rangle$ substrate axis, forming regular nanogratings with tunable periodicity. Within the nanowires, a zwitterionic dimerization scheme is revealed. STS shows that the biomolecular nanostructures act as tunable one-dimensional quantum resonators for the surface state electrons. Zero-dimensional electronic confinement is achieved by positioning single iron atoms in the molecular trenches. This shows a novel approach to control the dimensionality of surface state electrons. The nanogratings were exploited to steer the spontaneous one-dimensional ordering of cobalt and iron atoms. For $T > 15$ K, the metal species self-align into homogeneously distributed chains in between the biomolecular trenches with ~ 25 Å interatomic distance. For Co, the dynamics of the self-alignment was monitored, revealing a reduced mobility in comparison with isolated Co atoms

on bare Ag(111). On Cu(111), the self-assembly of methionine is influenced by the substrate reactivity and its temperature during molecular deposition. For $T < 273$ K, the biomolecules assemble in anisotropic extended clusters oriented with a -10° rotation off the $\langle 110 \rangle$ substrate orientations, whereas above 283 K a regularly ordered 1D phase arises with a $+10^\circ$ rotation off these high-symmetry axis. XPS reveals a structural transformation triggered by a thermally activated deprotonation of the zwitterionic ammonium group. On Ag(111), tyrosine self-assembles above a critical temperature into linear structures primarily following the substrate crystalline symmetry. A zwitterionic non-covalent molecular dimerization is demonstrated, NEXAFS data providing evidence of a non-flat adsorption of the phenyl ring. This recalls the geometrical pattern of methionine on Ag(111) and supports a universal self-assembling scheme for amino acids on close-packed noble metal surfaces, the different mesoscopic ordering being determined by the side chain reactivity.

Contents

Abstract	ii
Contents	iv
List of Tables	viii
List of Figures	ix
Acknowledgements	xii
1 Introduction	1
1.1 'Top-down' nanofabrication processes	1
1.2 The molecular self-assembly paradigm	4
1.3 The advent of Scanning Tunneling Microscopy (STM)	7
1.4 Thesis overview	11
2 Experimental methods	15
2.1 Scanning Tunneling Microscopy (STM) and Spectroscopy (STS)	16
2.1.1 STM theory	16
2.1.2 Scanning tunneling spectroscopy (STS)	23
2.1.3 Investigating adsorbates on metal surfaces with STM	28
2.1.4 The STM experimental setup	33

2.1.5	Preparation procedures	37
2.2	Complementary surface science techniques	41
2.2.1	Helium Atom Scattering (HAS)	41
2.2.2	X-ray Photoelectron Spectroscopy (XPS)	44
2.2.3	Near-Edge X-ray Absorption Fine Structure (NEXAFS)	50
3	Methionine on Ag(111)	56
3.1	Introduction	57
3.2	Experimental section	59
3.3	Results and discussion	62
3.3.1	Mesoscopic ordering and spectroscopic signature	62
3.3.2	Molecular-level observations	72
3.3.3	Modeling the zwitterionic coupling scheme	78
3.4	Conclusion	83
4	Electron confinement in <i>L</i>-methionine nanogratings	85
4.1	Introduction	85
4.2	Experimental section	87
4.3	Results and discussion	88
4.3.1	1D electronic confinement by self-assembled biomolec- ular nanogratings	88
4.3.2	Zero-dimensional electron confinement by Fe adatoms .	97
4.4	Conclusion	100
5	Adatom self-alignment in <i>L</i>-methionine nanogratings	101
5.1	Introduction	101
5.2	Experimental section	104

5.3	Results and discussion	105
5.3.1	Non-random 1D self-alignment of metal adatoms . . .	105
5.3.2	Dynamics and statistics of the self-alignment process .	110
5.3.3	Influence of the substrate electronic properties on the adatom self-ordering phenomenon	115
5.4	Conclusion	119
6	<i>L</i>-methionine on Cu(111)	121
6.1	Introduction	122
6.2	Experimental section	124
6.3	Results and discussion	126
6.3.1	Thermally activated enantiomorphic orientational switch	126
6.3.2	Correlation with a catalytically induced heterogeneous ammonium deprotonation	129
6.3.3	Molecular arrangement in the ordered high tempera- ture anionic phase	133
6.4	Conclusion	140
7	<i>L</i>-tyrosine on noble metal surfaces	141
7.1	Introduction	142
7.2	Experimental section	145
7.3	Results and discussion	146
7.3.1	Mesoscopic biomolecular self-assembly into two-dimensional zwitterionic nanoribbons	146
7.3.2	NEXAFS measurements	151

7.3.3	Molecular arrangement within the nanoribbons: zwitterionic coupling scheme	155
7.4	Conclusion	158
8	Outlook	160
9	Publications	165
	Bibliography	168

List of Tables

3.1	C 1s NEXAFS data for <i>L</i> -methionine on Ag(111)	72
7.1	C 1s NEXAFS data for <i>L</i> -tyrosine on Ag(111)	154

List of Figures

1.1	'Top-down' nanofabrication techniques	3
1.2	The tobacco mosaic virus	5
1.3	The molecular self-assembly paradigm	7
1.4	STM capabilities	9
1.5	The methionine and tyrosine amino acids	12
2.1	Principles of STM	18
2.2	STM head and sample holder	35
2.3	LT-STM and custom-built UHV chamber	36
2.4	STM setup at AMPEL	38
2.5	W tip eletrochemical etching	39
2.6	Schematic of the HAS setup geometry	45
2.7	X-ray Photoelectron Spectroscopy	46
2.8	NEXAFS diagram	52
3.1	The <i>L</i> -methionine amino acid	59
3.2	1D ordering of <i>L</i> -methionine on Ag(111)	63
3.3	Tuneable 1D <i>L</i> -methionine nanogratings	65
3.4	Statistics of the nanogratings spacing regularity	67
3.5	N 1s and O 1s XPS of <i>L</i> -methionine on Ag(111)	69
3.6	C 1s NEXAFS measurements of <i>L</i> -methionine on Ag(111)	71

3.7	High resolution STM of <i>L</i> -methionine on Ag(111)	73
3.8	Quadruple <i>L</i> -methionine stripes	75
3.9	Enantiomorphic biomolecular self-assembly	77
3.10	2D commensurate <i>L</i> -methionine layer structure on Ag(111) . .	79
3.11	Molecular mechanics total energy maps for <i>L</i> -methionine system on Ag(111)	81
4.1	Confinement of the Ag(111) 2DEG by self-assembled molecular gratings and Fe atoms	90
4.2	Quantum-well states in a molecular resonator	94
4.3	Free electron propagation along molecular walls	96
4.4	Zero-dimensional electron confinement in a quantum corral . .	98
5.1	The methionine biomolecular nanogratings on Ag(111) and the influence on the substrate electronic structure	106
5.2	Adatom 1D self-alignment in between methionine biomolecular chains	109
5.3	Temperature dependence of Co adatom hopping rates	113
5.4	Statistics of adatom-chain and nearest-neighbor adatom-adatom distances methionine trenches	114
5.5	Confinement of surface electrons in a methionine supramolecular nanostructures with Co adatoms	116
5.6	<i>Ab initio</i> calculations of the interaction energy between Fe and Co adatoms and a quantum resonator	118
6.1	STM topographs of <i>L</i> -methionine on Cu(111)	127
6.2	HAS data of <i>L</i> -methionine on Cu(111)	129

6.3	N1s XPS of <i>L</i> -methionine on Cu(111)	131
6.4	Molecular coverage dependence of the N 1s XPS signature of <i>L</i> -methionine on Cu(111)	134
6.5	Molecular resolution STM data of <i>L</i> -methionine on Cu(111)	137
6.6	MM+ molecular mechanics calculations for the β -phase	139
7.1	STM topographs of <i>L</i> -tyrosine on Ag(111) and Cu(111)	148
7.2	N 1s and O 1s XPS for the <i>L</i> -tyrosine/Ag(111) system	152
7.3	C 1s NEXAFS measurements of <i>L</i> -tyrosine on Ag(111)	153
7.4	High resolution STM data of <i>L</i> -tyrosine on Ag(111)	157

Acknowledgements

First of all, I would like to thank my supervisor, Dr. Johannes V. Barth, for giving me the chance to work in this interesting project and in a stimulating environment. His support and expertise in the field of STM and general surface science were of great help all along these years. I am extremely thankful to Dr. A. Riemann, Dr. W. Auwärter, Dr. J. Reichert, Dr. Y. Penec, A. Weber-Bargioni, G. Jahnz, E. Varene, M. Marshall, M. Eichberger and R. Carron from our STM group, not only for their professional support, but also for creating such a pleasant work atmosphere. In particular, thanks to Dr. A. Riemann and Dr. W. Auwärter for teaching me everything about the STM setup at AMPEL and for their inspiring experimental savoir-faire, to Dr. J. Reichert for a fruitful collaboration and his rigorous scientific approach, Dr. Y. Penec for his natural professional spontaneity and Alex Weber-Bargioni for the stimulating science discussions and the good times spent outside the lab in the mountains or sharing his passion for italian cooking.

I am also very thankful to Dr. K. Kern for supporting the initial stage of my PhD project at EPFL, Switzerland, and to Dr. S. Clair for introducing me to STM.

Furthermore, I would like to thank the members of my PhD committee Dr. M. Shapiro and Dr. H. Li for evaluating my work, and specially Dr.

D. Bizzotto for reading and correcting this thesis. Also, thanks to Dr. G. Sawatsky for his time and availability to discuss scientific issues. In summary, many thanks to the whole AMPEL team with whom I shared daily world-class coffee thanks to the state-of-the-art espresso setup developed by Dr. W. Hardy.

I am very grateful to Dr. A. Morgante, Dr. D. Cvetko, Dr. A. Cossaro, Dr. L. Floreano, Dr. G. Bavdek and M. Dell'Angela from the ALOISA beamline at the ELETTRA synchrotron light source in Trieste, Italy, for their extensive expertise in XPS, NEXAFS and HAS, their constant motivation and good humor.

Moreover, I thank Dr. V.S. Stepanyuk, Dr. L. Niebergall and Dr. P. Bruno from the Max Planck Institute in Halle, Germany, for their theoretical contribution in the calculation of the interaction energy in the metal adatom-quantum resonator system in Chapter 5. Also, I would like to acknowledge Dr. R. Fasel for the computational procedures for the classical molecular mechanics calculations.

Last but not least, I want to dedicate this thesis to my family, specially to my parents and grandparents, who always encouraged me to follow my true motivations.

This work was supported by the Canada Foundation for Innovation, the Natural Science and Engineering Research Council of Canada, and the British Columbia Knowledge Development Fund.

Chapter 1

Introduction

'... we are control freaks...'

D. Eigler

1.1 'Top-down' nanofabrication processes

Since the beginning of civilization, cultural evolution has been closely linked to technological innovation and the development of new functional devices. From the Bronze Age to Gutenberg's invention of the mechanical printing procedure, from the design of the steam engine which led to the Industrial Revolution to the more recent Silicon Era, the discovery of new technical processes has accompanied our concept of Progress. The unprecedented technological advancements which we have witnessed during the last 50 years are directly linked to the design of semiconducting devices and the advent of the silicon chip. The exponential improvement in terms of performance that these digital systems underwent from the early days to the present, were enabled by a systematic increase of the density of transistors and magnetic memory bits, increase only rendered possible by a constant miniaturization trend of such functional units. In the commencement of the digital era, the density of transistors on an integrated chip doubled every two years, this empirical exponential trend becoming what we commonly call Moore's Law

[1] and which has been accurately followed until nowadays.

Currently, standard ways of mass-producing such low-scale components consist in 'top-down' fabrication techniques where the surface of the raw material is patterned and sculptured by removing amounts of material: the initial macroscopic raw material is treated in order to obtain a final low-scale functional unit. At the industrial level, photolithography is a common 'top-down' microfabrication process, where a light beam selectively patterns a substrate by using a photo-sensitive material and where the scale of the obtained features is limited by the light wavelength and numerical aperture. Still at a research status, state-of-the-art lithographic processes can overcome these limits either by increasing the numerical aperture of the light beam, as it is the case in immersion photolithography where features in the order of 40 nm can be obtained [2–4], or by decreasing the wavelength of the patterning beam. The later can be achieved by using an electron beam, as in electron-beam lithography [5–9], or by considering x-ray radiation [2]. By means of these techniques, features in the order of several tens of nm can be successfully fabricated, as seen in Fig. 1.1. Another example of patterning at these scales is nanomachining, which allows the production of regular and low-scaled features by locally steering chemical reactions [10] (see Fig. 1.1(d)).

If these standard miniaturization techniques have so far been able to keep up with Moore's Law's predictions, they will soon reach their own limitations due to new physical phenomena intrinsically arising from the systems' low-scale. In fact, beyond a critical threshold, new quantum effects take place due to the restraining geometrical boundary conditions which have to be satisfied by the solution of the system's Schrödinger's equation: at the nanoscale,

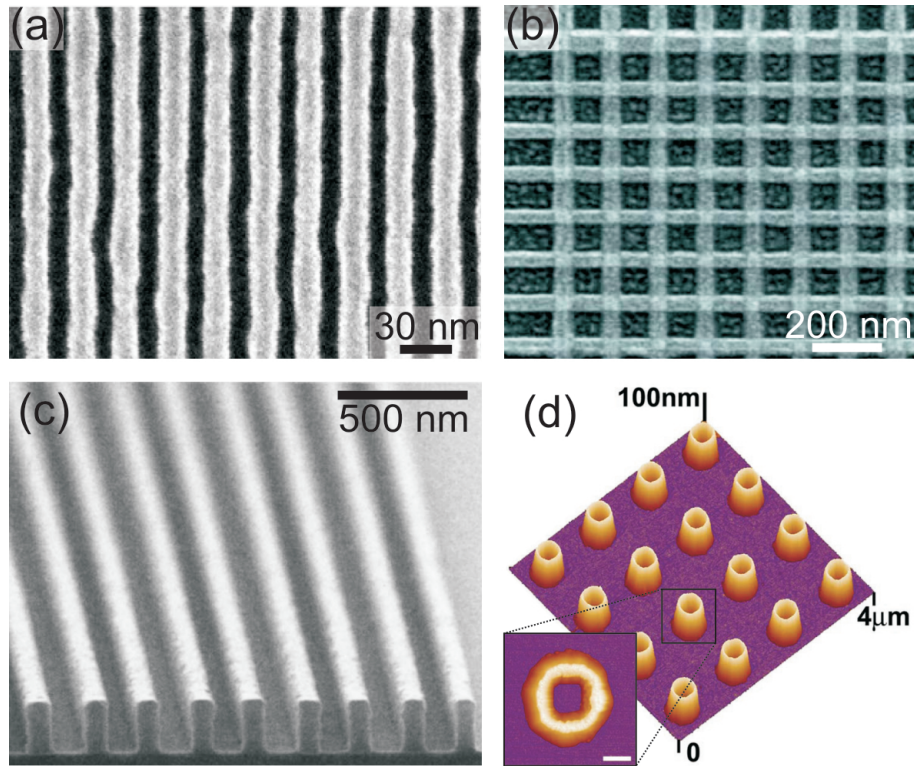


Figure 1.1: State-of-the-art electron-beam lithography, immersion photolithography and chemical nanomachining. (a) Scanning electron micrograph (SEM) of a 30 nm-pitch Si nanowire array obtained by nanoimprint and electron-beam lithography. Reproduced with permission from [6]. (b) SEM of an 8×8 130-nm pitch grid of Pt/Ti bilayer nanowires with potential use for a high-density molecular memory device, obtained by nanoimprint and e-beam lithography. Reproduced from [9] with kind permission from Springer Science+Business Media. (c) SEM picture of a photoresist for immersion photolithography. Reproduced with permission from [4]. (d) Atomic Force Microscopy (AFM) images of an array of Si rings on an insulating SiO₂ layer obtained by chemical nanomachining. Reprinted with permission from [10]. Copyright 2007 American Chemical Society. Scale bar in the inset: 200 nm.

the physical properties become dramatically influenced by the geometrical extension of the system. For instance, a magnetic memory bit requires a

minimum number of atoms to resist thermal fluctuations, and SiO₂ clusters need a minimum size to remain insulating [11]. Therefore, the control of matter at the sub-10-nm scale requires new materials, and most of all, new nanofabrication processes.

An alternative to the techniques mentioned above for the prospective mass production of functional nanodevices consists in 'bottom-up' approaches, whereby specific atoms and molecules are considered as building units for more complex entities. For instance, the idea of conceiving a single-molecule electronic device that would avoid the scale limitations of the silicon-based integrated circuits has been in minds for more than 30 years already [12]. On the other hand, the advent of scanning tunneling microscopy, which will be discussed later, has enabled single atom manipulation [13]. However, mass production and reliable functionality of molecular nanosystems are still far from being achieved. Homogeneous nanostructuring at surfaces in a controlled 'bottom-up' fashion and in a commercially viable way that could compete with lithographic methods is still an open technological challenge [14, 15].

1.2 The molecular self-assembly paradigm

Pioneering work by A. Klug *et al.* fifty years ago allowed elucidating the basic biochemical processes that drive the specific supramolecular aggregation into more complex biological entities with specific functionalities [16, 17]. The probability that millions of molecules randomly self-aggregate into a specific supramolecular arrangement in a precise order, reversibly and repeatedly, is statistically null. However, reversible non-covalent interactions [18] between

the molecular units drive an intermolecular recognition mechanism which enables a specific self-assembly process into a functional virus [19–21]. As an example, the structure of the tobacco mosaic virus [16, 17, 22] (see Fig. 1.2) is determined by a self-recognition process between peptidic units and specific binding-sites on a RNA strand. This allows the self-assembly of the different units into a well-defined helix-shaped supramolecular complex.

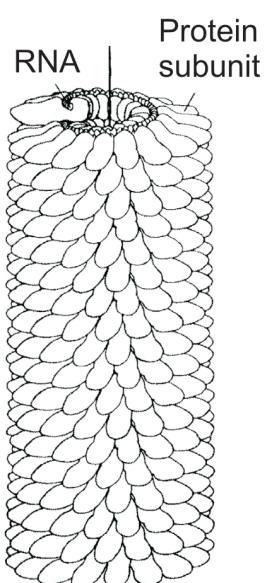


Figure 1.2: Molecular recognition and self-assembly in biological systems: diagram of the RNA-protein complex determining the structure and functionality of the tobacco mosaic virus, as discovered by Klug *et al.*. Reprinted with permission from [17].

The understanding of such fundamental biochemical processes at the molecular scale permits the definition of a new paradigm towards 'bottom-up' control of matter at the nanoscale. This concept, inspired by the basic order phenomena governing the structure of biomolecular systems, is based on non-

covalent synthesis and molecular recognition for the fabrication of functional nanostructures [23–27]. The approach aims to imitate the processes that allow in nature to gain functionalities at the molecular level [28]. It consists in a predefined selection of the molecular building units, the surrounding environment and a set of macroscopic controlling parameters whose configuration at equilibrium yields a supramolecular structure with the desired shape and functionality [29–32]. In two dimensions, this method supports potential pathways for the nanopatterning of surfaces at the molecular and atomic level, by choosing a judicious set of supporting surface and adsorbed species at appropriate deposition conditions [15]. Here, a balanced interplay between adsorbate diffusive processes, intermolecular forces, substrate-adsorbate and deposition conditions such as evaporation rate and substrate temperature defines the equilibrium configuration of the supramolecular ensemble (see Fig. 1.3).

Therefore, through this bioinspired molecular self-assembly approach, nanofabrication processes which go beyond the scale limitations imposed by the current 'top-down' techniques can be realized. On surfaces, the understanding of the molecular-recognition mechanism is not only interesting for such biomimetic purpose, but its unravelling can lead to the development of biocompatible materials necessary for the design of future biosensors or implants [33]. From a more general perspective, the resolution of basic physical and chemical processes on solid surfaces at the molecular level and their correlation with macroscopic interfacial phenomena is of fundamental interest in the field of surface science, as shown by studies from Ertl, the current Nobel Prize winner in Chemistry [34, 35].

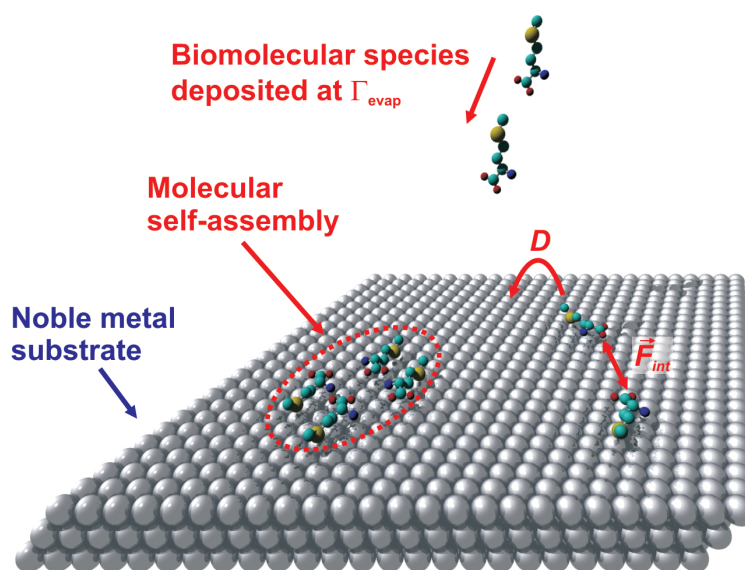


Figure 1.3: Diagram of the 'bottom-up' molecular self-assembly approach: an ensemble composed of a supporting substrate, molecular and atomic deposition species at given macroscopic conditions yields potential for functional supramolecular self-assembly. The equilibrium configuration is driven by the balance between transport, molecular rotation, intermolecular forces, substrate-adsorbate interactions and deposition conditions.

1.3 The advent of Scanning Tunneling Microscopy (STM)

If self-assembly provides the conceptual paradigm for new nanofabrication pathways, a technical tool for the control and observation at such scales is still required for concrete applications. The invention in 1982 by Binnig and Rohrer of scanning tunneling microscopy (STM) represented without a doubt a major breakthrough in microscopy and surface science techniques [36] and provided a perfectly adapted tool for the study of adsorbates on surfaces at

the nanoscale. This apparatus exploits the quantum mechanical tunneling effect according to which electrons are able to tunnel from one electrically conducting electrode to another when these are separated by small distances, usually between 5 to 10 Å. This tunneling electric current is generally of the order of 1 nA and decays exponentially with respect to the distance that separates both surfaces. Therefore, by scanning a metallic tip over a sample surface and measuring the current between the two surfaces, it is possible to obtain topographic information of the sample in real space with unprecedented vertical resolutions below 0.1 Å.

Developed in 1951, field ion microscopy (FIM) was the first microscopic method providing true atomic resolution data of transition metal surfaces by applying electric fields of the order of 10^{11} V/m [37]. However, this technique is mostly restricted to imaging of sharp metallic tips and shows therefore limited versatility. The advantages of STM with respect to other surface science techniques resides in the non-destructive measurement (which can be a problem with electron microscopy and FIM) and the locality of the obtained data, which allows the observation of individual atoms and molecules (in contrast with diffraction techniques such as low-energy electron diffraction (LEED), x-ray diffraction (XRD) or helium atom scattering (HAS) which only allow mapping of the reciprocal space and require a periodic order of the observed system). Most of all, its main asset consists in its atomic scale resolution capabilities: Fig. 1.4 represents an STM image of the atomically-resolved Si(111) surface with its (7×7) reconstruction. This image is reproduced from work from Binnig *et al.* [38] and represents the first atomically-resolved reconstructed surface in real space.

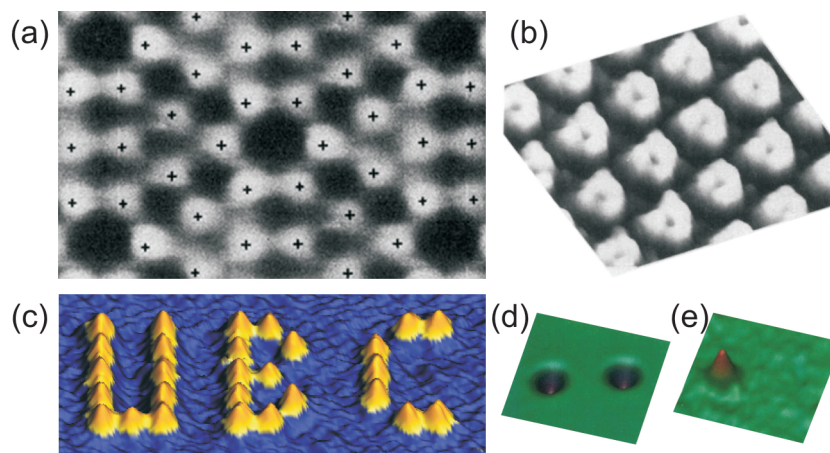


Figure 1.4: Capabilities of scanning tunneling microscopy (STM) and spectroscopy (STS). (a) STM topograph of the atomically resolved Si(111)- 7×7 reconstructed surface as obtained first by Binnig *et al.* in 1983. Each cross represents a Si adatom. Reprinted figure with permission from [38]. Copyright 1983 by the American Physical Society. (b) STM topographic images of carbon monoxide and benzene coadsorbed on Rh(111). Each threefold ringlike feature is a benzene molecule lying flat on the substrate. The CO molecules are not resolved. Reprinted figure with permission from [39]. Copyright 1988 by the American Physical Society. (c) Single molecule manipulation with STM: CO molecules adsorbed on a Cu(111) surface at 4 K are positioned with the STM tip in order to spell UBC, standing for the University of British Columbia. Each yellow protusion represents a CO molecule. In constant-current STM topographs, CO molecules on Cu(111) naturally appear as holes: here, the image was treated in order to image each CO molecule as a yellow protusion. Letters are 2 nm wide. (d) and (e) Chemical imaging by means of inelastic scanning tunneling spectroscopy: in (d), one is not able on a constant-current STM topograph to differentiate between acetylene (C_2H_2 , left) and deuterated acetylene (C_2D_2 , right) molecules, whereas the d^2I/dV^2 spectroscopic data obtained with a bias voltage of 358 mV in (e) provides chemical resolution and only images the non-deuterated C_2H_2 species. From [40]. Reprinted with permission from AAAS.

A prerequisite of STM is that the studied substrate is a conductor or a semiconductor. However, electrons are still able to tunnel through thin insulating films by resonant tunneling, enabling the visualization of organic molecular adsorbates on metallic surfaces. Benzene molecules coadsorbed with carbon monoxide (CO) on the Rh(111) surface were one of the first systems where organic species were imaged with STM (see Fig. 1.4(b)).

The tip of the microscope is not only useful as an electrode, but it can also be considered as a nanoprobe to position atoms and molecules on the surface in a controllable fashion and with atomistic precision. This manipulation procedure was first demonstrated by Eigler *et al.* with Xe atoms on Ni(110) [13]. Figure 1.4(c) shows how the position of single CO molecules on a Cu(111) surface is controlled at 4 K by manipulating with the STM tip: each yellow protusion represents a CO molecule adsorbed on a 'top' site of the substrate. In constant-current STM topographs, CO molecules adsorbed on Cu(111) appear as holes and not protusions: here, the image was treated in order to inverse the appearance of the adsorbed species.

Whereas the exponential decay of the tunneling current with respect to the tip-sample distance allows accessing topographic information, the tunneling current itself is directly dependent on the electronic structure of the observed system. For instance, the conductance of the tunnel junction (i.e. the first derivative of the current) bears information on the electronic local density of states of the sample. Therefore, the apparatus developed by Binnig *et al.* has not only microscopical, but also spectroscopic functions: not only the topography of the system can be addressed, but also its electronic properties. With respect to molecular species on the surface, STM can even

yield chemical mapping of organic adsorbates: the tunneling electrons can excite the vibrational modes of the adsorbed species by inelastic scattering. The electron energy loss being extremely sensitive to the chemical nature of the excited mode, the tunneling signal can contain local information of the chemistry of the system. This approach, developed by Ho *et al.*, is depicted in Fig. 1.4(d) and 1.4(e) [40]: while in 1.4(d) we observe the topographic STM image of two indiscernible adsorbed acetylene molecules, in 1.4(e) the mapping of the same region with the second derivative of the tunneling signal allows to differentiate a normal acetylene molecule from a deuterated one. These aspects make STM an unmatched tool for probing locally the topographic, electronic and chemical properties of adsorbed species on metal substrates.

1.4 Thesis overview

The main topic addressed in this thesis is the investigation and characterization of the two-dimensional molecular self-assembly of biologically relevant species on noble metal surfaces. More specifically, we will consider the case of the amino acids methionine and tyrosine on the closed-packed noble metal surfaces Ag(111) and Cu(111). Like nucleic acids, amino acids are in general an interesting class of molecules as they represent the basic elements of living organisms, and therefore, through their inherent self-assembly and molecular-recognition capabilities, they automatically qualify as potential building units for the prospective non-covalent synthesis of functional nanostructures. Among the 20 natural amino acids, methionine and tyrosine (see Fig. 1.5) have been selected due to the interesting chemical reactivity prop-

erties of their side-chains. Methionine and tyrosine, through the sulfur atom, and through the phenyl and hydroxyl groups respectively, are suspected to bind in physiological conditions to metal ions, inducing conformational and thus functional changes in specific peptide chains [41–43]. Hence, their study carries also some fundamental significance concerning their role in biological systems.

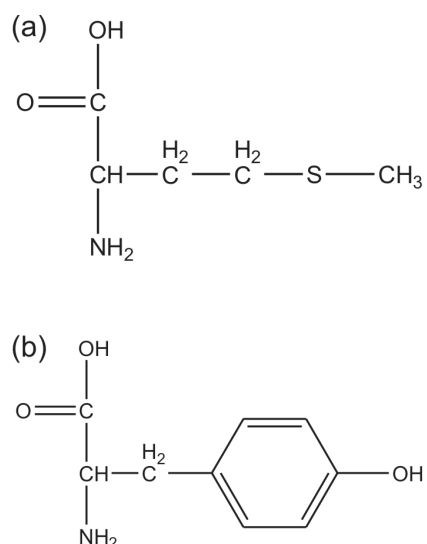


Figure 1.5: Chemical structures of the methionine (a) and tyrosine (b) amino acids.

These systems were studied by means of scanning tunneling microscopy (STM) in ultrahigh vacuum (UHV) conditions. The Ag(111) and Cu(111) supporting substrates have been selected in order to satisfy the conditions of electric conductivity imposed by STM experiments. Their closed-packed nature implies a low atomic corrugation and an isotropic threefold symmetry. Also, their different chemical reactivities and specific electronic properties are susceptible to influence the biomolecular self-assemblies, presenting

consequently interesting control parameters. The influence of the molecular assemblies on the electronic structure of the underlying substrate were addressed. Furthermore, complementary x-ray absorption surface science techniques such as X-ray photoelectron spectroscopy (XPS) and near-edge x-ray absorption fine structure (NEXAFS) spectroscopy bring insight into the chemical state and intramolecular conformation geometry of the adsorbed species. Helium atom scattering (HAS) measurements were considered in order to corroborate, through diffraction arguments, the findings of STM in real space.

The following Chapter in this thesis describes the experimental methods used for this project and the physical principles behind them. In particular, STM, XPS and NEXAFS are addressed.

Chapter 3 deals with the self-assembly of methionine on Ag(111) under UHV conditions. The system is characterized by STM, XPS and HAS. Classical molecular mechanics calculations are discussed in order to support the model of the molecular arrangement.

In Chapter 4, the influence of the methionine self-assembly on the electronic structure of Ag(111) is approached by means of scanning tunneling spectroscopy (STS). In particular, the surface local density of states was probed by STS, and the scattering and confinement of the substrate electron surfaces states by the biomolecular arrangements are demonstrated.

The use of the methionine self-assembled structures as nanotemplates for adsorbed atomic species on Ag(111) is considered in Chapter 5. In fact, it is shown here how the biomolecular assemblage steers the self-alignment process of adsorbed Fe and Co adatoms at temperatures below 20 K.

Chapter 6 treats the self-assembly of methionine on the more reactive Cu(111) substrate, the outcome being that the increased reactivity of Cu(111) has catalytic effects on the biomolecular self-assembly. These effects were studied by means of STM, HAS and XPS, demonstrating how chemical changes of the adsorbed species can induce morphological alterations of the supramolecular arrangement.

Finally, the adsorption of the amino acid tyrosine on Ag(111) is addressed in Chapter 7 by means of STM, XPS and NEXAFS. In particular, it is shown that amino acids self-assemble following a universal non-covalent bonding scheme. This Chapter is followed by concluding remarks.

Chapter 2

Experimental methods

This Chapter will introduce the different experimental techniques used in this thesis to investigate biomolecular self-assembly on noble metal surfaces. The main tool for this study is the scanning tunneling microscope (STM). The physical concepts exploited by this technique will be presented, as well as the details of the experimental setup and procedure. All the STM measurements were performed at the Advanced Materials and Process Engineering Laboratory (AMPEL) at the University of British Columbia.

To support the STM observations, complementary surface science techniques such as helium atom scattering (HAS), X-ray photoelectron spectroscopy (XPS) and near-edge X-ray absorption fine structure spectroscopy (NEXAFS) were employed. The theoretical aspects behind these methods will be exposed briefly. These experiments were carried out at the ALOISA beamline [44] of the ELETTRA synchrotron light source in collaboration with Prof. A. Morgante's group.

2.1 Scanning Tunneling Microscopy (STM) and Spectroscopy (STS)

2.1.1 STM theory

The concept of scanning tunneling microscopy (STM) has its birth with the work of Binnig *et al.* in 1982 [36, 45]. The main advantages of this method with respect to other modern surface science techniques resides in its capacity to reach atomic level topographic resolution in real space with negligible influence on the observed system. Moreover, STM not only allows accessing real space topographic information of conducting and semiconducting samples at the atomic scale, but also to probe the physical and chemical properties related to the electronic behavior of the observed system.

STM is based on the quantum mechanical tunneling effect according to which the wavefunction of a particle with energy ϵ can penetrate through a potential barrier $\phi > \epsilon$. Within the barrier region, the electron probability density decays exponentially. Therefore, if a conducting tip is approached to a conducting sample at a small enough distance z , electrons from one electrode have a non-null probability to cross the potential barrier elastically and 'tunnel' into the facing electrode with their energy conserved. This tunneling effect between tip and sample is bidirectional, and the overall tunneling electric current is null unless a bias potential V_{bias} is applied to one of the electrodes in order to shift its Fermi level E_F and generate a measurable tunneling current I_t . In our case, V_{bias} is applied to the sample. The electron probability density decaying exponentially through the barrier, the current I_t produced by these electrons is extremely sensitive to the distance between

tip and sample, and thus, the variation of this current contains topographic information of the sample with a sub-Å vertical resolution. Only the electrons with energy ϵ between E_F and $E_F - eV_{bias}$ (e being the electron charge) contribute to I_t .

Figure 2.1(a) depicts the tunneling junction where a negative bias voltage V_{bias} is applied to the sample and therefore electrons are tunneling from the sample occupied states to the unoccupied tip states. Exploiting this physical process, a two-dimensional topographic image of the sample surface can be generated by scanning the tip at a distance between 5 and 10 Å above the sample and measuring the tunneling current. The tip is commonly positioned above the surface with pm precision by a piezoelectric actuator. The topographic STM images showed in this work were obtained by using the STM in the constant-current topographic mode. In this measuring method, the tunneling current is pre-set at a constant value and, while scanning the tip above the surface, this current is kept constant by a feedback loop which tunes the tip-sample separation. This way, the output voltage V_z of the feedback which controls the vertical position of the tip represents the two-dimensional surface topography of the observed system. This constant-current method is summarized in Fig. 2.1(b). From Fig. 2.1(a) one can intuitively notice that the tunneling current depends directly on the electronic structure of tip and sample. Therefore, it is important to point out that a STM topograph corresponds actually to a convolution of the geometrical and electronic properties of the system. This is a key factor when interpreting STM data.

Because the principle of STM is based on the measurement of electronic currents between the tip and the sample, the observed systems must be con-

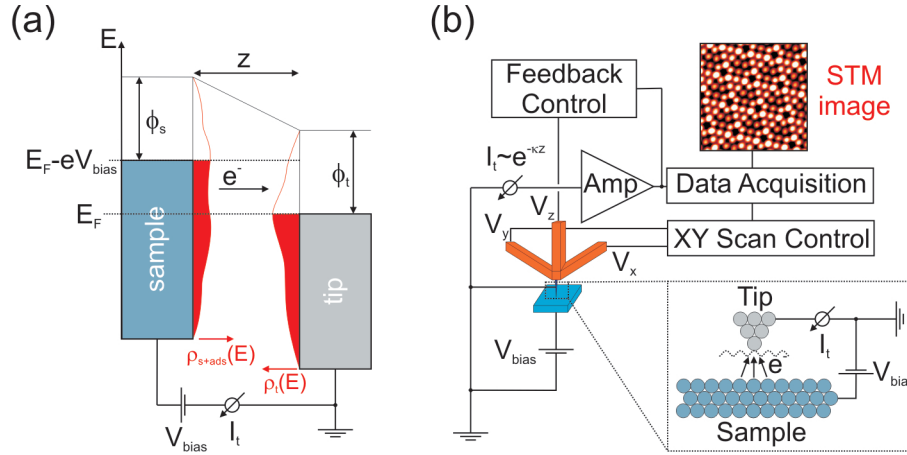


Figure 2.1: The tunneling effect and STM constant-current imaging mode. (a) The tunneling junction: the tip and sample wavefunctions can penetrate in the vacuum potential barrier, and electrons have a non-null probability to flow from the sample to the tip when a negative bias voltage V_{bias} is applied to the sample (electrons flow from the tip to the sample when the bias voltage is positive). The tunneling current I_t due to this electronic flow is a function of the local electronic density of states (LDOS) of the observed system, and decays exponentially with respect to the tip-sample distance z in the barrier. ϕ_s and ϕ_t correspond to the work functions of the sample and tip respectively. (b) Schematic diagram of a STM in constant-current topographic mode: an xyz-piezoelectric scanner positions the tip over the surface, while an electronic feedback loop keeps the tunneling current I_t constant by adapting the V_z voltage applied to the vertical z piezo. The STM image shows the atomically resolved Si(111)-(7x7) reconstruction.

ducting or semiconducting. However, STM probes the electronic structure near the Fermi level of the observed sample at small bias. This means that adsorbed atoms and molecules which alter the electronic properties of the substrate at E_F through resonant orbital coupling can be imaged. The capabilities of STM for imaging adsorbed species will be discussed in detail below.

Typically, the distance between the tip and the sample is of the order of 10 Å, and the applied bias voltage varies between ~ -2 V and $\sim +2$ V. In these conditions, the set currents are usually between the orders of ~ 1 pA and ~ 10 nA. Due to the exponential behaviour of the tunneling current with respect to the tip-sample distance, variations of this distance in the order of 1 Å correspond to tunneling current variations of one order of magnitude, and the vertical resolution reaches values below 0.1 Å. Experimentally, this high vertical sensitivity requires a perfect isolation of the system with respect to external mechanical vibrations. The lateral resolution is limited by the radius of curvature of the tip. Ideal tips with a single atom at the apex give a lateral resolution reaching the order of 1 Å. With these parameters, atomic resolution of surfaces can be achieved. The first atomically-resolved system with STM was the Si(111)-(7x7) reconstructed surface by Binnig *et al.* [38] (see Fig. 1.4(a) in the 'Introduction' Chapter).

According to Tersoff and Hamman, the tunneling current I_t can be approximated to first order by [46, 47]:

$$I_t = \frac{2\pi e}{\hbar} \sum_{\mu, \nu} [f(E_\nu) - f(E_\mu)] |M_{\mu\nu}|^2 \delta(E_\mu + eV_{bias} - E_\nu) \quad (2.1)$$

where $f(E)$ is the Fermi-Dirac distribution, e the electron charge, V_{bias} the bias voltage applied to the sample, $M_{\mu\nu}$ the tunneling matrix element between sample and tip states ψ_μ and ψ_ν having energies E_μ and E_ν respectively. The tunneling matrix element $M_{\mu\nu}$ can be written in terms of the expression used by Bardeen in 1961 to describe the tunneling current between two metallic electrodes separated by an insulating oxide layer [48]:

$$M_{\mu\nu} = \frac{\hbar^2}{2m} \int_S (\psi_\mu^* \nabla \psi_\nu - \psi_\nu^* \nabla \psi_\mu) d\vec{\sigma} \quad (2.2)$$

where S is any surface lying within the barrier region and m the electron mass. Here, the expression in between parenthesis is the probability current density operator. Although equation (2.1) might recall first-order perturbation theory and Fermi's 'Golden Rule', a fundamental difference resides in the fact that, in this approach, ψ_μ and ψ_ν are non-orthogonal independent states of the separated sample and tip systems respectively. Therefore, they do not correspond to a complete orthogonal basis set of the total tunneling junction system. The hypothesis of independent ψ_μ and ψ_ν states is only valid for large tip-sample distances. The transmission matrix $M_{\mu\nu}$ depends explicitly on ψ_μ and ψ_ν , and some assumptions have to be made in order to obtain a useful expression for I_t . In particular, it is very difficult to determine the geometry and hence the state of the tip. In this same formalism, the substrate states are approximated by two-dimensional Bloch states decaying exponentially in the direction perpendicular to the surface, whereas the tip states were assumed to have only an s -wave character. This hypothesis is justified by the fact that s -type wavefunctions having a further spatial extent than p and d waves, states with zero angular momentum contribute therefore more significantly than states with non-zero angular momentum to the tunneling current in the considered range of tip-sample distances. Furthermore, it was assumed that the temperatures were low enough in order to approximate the Fermi-Dirac distributions by step-functions, and that the applied bias voltages were also small. By implementing these assumptions in equation 2.1, the expression for I_t becomes:

$$I_t \propto \sum |\psi_\mu(\vec{r}_t)|^2 \delta(E_\mu - E_F) \equiv \rho_s(\vec{r}_t, E_F) \quad (2.3)$$

$\rho_s(\vec{r}_t, E_F)$ being the local density of states (LDOS) of the sample at E_F and at the tip position \vec{r}_t . These hypothesis might seem unrealistic to obtain a quantitative picture for the tunneling process, but this approach explains how the tunneling current is a direct measurement of the electronic structure of the sample. The exponential dependence of I_t with respect to the tip-sample distance z is included in the expression of $M_{\mu\nu}$ when the assumption of Bloch states and s -wave is made for the sample and tip states respectively. In particular, many discussions have concerned the s -wave character of the tip state, as atomic resolution and other low-scale features resolved for metal and semiconductor surfaces can only be explained by considering p and d orbitals for the tip and sample states [49].

The expression in equation (2.3) is valid for small bias voltages (i.e. in the order of 10 mV). For larger values of V_{bias} , Selloni *et al.* expressed I_t more generally in the Wentzel-Kramers-Brillouin (WKB) formalism as follows [50]:

$$I_t(V_{bias}) \propto \int_0^{eV_{bias}} \rho_s(\vec{r}_t, E) T(E, V_{bias}, z) dE \quad (2.4)$$

where the energy E is considered with respect to the Fermi level, the tip density of states ρ_t is assumed constant in the energy window $[E_F; E_F + eV_{bias}]$ and $T(E, V_{bias}, z)$ is the tunneling transmission probability. $T(E, V_{bias}, z)$ is derived from Bardeen's tunneling matrix $M_{\mu\nu}$ by assuming that the sample states are two-dimensional Bloch functions and that tip and sample states decay exponentially in the barrier:

$$T(E, V_{bias}, z) = \exp\left(-2z\sqrt{\frac{m}{\hbar^2}\sqrt{\phi_s + \phi_t + eV_{bias} - 2E}}\right) \quad (2.5)$$

Here, ϕ_s and ϕ_t are the sample and tip work functions respectively. The work functions of metals are typically around ~ 5 eV (e.g. $\phi_W = 4.55\text{eV}$; $\phi_{Ag(111)} = 4.74\text{eV}$, $\phi_{Cu(111)} = 4.98\text{eV}$ [51]). Therefore, we can assume that $\phi_s = \phi_t$. It is important to notice that, when $V_{bias} < 0$ (i.e. electrons are tunneling from sample to tip), $T(E, V_{bias}, z)$ is largest when $E = eV_{bias}$, meaning that the sample electrons at the highest occupied level contribute the most to I_t . On the other hand, when $V_{bias} > 0$ (i.e. electrons are tunneling from tip to sample), electrons at the tip Fermi level have the most consequent contribution on I_t . Therefore, one can say in general that the tunneling probability is always the largest for electrons at the Fermi level of the negatively biased electrode.

The Tersoff-Hamann formalism, introduced in equation (2.1) and generalized in equation (2.4) which link I_t to the topographic and electronic properties of the sample, implied drastic assumptions, such as the s -wave nature of the tip state and the independence of tip and sample states. In particular, this perturbative method does not explain the atomic resolution on metals which is experimentally obtained with STM. An alternative approach resides in scattering theory, where the single-electron Hamiltonian is defined by the scattering potentials of the tunneling barrier and the electrodes. The tip is modeled by a single atom on one of the electrodes and introduces a perturbing scattering potential. The tunneling current is then calculated by applying a Green's function technique and Ehrenfest's theorem [52]. This method does not require any assumptions on the nature of the tip states. Also, the in-

fluence of the applied bias potential V_{bias} is implemented. Furthermore, tip and sample states are not assumed here to be independent. This formalism successfully explains the low-scale topographic resolution such as the atomic corrugation which can be measured with STM and whose demonstration is not enabled by the simpler Tersoff-Hamann approach.

2.1.2 Scanning tunneling spectroscopy (STS)

Equation (2.4) demonstrates how I_t yields information of the sample electronic density of states $\rho_s(\vec{r}_t, E)$. For instance, the derivative of I_t with respect to V_{bias} gives:

$$\begin{aligned} \frac{dI(V_{bias})}{dV_{bias}} &\propto \rho_s(\vec{r}_t, eV_{bias})T(eV_{bias}, V_{bias}, z) \\ &\times \int_{E_F}^{E_F+eV_{bias}} \rho_s(\vec{r}_t, E) \frac{dT(E, eV_{bias}, z)}{dV} dE \end{aligned} \quad (2.6)$$

In this expression, $\rho_s(\vec{r}_t, E)$ is convoluted by an exponential term with respect to V_{bias} introduced by the transmission factor $T(E, V_{bias}, z)$. However, dividing dI_t/dV_{bias} by I_t/V_{bias} yields $d(\ln I_t)/d(\ln V_{bias})$, which eliminates the exponential term [53–55]:

$$\begin{aligned} \frac{dI_t(V_{bias})/dV_{bias}}{I_t(V_{bias})/V_{bias}} &= \frac{dI_t/dV_{bias}}{\frac{d(\ln V_{bias})}{dV_{bias}} / \frac{d(\ln I_t)}{dI_t}} = \frac{d(\ln I_t)}{d(\ln V_{bias})} \\ &\propto \rho_s(\vec{r}_t, eV_{bias}) \end{aligned} \quad (2.7)$$

The division of the first derivative of I_t by I_t/V_{bias} is necessary when large bias voltages are applied in order to suppress the exponential behavior

due to the transmission term. When smaller voltages are considered (i.e. $eV_{bias} \ll \phi_s$), one can directly approach $\rho_s(\vec{r}_t, eV_{bias})$ with dI_t/dV_{bias} :

$$\frac{dI(V_{bias})}{dV_{bias}} \propto \rho_s(\vec{r}_t, eV_{bias}) \quad (2.8)$$

In the framework of this thesis, we apply first-derivative STS to probe the electronic Shockley surface states of the Ag(111) substrate. Therefore, the surface state band onset being located 67 meV below the Fermi level [56], only low voltages are applied when evaluating local electronic density of states with STM, and thus equation (2.8) without the I_t/V_{bias} normalization is used.

This approach in which the tunneling current is treated to extract spectroscopic information from the sample electronic configuration is called scanning tunneling spectroscopy (STS). Concretely, the experimental procedure usually consists in placing the tip at a given position \vec{r}_t and tip-sample separation z , and varying V_{bias} with the constant-current feedback loop 'open' (i.e. the tip height over the sample remains constant during the measurement, assuming that there is no drift). Therefore, evaluating the first derivative of I_t with respect to V_{bias} gives access to features in $\rho_s(\vec{r}_t, eV_{bias})$. Now, by scanning the tip over the sample in the constant-current mode (i.e. with the feedback loop closed) at a given V_{bias} and considering the dI_t/dV_{bias} signal at each location allows to resolve spatially some electronic features. These two-dimensional distribution matrices of the I_t first derivative are called dI/dV maps. Regarding these dI/dV maps however, it is crucial to point out that, due to the constant-current scanning, the spatial dI/dV signal represents a convolution between the sample LDOS (in a first-order approximation) and

its topography. An alternative spectroscopic method consists in varying z while leaving V_{bias} constant, but this approach will not be used in the context of this work.

Measuring the first derivative signal of I_t is not trivial. The direct way would consist in simply differentiating the I_t/V_{bias} curves obtained with the feedback loop open. However, this method implies a poor signal-to-noise ratio. Here, dI_t/dV_{bias} is directly measured with a lock-in technique, consisting in adding to V_{bias} a harmonic modulation signal $V_{osc}(t)$ of amplitude V_{mod} and frequency $\nu = \omega/2\pi$: $V_{bias}(t) = V_0 + V_{osc}(t) = V_0 + V_{mod} \sin(\omega t)$ where V_0 is the constant component of V_{bias} . Consequently, the tunneling current I_t is also modulated with a frequency ν and a phase difference ϕ with respect to the modulation signal. The correlation ($I_t(t) \star V_{osc}(t)$) between $I_t(V_0 + V_{mod} \sin(\omega t + \phi))$ and the modulation signal $V_{osc}(t)$ is given by:

$$I_t(t) \star V_{osc}(t) = \int_0^T I_t(s) V_{osc}(t+s) ds \quad (2.9)$$

where T is an integration time constant.

Now, usually $V_{mod} \ll V_0$ (i.e. V_{mod} is in the order of 1 to 5 mV), what allows us to consider the Taylor expansion of I_t around V_0 to the first-order:

$$I_t(V_0 + V_{mod} \sin(\omega t + \phi)) = I_t(V_0) + \frac{dI_t(V_0)}{dV_{bias}} V_{mod} \sin(\omega t + \phi) + \dots \quad (2.10)$$

The correlation between $I_t(V_0)$ and $V_{osc}(t)$ being null, one gets for ($I_t(t) \star V_{osc}(t)$):

$$\begin{aligned}
(I_t(t) \star V_{osc}(t)) &\simeq \int_0^T \frac{dI_t(V_0)}{dV_{bias}} V_{mod}^2 \sin(\omega s + \phi) \sin(\omega(t + s)) ds \\
&\simeq \frac{TV_{mod}^2 \cos(\phi - \omega t)}{2} \frac{dI_t(V_0)}{dV_{bias}}
\end{aligned} \tag{2.11}$$

At $t = 0$, the correlation gives:

$$(I_t(t = 0) \star V_{osc}(t = 0)) \simeq \frac{TV_{mod}^2 \cos(\phi)}{2} \frac{dI_t(V_0)}{dV_{bias}} \tag{2.12}$$

Therefore, by evaluating the correlation at $t = 0$ between the tunneling current and a sinusoidal modulation signal on the bias voltage, one obtains a quantity proportional to the value of dI_t/V_{bias} at the constant component V_0 of the bias. Experimentally, this correlation at $t = 0$ is measured by a lock-in amplifier, with ν , T , V_{mod} and ϕ being parameters which will determine the quality of the signal. For example, if increasing T and V_{mod} improves the signal-to-noise ratio, a large measurement duration will however amplify any possible drift effect and the energy resolution will be diminished by the significant modulation amplitude V_{mod} . The values commonly used for ν are in the 1-8 kHz range, requirements being that ν is above the bandwidth of the feedback loop in order to maintain the feedback unaffected during dI_t/dV_{bias} mapping, and that ν does not match any frequency component of I_t . The optimization of these parameters is accomplished empirically, and the values used in this work are 3 kHz, 20 ms and ~ 4 mV for ν , T and V_{mod} respectively in the case of dI_t/dV_{bias} spectra at a given tip location with the feedback loop open, and 3 kHz, 5 ms and ~ 7 mV for ν , T and V_{mod} respectively in the case of 2D dI_t/dV_{bias} maps with the feedback loop closed. Also, it is important to

set the phase difference ϕ between I_t and V_{osc} to zero in order to maximize the signal amplitude.

In the past, STS measurements successfully obtained local electronic information of semiconducting surfaces [54, 55], of electronic surface states of closed-packed metal surfaces [57] as well as their confinement by topographic features on the surface [58], and even resolving local magnetic features on a surface with a magnetic tip [59, 60]. Moreover, the analysis of the second derivative of I_t permits to detect the excitation of vibrational modes on the surface by inelastic electron scattering, and thus to obtain local chemical information of the system [61].

One of the main assets of this spectroscopic method is that it gives access to the spatial dependency of the sample electronic features, whereas standard spectroscopic methods (e.g. optical spectroscopy) can only provide a spatial average. For example, results given by STS agree with ultraviolet photoelectron spectroscopy (UPS) results, with the supplementary advantage that the same method yields access to both occupied and unoccupied states [62]. Moreover, its energy resolution can reach the order of 5 meV. Nevertheless, STS is an efficient tool only in some specific experimental conditions, and it cannot replace completely other spectroscopic methods. For instance, the energy window which is accessible with STS is, at best, only in the order of $\pm \sim 4$ eV, this due to structural instabilities of the junction for higher bias voltages. Furthermore, the need to apply a bias voltage to the sample introduces a perturbation in the system: the electric field which ensues can give rise to a Stark effect and influence the sample electronic levels. However, it has been shown that for a tunneling current range of 50pA to $1\mu\text{A}$, the

Stark shift for the Ag(111) surface state electrons is in the order of 4 meV, which can be neglected with respect to the method resolution [63].

2.1.3 Investigating adsorbates on metal surfaces with STM

Due to their relevance for the design of novel technological devices, the study of adsorbed species and of the physical and chemical processes that they undergo on atomistically clean substrates is a main topic in modern surface science. STM, with its real-space atomic level resolution, represents an unmatched tool for this purpose. The real-space visualization of atomic and molecular adsorption enables monitoring of such fundamental processes as epitaxial growth, heterogeneous catalysis, surface reconstruction, friction and corrosion among others, whose understanding is crucial for future technological developments. In the framework of this thesis, the studied biomolecular species are vapor deposited onto the metal surfaces in ultrahigh vacuum (UHV) conditions by organic molecular beam epitaxy (OMBE). Once adsorbed, the behaviour of the molecules is determined by the interplay between adsorbate-adsorbate and adsorbate-substrate interactions within a set of given macroscopic parameters such as deposition rate Γ and temperature T . This behaviour is dictated by such phenomena as surface diffusion, possible desorption, non-covalent synthesis or self-assembly, chemical reactions driven by reactive substrates and binding to specific low-coordinated sites (e.g. substrate step-edges) [64]. The interplay between dynamics and kinetics of the adsorbate-substrate system defines the balance between these processes [15, 37]. In fact, let's define the diffusivity D of the molecular

species as $D \propto \langle \lambda \rangle^2 \nu_0 \exp(-E_m/k_B T)$, where $\langle \lambda \rangle$ is the adsorbate average hopping length during a diffusion event, ν_0 the corresponding prefactor and E_m the migration barrier [65]. The attempt frequency ν_0 is related to the adsorbate vibrational frequency at the bottom of the adsorption potential and is in general of the order of $\nu_0 \simeq 10^{13}$ [37]. The migration barrier E_m is due to the adsorption potential imposed by the substrate and corresponds usually to $\sim 5\text{-}20\%$ of the adsorbate adsorption energy [37, 65]. Now, if D is large with respect to the adsorption rate Γ , where $\Gamma = p/\sqrt{2m\pi k_B T}$ (m being the adsorbate mass and p the adsorbate gas pressure [64]), the system has access to the totality of its phase space and can relax into a thermodynamic equilibrium state at each step of the deposition. On the other hand, if Γ dominates D , the system cannot relax into a thermodynamic equilibrium and it can, depending on the balance between adsorbate-substrate and lateral adsorbate-adsorbate interactions, reach a metastable non-equilibrium configuration governed by kinetics. The balance between Γ and D which defines the limit between thermodynamics and kinetics depends on the strength of the lateral inter-adsorbate interactions, and systems involving weak and directional non-covalent intermolecular bonds yield thermodynamically equilibrated configurations [15]. For these weakly interacting systems evolving in near equilibrium conditions, self-correction upon deposition into a thermodynamically stable is possible.

The nature of the substrate-adsorbate interactions is critical for the supramolecular adsorbed configuration. On the other hand, the substrate can also undergo dramatic changes due to the presence of the adsorbed species. For example, adsorbate-induced surface reconstructions are often observed. Also,

the polarization of the substrate electronic distribution mediated by polar groups and the hybridization with the adsorbate electronic orbitals can perturb the substrate electronic properties by altering the work function and/or LDOS at E_F .

The possibility of imaging adsorbed species with STM allows tracking of these fundamental processes taking place at the substrate interface. The observation with STM of atoms or small molecules on metal surfaces implies immobilization of the species on the surface, or at least minimized diffusion with respect to the scanning speed. For these reasons, performing STM measurements at low temperature is appropriate to control the adsorbate mobility and permit their imaging. Moreover, low temperature improves the mechanical stability of the tunneling junction and is necessary in STS measurements in order to limit the thermal drift of the piezoelectric scanner and the thermal broadening of the observed electronic features. For instance, the STM data exhibited in this work were all obtained in a temperature range between ~ 4 and 20 K.

The correlation between STM constant-current data and actual sample topography is not straightforward when it comes to visualizing adsorbed atoms or molecules. For instance, early STM imaging of Xe atoms on Ni(110) at 4 K shows the atomic adsorbates as 1.6 Å-high protrusions [66], whereas oxygen atoms on Al(111) [67] and Ni(100) [68] are seen as 0.7 and 0.3 Å-deep holes respectively, even though O is known to adsorb on Ni(100) hollow sites 0.8 Å above the topmost Ni layer [69]. Concerning the imaging of organic molecules, early experiments achieved the real-space observation of benzene and CO molecules coadsorbed on Rh(111), showing an ordered saturated

monolayer with the benzene molecules appearing as ring-like protrusions [39] (see 'Introduction' chapter for a STM topograph). Furthermore, intramolecular topographic details in real-space could be obtained for the first time for isolated Cu-phthalocyanine molecules on Cu(100) [70]. Another interesting case of organic molecular adsorption is the system composed of CO adsorbed on Pt(111), where the CO molecules are visualized differently depending on their adsorption site [71]. With respect to molecules which have key functions in biological systems, some work exists where the adsorption of amino acids [72, 73] and nucleic acids [73, 74] on metal surfaces have been studied with STM.

The examples of oxygen atoms on Ni(100) and Al(111) and of carbon monoxide on Pt(111) mentioned above illustrate the difficulty of translating the STM data into real physical properties. A theoretical interpretation for these cases is still an open challenge. However, some formalisms have succeeded in providing insight in this matter. Basically, a complete theoretical picture of adsorbate STM imaging has to include the influence of the adsorption process on the electronic properties of the system, and a general form for the electronic tunneling in between the two electrodes itself. The chemisorption of species on a substrate broadens the initially unperturbed and sharp δ -function electronic energy levels of the adsorbed entities, this due to resonant coupling and partial hybridization with the substrate continuum states [37]. Although the electronic features of the adsorbed system are distant in energy with respect to E_F , the broadening can cause that a tail of an orbital contributes to the LDOS near E_F . In consequence, the imaging of the adsorbate is enabled. Chemisorption not only disturbs the surface

through an electronic contribution near E_F , but it usually alters its work function and induces a charge transfer between the bonded species and the substrate depending on the relative energy position of the electron affinity and the ionization potential with respect to E_F . On the other hand, if the species are physisorbed, the binding with the substrate has a van der Waals character and the substrate electronic configuration is affected through polarization. Lang was the first to propose a theoretical approach to adsorbate imaging with STM [75, 76]. His Bardeen-like first-order perturbative picture where the substrate was modeled as a jellium surface was able to explain how a sodium atom could contribute to the LDOS near E_F and thus appear as a protusion, although its electronic levels were positioned in energy far from E_F . Also, it showed how an He atom, which adsorbs far above the surface, does not contribute to the LDOS due to its filled valence shell, but polarizes the substrate electronic distribution at E_F and therefore is imaged as a hole. More recent and developed theoretical explanations are based on scattering theory and Green-function techniques [77]. Here, different tunneling current channels contribute to I_t and systems where the adsorbed species appear differently depending on their adsorption sites (such as CO on Pt(111)) could be resolved.

Visualizing and correctly interpreting the STM data of atomic and molecular adsorbates allowed investigating in real-space and real-time some fundamental physical processes taking place on metal interfaces. For example, the surface reconstruction of Rh(100) induced by the adsorption of oxygen was resolved [78]. Moreover, recent designs of fast scanning STMs allowed tracking the diffusion events of atoms [79, 80] and molecules [81] on sur-

faces. Also, catalytically induced molecular dissociation could be observed with STM [82], and even intramolecular conformational alterations could be described [14].

2.1.4 The STM experimental setup

This section will describe the low-temperature scanning tunneling microscopy (LT-STM) setup with which all the presented STM and STS data were acquired at the Advanced Materials and Process Engineering Laboratory (AMPEL), University of British Columbia. The STM experiments in this work were performed in a ultrahigh vacuum (UHV) chamber equipped with a commercial low-temperature Besocke-type [83] scanning tunneling microscope (LT-STM) [84] and various other tools which allow *in situ* sample preparation and characterization. The STM, designed at the Freie Universität of Berlin by G. Meyer [84, 85] and now commercialized by CreaTec, consists in three piezoelectric ceramic cylinders (which we will call the outer piezos) which support a copper ramp. Sapphire half-spheres make the contact between these piezo actuators and the ramp, which is free in the lateral directions. The bottom of the ramp is not flat, but each outer piezo is placed beneath a different oblique plane. This geometry, characteristic of a Besocke-type STM, allows to perform coarse displacements of the tip with respect to the sample in the vertical and lateral orientations. The tip is placed on a central piezoelectric cylinder pointing downwards to the sample. In the framework of this thesis, the STM data were acquired by scanning in the lateral x - y plane defined by the substrate with the outer piezos, with the tip-sample distance regulated by the central piezo. At the temperatures where the experiments

are performed, these actuators have a voltage-to-displacement ratio of the order of 10 Å per V, which allows a pm precision for the tip positioning. While the tip is scanned laterally, the tip-sample distance is tuned in the z direction by the central piezo, and topographic information of a sample is obtained in the constant-current mode. A digital feedback loop having I_t as an input controls the signal V_z of the z-piezoelectric during the scan in order to maintain I_t constant. The signal $V_z(x, y)$ represents therefore a 2D matrix and the sample topography. The tunneling current I_t is converted into a voltage signal by an I/V current amplifier. This device is placed as close as possible to the measuring point in order to avoid coupling electronic noise to the tunneling current. The results presented here were obtained with a 10^9 I/V conversion gain.

A detail of the STM head can be viewed in Fig. 2.2(a). In the measuring position, the piezoelectric scanner and the sample holder hangs from Inconel springs that, along with the Eddy current magnets, damp the outer high frequency vibrations ($> \sim 50$ Hz). The tunneling junction being exponentially sensitive to tip-sample distance variations, it is crucial to effectively isolate the system from mechanical vibrations. The STM head is surrounded by a nickel-coated aluminum shield which protects the system from outer thermal radiation (necessary to maintain the temperature low) and also acts as a Faraday cage preventing to couple any electromagnetic noise from the outside. The sample is located on a copper sample holder (see Fig. 2.2(b)) to which the bias voltage is applied through electrical contacts.

The STM head is coupled to a liquid N₂ shielded ⁴He bath cryostat which allows cooling the sample down to 4 K in the cooling position (see Fig. 2.3(a)).

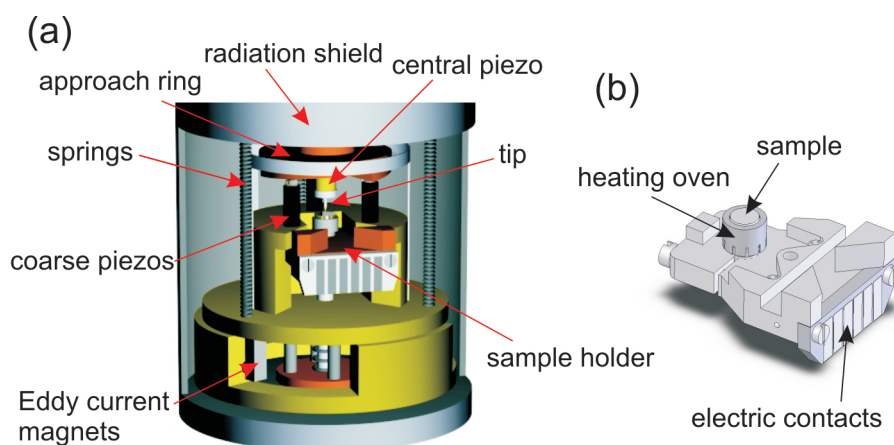


Figure 2.2: STM head and sample holder. (a) 3D drawing of the Besocke-type STM head. Reproduced from [85]. (b) Detail of the sample holder. Metal sample can be baked to 800 K by resistive heating. Temperature of the sample is measured with a chromel-alumel thermocouple.

However, in the measurement position, the sample temperature drifts up to 9 K, where it remains stable almost permanently with respect to the time-scale of our experiments. The temperature of the sample during the STM measurements can be tuned with a Zener diode within a temperature range of 9 K to room temperature. The temperature on the STM head is measured with a Si diode. All the STM results presented here were obtained by measuring in constant-current mode with the sample held at temperatures between 6 and 19 K. The motivations of working at a low temperature are multiple. First, the diffusion of the studied adsorbates is controlled. Also, the tip structural configuration is extremely stable. Moreover, the drift due to the thermal relaxation of the piezoelectric ceramics is minimized. Finally, in the case of STS measurements, the electronic features observed in the spectra present a negligible thermal broadening.

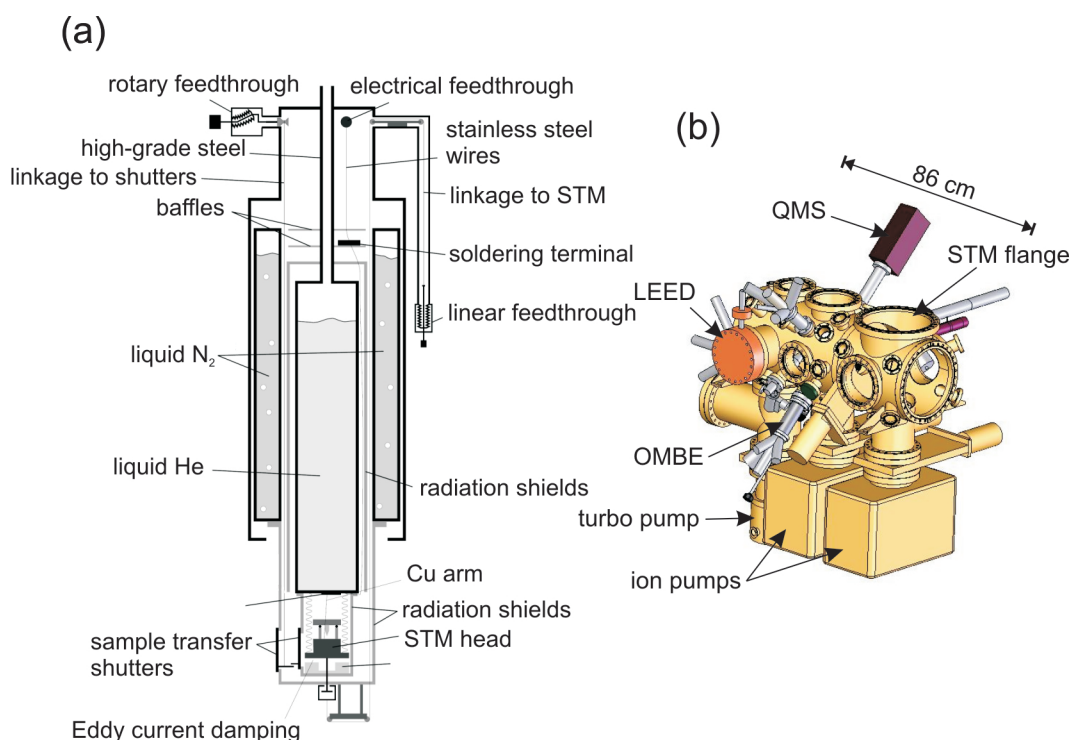


Figure 2.3: The liquid He refrigerated STM and the custom-designed UHV chamber. (a) Drawing of the low-temperature STM with the liquid He bath cryostat. Image reproduced from [85]. (b) 3D drawing of the custom-designed UHV chamber with instruments for *in situ* sample preparation and characterization.

All experiments were carried out in ultrahigh vacuum (UHV) conditions at a base pressure lower than 5×10^{-10} mbar. The UHV setup was custom-designed as part of this thesis project in collaboration with the company VAB. The vacuum system is composed of three turbomolecular pumps connected in series, two ion pumps and a titanium sublimation pump (TSP). The UHV chamber is divided in two sub-chambers separated by a gate valve: the preparation chamber, where the sample is prepared and characterized, and

the STM chamber, where the STM and STS measurements are performed (see Fig. 2.3(b)). The preparation chamber is equipped with different state-of-the-art surface science technique tools for *in situ* sample preparation and characterization, such as a low-energy electron diffraction (LEED) setup, a quadrupole mass spectrometer (QMS), an ion gun for Ar⁺ sputtering, an organic molecular beam epitaxy (OMBE) cell for molecular deposition, several leak valves for controlled gas introduction and several cold cathode gauges for pressure measurements. The sample holder presented in Fig. 2.2(b) can be easily transferred from the preparation to the STM chamber with a translational manipulator. In the preparation chamber, the sample temperature can be tuned from ~ 77 K (by flux cooling tubes thermally coupled with the sample) to more than 800 K (by resistive heating). The entire UHV setup seen in Fig. 2.3(b) is fixed on an aluminium frame which is positioned on passive compressed air pneumatic isolators which, along with the Inconel springs and Eddy current damping magnets, decouple the entire setup from external vibrations. A photograph of the STM setup at AMPEL is depicted in Fig. 2.4.

2.1.5 Preparation procedures

The chosen substrates on which the biomolecular self-assemblies are studied are monocrystalline Ag(111) and Cu(111) ($a_{Ag(111)}=4.09$ Å, $a_{Cu(111)}=3.61$ Å at 300 K). The selection of these surfaces is motivated by their low chemical reactivity and their low-corrugated closed-packed threefold symmetry. Different effects on the molecular arrangements on both surfaces are expected due to their different chemical properties. These samples are chemome-

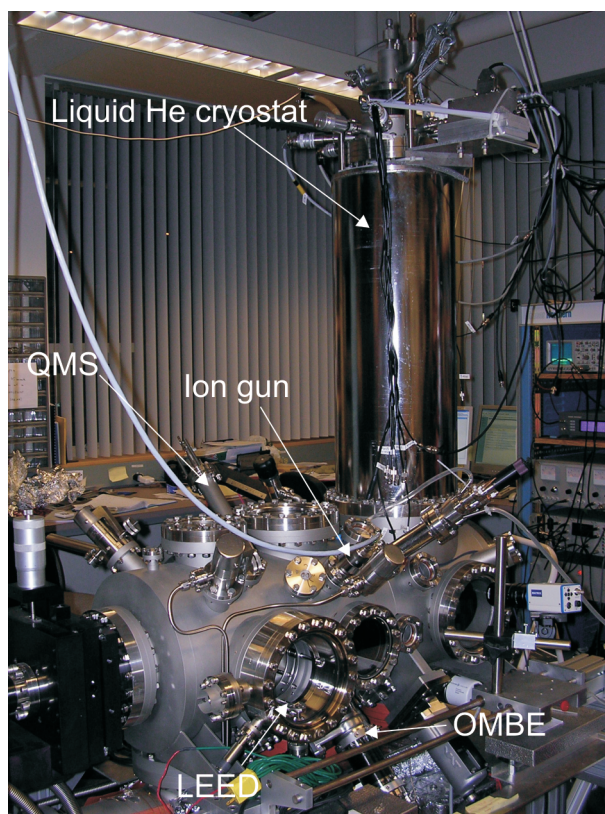


Figure 2.4: Photography of the STM setup at AMPEL.

chanically polished. This cleaning procedure in the UHV chamber before molecular deposition consists in repeated Ar^+ sputtering cycles at an energy of 0.8keV and currents of typically $4 \mu\text{A}$, followed by sample annealing at a temperature of 770 K for about 10 min.

All the presented STM data were obtained with a tungsten (W) tip of diameter 0.25 mm. Before introducing in the UHV chamber, the tip was electrochemically etched following the procedure depicted in Fig. 2.5. By applying a DC voltage of ~ 10 V in between a stainless-steel cathode and the

W tip acting as an anode in a 2M NaOH solution, W is oxidized into soluble WO_4^{2-} , creating a sharp apex at the end.

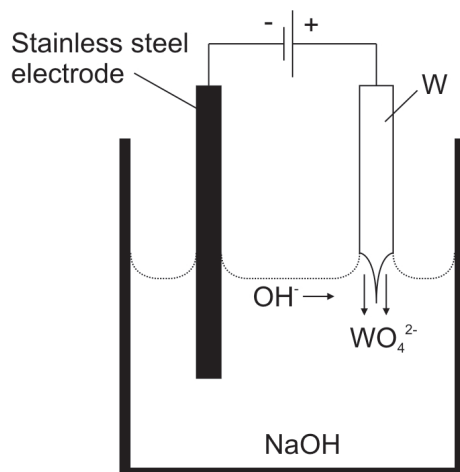
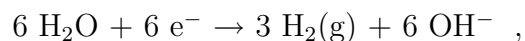


Figure 2.5: Schematic of the W tip electro-etching. W tip is etched in a 2 M solution of NaOH. Water is reduced at the cathode, while W is oxidized into soluble WO_4^{2-} at the anode.

The chemical reaction taking place at the cathode is:



while at the anode:



This yields the overall reaction:



Once the tip is in the UHV chamber, the oxide layer can be removed by Ar^+ sputtering. Also, a technique to sharpen and stabilize the tip consists in

dipping it in a *controlled* fashion onto the clean metal substrate. In the latter procedure, one must note that the atoms at the apex of the tip would not correspond to W atoms anymore, but to atoms of the nature of the substrate. The parameters for this procedure are optimized empirically.

The enantiopure methionine and tyrosine amino acid molecules ($\geq 99.5\%$, Sigma-Aldrich) were deposited onto the Ag(111) and Cu(111) substrates by organic molecular beam epitaxy (OMBE) by evaporating from a glass crucible heated to a temperature of 370 K. The substrate temperatures during molecular deposition will be specified for each experiment. The molecular coverages θ on the silver and copper samples were derived from STM data and are given in terms of monolayers (ML), where 1 ML corresponds to a saturated molecular layer completely covering the surface. All the molecular depositions are enantiopure, meaning that only preparations with enantiomers of the same chirality will be considered. Upon biomolecular deposition, the sample is cooled down and introduced into the STM chamber for *in situ* transition metal adatom deposition and/or STM observation.

In the case of the methionine self-assembly on Ag(111), the biomolecular nanostructures are used as templates for the self-organization of transition metal atomic species. For this purpose, iron (Fe) and cobalt (Co) adatoms are deposited onto the noble metal substrate by evaporating from a properly degassed pure filament of respectively Fe and Co wound around a W wire. This adatom deposition procedure is performed *in situ* in the STM chamber with the Ag(111) substrate held at 8 K.

The presented conductance STS data are obtained using a lock-in technique with a bias voltage modulation of ~ 4 mV amplitude, 3 kHz frequency

and 20 ms time-constant in the case of dI_t/dV_{bias} spectra, whereas in the case of dI_t/dV_{bias} maps these parameters are ~ 7 mV, 3 kHz and 5 ms for the modulation amplitude, frequency and time-constant respectively.

The exhibited STM topographs and dI_t/dV_{bias} maps are treated using FFT filtering and Gaussian smoothing with the WSxM SPM program [86].

2.2 Complementary surface science techniques

In this following section we will describe briefly the theoretical principles behind helium atom scattering (HAS), X-ray photoelectron spectroscopy (XPS) and near-edge x-ray absorption fine structure (NEXAFS) spectroscopy. These experiments were performed at the ALOISA beamline of the ELETTRA synchrotron light source (Trieste, Italy) [44] in collaboration with Prof. A. Morgante's group. The samples were prepared and measured in the same *in situ* UHV conditions as for the STM experiments.

2.2.1 Helium Atom Scattering (HAS)

When it comes to observing adsorbates on metal surfaces, the difficulty in interpreting topographic STM images requires support of real-space data with diffraction information of the same system. For this purpose, helium atom scattering (HAS) was performed on some of the studied systems. The experimental setup at the ALOISA beamline allows performing HAS and XPS measurements simultaneously. The HAS method consists in measuring the diffraction pattern of a monochromatic He beam elastically scattered from the observed surface. The fact that the He atoms are sensitive to

the charge density of the sample's topmost layer implies that the beam is exclusively scattered at the surface and that only periodic features at the surface are detected. Moreover, the use of a low-energy beam renders this technique perfectly non-destructive. The nature of the interaction between the He atoms and the metal surface is of the van der Waals type. More specifically, the interaction arises from the polarization induced by the He atoms on the metal substrate.

The monochromatic beam is produced by an adiabatic expansion from a stagnation chamber at He pressure p_0 and temperature T_0 into the main UHV experiment chamber at pressure p_1 and temperature T_1 [87]. During the HAS procedure, p_1 remains always below 1×10^{-9} mbar, and the ratio between p_1 and p_0 is of the order of 10^7 . The connection between the stagnation chamber and the UHV chamber is achieved through a $10 \mu\text{m}$ diameter nozzle through which the continuum flow in the stagnation chamber is transformed into a free-molecular flow. A collimator renders the random He trajectories into a directional beam with a diameter of 0.7 mm at the scattering sample. Following the collimator, a chopper gives beam pulses of 4×10^8 atoms with a frequency of 960 Hz . Because the flux is fast with respect to diffusion processes, the expansion is considered adiabatic, and therefore the work performed on the gaseous system is exclusively transferred into the beam translational energy. Within the perfect gas hypothesis and assuming that the heat capacity at constant volume C_V is constant, we can write that $T_1 = T_0(p_1/p_0)^{\frac{\eta-1}{\eta}}$ where $\eta = C_p/C_V$. Hence, p_1/p_0 being of the order of 10^{-7} , $T_1 \ll T_0$ and the velocity distribution within the expanded beam is very sharp. By controlling the temperature T_0 in the nozzle chamber, the

energy of the beam can be tuned between 18.6 and 100 meV. In our case, we will use a He beam of energy 19 meV in order to minimize the possible damage on the molecular arrangements. The sample temperature can be controlled in between 100 and 1000 K during the measurement. Detection of the He beam is made by ionizing the He atoms in a quadrupole mass filter.

Let's assume that the observed molecular self-assemblies on the substrate present periodic features with can be characterized by a two dimensional super-lattice with vectors \vec{a}' and \vec{b}' in the substrate plane. Given a He beam with initial momentum \vec{k}_i and assuming elastic scattering on the observed sample, the beam is scattered with a momentum \vec{k}_f satisfying the Laue conditions in two dimensions:

$$\Delta\vec{k} \doteq (\vec{k}_f - \vec{k}_i) \cdot \vec{a}' = 2\pi m \quad \text{and} \quad \Delta\vec{k} \cdot \vec{b}' = 2\pi n \quad (2.13)$$

where m, n are integers. These conditions are imposed by the periodicities within the substrate plane. In the direction normal to this plane, we can consider that the structures present a periodicity with a wavelength of infinite magnitude (i.e. the normal component of the reciprocal space vectors \vec{G} can take continuous values from zero to infinity) and there is no condition to satisfy for the normal component of $\Delta\vec{k}$: we talk therefore about diffraction rods and not diffraction points [37]. The specular scattered beam with momentum \vec{k}_f^{spec} corresponds to the scattering process satisfying equations (2.13) with $n, m = 0$, whereas \vec{k}_f^{sat} correspond to the wave vectors of the satellite diffraction features. The setup allows to perform the HAS measurements simultaneously with the molecular deposition, the estimation of the molecular coverage being enabled by the consequent decrease in the specular

beam intensity.

The geometry of the setup is detailed in Fig. 2.6. The He beam source and the He detector are separated with an angle $\theta_{tot} = 110^\circ$. Considering the coordinate system $Ox'y'z'$ attached to the sample (axis x' and y' define the sample plane), the sample can undergo a rotation $\mathcal{R}(\theta, \varphi) = \mathcal{R}_{x'}(\theta) \circ \mathcal{R}_{y'}(\varphi)$ where $\mathcal{R}_{x'}(\theta)$ ($\mathcal{R}_{y'}(\varphi)$, respectively) is a rotation of angle θ (φ , respectively) around y' (x' , respectively). By varying the angles θ and φ , the two-dimensional diffraction pattern $(\Delta k_x, \Delta k_y)$ can be mapped, where $\Delta \vec{k}_x$ and $\Delta \vec{k}_y$ are the components of $\Delta \vec{k}_\parallel$ in the sample coordinate system, $\Delta \vec{k}_\parallel$ being the orthogonal projection of $\Delta \vec{k}$ on the substrate plane: $\Delta \vec{k} = \Delta \vec{k}_\perp + \Delta \vec{k}_\parallel$ and $\Delta \vec{k}_\parallel = \Delta k_x \cdot \vec{e}_{x'} + \Delta k_y \cdot \vec{e}_{y'}$. Within this geometry, the components Δk_x and Δk_y are obtained by:

$$\Delta k_x = 2k \sin \theta \sin \varphi \cos \left(\frac{\theta_{tot}}{2} \right) \quad (2.14)$$

$$\Delta k_y = 2k \sin \theta \cos \left(\frac{\theta_{tot}}{2} \right) \quad (2.15)$$

where $k = \|\vec{k}_i\| = \|\vec{k}_f\|$. This setup reaches a structural diffraction resolution of 0.135° in angle.

2.2.2 X-ray Photoelectron Spectroscopy (XPS)

Although second-derivative STS can measure chemical information of small organic molecules adsorbed on a metal surface through identification of adsorbate vibrational modes [40], chemical sensitivity for larger species and specially for supramolecular assemblies is still lacking in general. In this work, x-ray photoelectron spectroscopy (XPS) measurements are performed

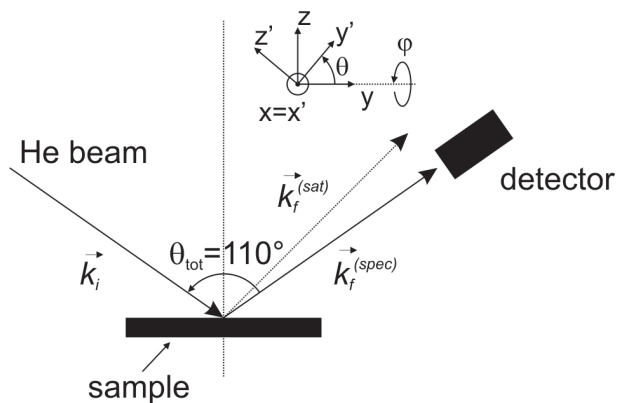


Figure 2.6: Schematic of the HAS setup geometry: incident He beam with momentum \vec{k}_i is elastically scattered at the topmost layer of the substrate. Scattered He atoms with momentum vectors satisfying Laue conditions in two dimensions generate a diffraction pattern of the periodic arrays on the surface.

in order to gain insight into the chemical state of the adsorbed amino acids. More specifically, we focus on the chemical environments of the oxygen and nitrogen electronic core levels in order to determine the oxidation and protonation states of the carboxylic and amino groups.

The physical concept behind XPS is the photoelectric effect explained by Einstein in 1905. According to this phenomenon, a photon with energy $h\nu$ can be absorbed by a material and eject an electron which is initially at a given energy level. The photon energy $h\nu$ is thus transferred to the electron, and, if $h\nu$ is large enough so that the electron can escape the material potential, measuring the kinetic energy E_{kin} of photoemitted electrons provides information about the initial state of the electron [88]. The electron kinetic energy E_{kin} is given by:

$$E_{kin} = h\nu - E_B - \phi \quad (2.16)$$

where ϕ is the material work function and E_B is the binding of the emitted electron, defined as the difference between the Fermi energy E_F and the energy of the initial electron state. The quantity $E_B + \phi$ corresponds to the energy which is required by the electron to escape the material. Figure 2.7 illustrates the photoemission process for a core-level 1s orbital electron and the respective E_{kin} XPS spectrum.

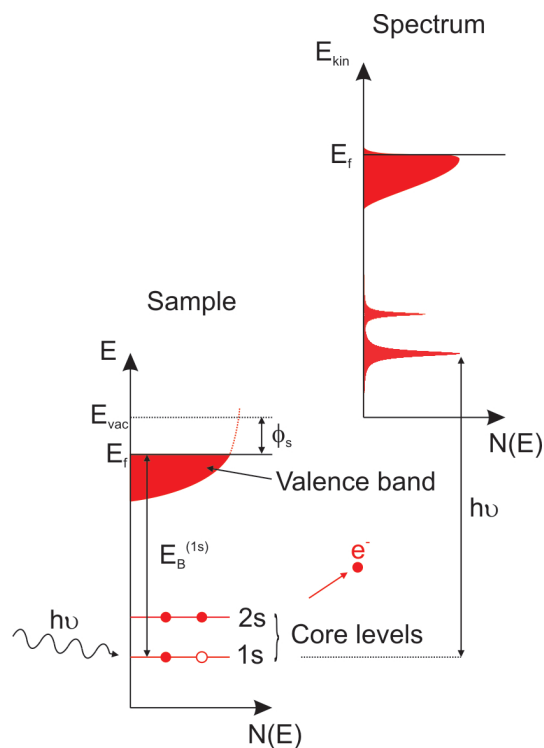


Figure 2.7: Schematic drawing of the x-ray photoemission process of a 1s core-level electron and its respective E_{kin} spectral signature.

In the case of core-level electrons, their local character in space and energy

makes their E_B a sensitive probe for the determination of their local chemical environment. Also, their value is specific for each atomic element, meaning that its measurement can lead to the determination of the oxidation and protonation state of a specific atom in the studied molecule. For instance, an atom from which a valence electron has been removed will have a slightly increased E_B for its core-level electrons, this due to a decreased screening of the positive nucleus Coulombic potential. These variations of E_B due to local chemical changes are called chemical shifts. On the other hand, the core-level binding energy E_B of a species adsorbed on a polarizable metal surface is also influenced by this adsorption. In fact, the substrate conduction electrons represent a supplementary Coulombic screening, inducing a decrease in the E_B of the core-levels. This effect of the substrate polarizability is dependent on the distance between the surface and the molecule. These changes in E_B can reach several eV's, and their measurement yields efficient determination of the chemical surroundings of the specific core-level electron.

Due to the large binding energy of core-level electrons, their photoemission requires x-ray radiation. In the case of our work, the monochromatic x-ray beam is produced by a synchrotron light source, taking advantage of the high-energy electromagnetic radiation of 2 GeV accelerated electrons [44]. The advantage of a x-ray beam generated by a synchrotron source with respect to a lab x-ray tube source resides in its high photon intensity, tunable photon energy, and high photon polarization (this high polarization is not required for XPS measurements, but it will be required for near-edge x-ray absorption fine structure experiments).

Although photons with an energy of the order of 1 keV have a penetration

depth in between 1 and 10 μm , this technique is extremely surface sensitive due to the fact that electrons with E_{kin} between 15 and 1000 eV have a mean free path of less than 10 Å. Therefore, mainly core-level electrons from atoms located near the surface are photoemitted outside the material and detected [37]. Moreover, the localization of the photoemission process at the surface is improved by working at grazing incident angles for the x-ray beam.

For a given photon with energy $h\nu$, the photoelectron current $I(E_{kin})$ composed of 1s photoelectrons with kinetic energy E_{kin} is proportional to the 1s photoemission process probability per unit time (i.e. probability per unit time that a 1s core level electron interacts with a photon of energy $h\nu$). This probability is given by Fermi's Golden Rule and yields $I(E_{kin}) \propto (2\pi/\hbar)|\langle\psi_{f,E_{kin}}|H^{ext}|\psi_i\rangle|^2\delta(E_f-E_i-h\nu)$, where ψ_i is the initial many-electron state with energy E_i , and $\psi_{f,E_{kin}}$ is the final many-electron state with energy E_f containing a 1s core hole and a free electron with kinetic energy E_{kin} . The perturbation potential H^{ext} arises from the photon-electron interaction and is given by $H^{ext} = (e/mc) \cdot (\vec{A} \cdot \vec{p})$ within an appropriate gauge choice, m being the electron mass, \vec{A} the vector potential operator and \vec{p} the momentum operator [88]. Within some approximations, this relation yields for the 1s component $I(E_{kin})$ of the photocurrent a Lorentzian relation with respect to E_{kin} whose width is related to the lifetime of the core hole in the final state.

In a XPS spectrum, the Lorentzian features of the 1s photoemission processes can be convoluted with other phenomena, hindering a straightforward interpretation. Secondary electrons emerging from electron-electron scattering processes or electron-hole relaxation often affect the photoelectron current. These secondary events can be discriminated by an appropriate choice

of $h\nu$ and the application of a retardation potential in front of the electron analyzer in order to disable the detection of low energy electrons. The spectra can be also disturbed by inelastic events such as 'shake-up' processes, where the photoelectron inelastically excites a valence electron into a unoccupied orbital (this is unusual, except in the case of a C 1s induced $\pi \rightarrow \pi^*$ excitation in aromatic systems). Splitting of the features due to spin-orbit coupling can also be detected sometimes. These effects must be taken into account in a rigorous analysis. Moreover, assuming similar process cross-sections, stoichiometries of atomic species in different chemical states can also be extracted from the intensities of the spectroscopic features.

The ALOISA beamline where the XPS experiments were performed allows tuning the photon energy in a 140-8000 eV range, with a photon intensity in the order of 4×10^{10} photons/(s · mm²). In our case, the spectra are acquired with an x-ray beam energy between 500 and 700 eV (the exact photon energy is specified for each experiment) and with a grazing incident angle of 3°. The electron analyzer is positioned in the plane of incidence at an angle of 45° with respect to the incident beam. The electron analyzer consists of a spherical deflection analyzer with a retardation potential applied before the spherical deflector. The energy resolution is of the order of 350-400 meV. The measurements are performed *in situ* with the sample held at 150 K in order to minimize the x-ray induced effects on the adsorbed organic molecules [89]. The presented 1s XPS spectra are given with respect to E_B and are fitted with Voigt functions, the latter corresponding to convolutions of a Lorentzian function with a Gaussian term. The Gaussian term emerges from the thermal broadening and instrumentation broadening of the

data. The binding energy E_B is derived from E_{kin} , $h\nu$ and the calibration of E_B with the Ag 3d ($E_B^{Ag3d_{3/2}}=374.3$ eV, $E_B^{Ag3d_{5/2}}=368.3$ eV [90]) and Cu 3p ($E_B^{Cu3p_{1/2}}=77.3$ eV, $E_B^{Cu3p_{3/2}}=75.1$ eV [91]) binding energy peaks in order to take account of the Fermi energy E_F .

2.2.3 Near-Edge X-ray Absorption Fine Structure (NEXAFS)

Another chemically sensitive x-ray absorption surface science technique is near-edge x-ray absorption fine structure (NEXAFS) spectroscopy. Like XPS, NEXAFS is a powerful tool to probe the chemical environment of the adsorbed species, but also intramolecular conformational aspects such as bond lengths and relative orientations of the different functional groups within a supramolecular self-assembly. In this thesis, NEXAFS is exploited in particular to estimate the relative orientations of π systems relative to the adsorption plane.

This method consists of measuring the absorption of an incident photon with energy $h\nu$ by a molecular electronic core-level within ~ 50 eV of the absorption edge (thus the name 'near-edge'). The interest in this near-edge portion of the absorption spectrum resides in the fact that it reveals the resonances due to electronic core-level excitations into unoccupied molecular orbitals induced by the photon absorption. These processes are highly sensitive to the orientation of the unoccupied orbitals with respect to the photon polarization, and therefore to the relative intramolecular geometry. Figure 2.8 depicts the near-edge x-ray absorption process by core-level electrons of a diatomic molecule. If $E_{\pi^*} \leq h\nu \leq IP$ (where E_{π^*} is the energy level

of the unoccupied π^* orbital and $IP = E_{vac} - E_{s1}$ is the ionization potential relative to the 1s core level with energy E_{s1}), the 1s electron has a probability of absorbing the photon and being promoted to the unoccupied π^* level. This absorption process is followed by the emission of a secondary Auger electron: a valence electron decays into the core hole and transfers this decay energy to another valence electron which is emitted, thus relaxing the final state. A NEXAFS spectrum consists of the intensity of these emitted electrons as a function of the photon energy $h\nu$. When $h\nu \gtrsim E_{vac}$, the 1s electron can be excited into an unoccupied σ^* 'virtual' bound state with σ symmetry, which is a continuum state just above the vacuum level E_{vac} having enough overlap with ordinary bound state orbitals [37]. These σ^* resonances have a much shorter lifetime than the π^* states. Now, if $h\nu \gg E_{vac}$, the 1s electron is directly photoemitted. Because we are interested here in the information of the σ and π systems of the adsorbed molecules carried by the secondary Auger electrons, it is important to discriminate inelastically scattered and directly photoemitted electrons by applying a retardation potential before the partial electron yield detection.

For a given photon energy $h\nu$, the NEXAFS partial electron yield intensity $I(h\nu)$ is proportional to the probability that a core-level electron in a ψ_i orbital absorbs the photon and becomes excited into an unoccupied molecular orbital ψ_f . This probability is given by Fermi's Golden Rule, and, within the one-electron dipole approximation, it yields $I(h\nu) \propto |\vec{e} \cdot \langle \psi_f | \vec{r} | \psi_i \rangle|^2 \delta(E_f - E_i - h\nu)$, where \vec{e} is the photon polarization vector defined as $\vec{e} = \epsilon \vec{\epsilon}$, $\vec{\epsilon}$ being the polarized photon electric field, E_f (E_i) is the energy of the ψ_f (ψ_i , respectively) state, and \vec{r} is the electron position

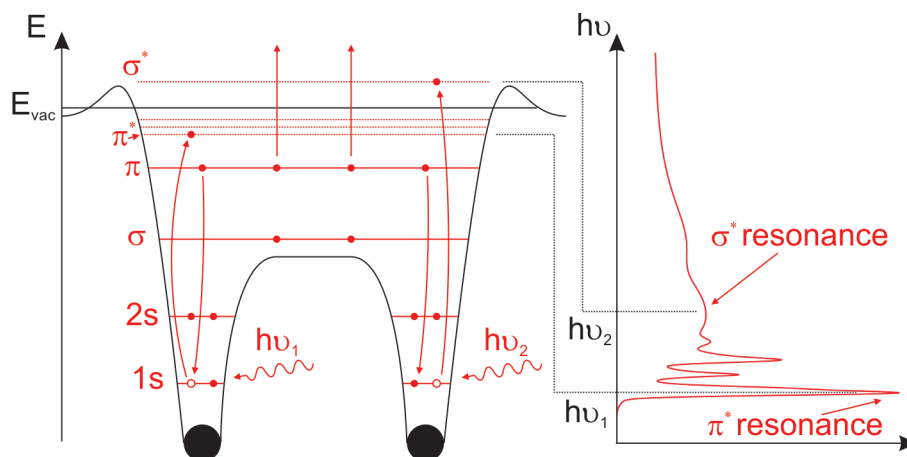


Figure 2.8: Schematic of the x-ray absorption process by a diatomic molecules of two photons with energy $h\nu_1$ and $h\nu_2$ inducing $1s \rightarrow \pi^*$ and $1s \rightarrow \sigma^*$ resonances respectively. The process is accompanied by the emission of two secondary Auger electrons. Graph on the right represents the corresponding partial electron yield NEXAFS spectrum.

operator. Within the context of this thesis, we focus on the C 1s absorption edge and therefore the state ψ_i corresponds to a 1s orbital with spherical symmetry. Hence, $I(h\nu)$ depends on the relative spatial disposition of the unoccupied state ψ_f with respect to the incident photon electric field $\vec{\epsilon}$. If the system is irradiated with a highly polarized x-ray beam where the direction of $\vec{\epsilon}$ is known, the value of $I(h\nu)$ can provide information on the orientations of the molecular orbitals and thus of the functional groups where these orbitals are located. For instance, let's consider an aromatic system absorbed on a substrate, γ being the angle between the substrate and aromatic planes. The aromatic system is composed of π^* orbitals which are oriented perpendicular to the aromatic plane and collinearly to a vector \vec{v} making an angle γ with the substrate plane normal. If the system is irradiated with linearly polar-

ized x-ray photons, the contribution $I_{1s \rightarrow \pi^*}$ of the $1s \rightarrow \pi^*$ resonance to I is given by Fermi's Golden Rule within the dipole approximation. In this case, this formalism yields $I_{1s \rightarrow \pi^*} \propto \cos^2 \delta$, where δ is the angle between $\vec{\epsilon}$ and \vec{v} . Now, considering a substrate with three-fold symmetry (as it is the case in this work) and defining $\vec{\epsilon}$ as $\vec{\epsilon} = \vec{\epsilon}_{p-pol} + \vec{\epsilon}_{s-pol}$ where $\vec{\epsilon}_{p-pol} = \|\vec{\epsilon}\| \cos \beta$ is the p-polarized component of $\vec{\epsilon}$ (i.e. the component in the incidence plane) and $\vec{\epsilon}_{s-pol} = \|\vec{\epsilon}\| \sin \beta$ is the s-polarized component (i.e. in the substrate plane), $I_{1s \rightarrow \pi^*} \propto \cos^2 \delta$ yields:

$$I_{1s \rightarrow \pi^*} \propto \cos^2 \beta \left(\frac{1}{2} \sin^2 \theta \sin^2 \gamma + \cos^2 \theta \cos^2 \gamma \right) + \sin^2 \beta \left(\frac{1}{2} \sin^2 \gamma \right) \quad (2.17)$$

where θ is the incident angle between the incident x-ray beam and the substrate plane. Hence, by identifying specific absorption resonances in the NEXAFS spectra and determining their dependence with respect to the known incident photon electric field, the orientation of the related unoccupied orbitals can be estimated. Here, a synchrotron x-ray source is required due to the necessity of tuning the photon energy and the photon polarization. In equation (2.17), a perfectly linearly polarized x-ray is assumed. In the case of the ALOISA beamline where the experiments are carried out, the x-ray polarization factor is 0.95. In our analysis however, we assume that this number is close enough to unity.

A normalization procedure for the NEXAFS data is required to avoid the fluctuations of the x-ray beam intensity with respect to photon energy and to eliminate the possible absorption signature of the x-ray optics. In our case, the presented NEXAFS spectra $I(h\nu)$ is treated as follows:

$$I(h\nu) = \frac{I^{sample}(h\nu)/I_0^{sample}(h\nu)}{I^{clean}(h\nu)/I_0^{clean}(h\nu)} \quad (2.18)$$

with I^{sample} being the measured NEXAFS signal for the adsorbed molecular species on a specific substrate obtained with an incident x-ray beam of intensity I_0^{sample} , and I^{clean} the NEXAFS signal for the same clean substrate irradiated with x-ray photons of intensity I_0^{clean} . The x-ray intensities I_0^{sample} and I_0^{clean} are measured with a photodiode. It is important that within the same normalization calculation all the signals are obtained with the same incident light polarization. Also, in order to avoid total reflection effects that could be different in the case of the adsorbed molecules and in the case of the clean substrate, the incident x-ray angle θ has to be larger than $\sim 5^\circ$. However, to maximize the surface sensitivity, it is appropriate to remain in grazing conditions. In our case, $\sim 7^\circ \leq \theta \leq \sim 10^\circ$.

A core-level NEXAFS spectrum, as the one seen in Fig. 2.8, consists in sharp features for $h\nu > IP$ and broader peaks for $h\nu < IP$. The pre- IP sharp peaks are assigned to isolated $1s \rightarrow \pi^*$ resonances. They can be approximated by Voigt functions where the Lorentzian term is dominant, their width being related to the lifetime of the excited state. Their sharpness and the dichroism that they can show with respect to the x-ray polarization make them good probes to analyze the spatial orientation of the functional groups on which they are located. The broad post- IP features are related to $1s \rightarrow \sigma^*$ shape resonances. Their broadening can be explained by two reasons: (i) the lifetime of the related excited states is much shorter than the one related to π^* resonances; (ii) they are convoluted with core-level excitations into continuum or quasi-continuum states. These features are usually approximated

by asymmetric Gaussian functions, the asymmetry being due to vibrational modes of the respective σ bonds. The position of these broad peaks with respect to photon energy $h\nu$ is an indication of the molecular bond length: the shorter the bond, the more confined the electrons become and therefore the higher σ^* is situated in energy. The core level excitations into unoccupied continuum states with a continuous density of states is translated in the NEXAFS spectra by the presence of a step-like function centered at IP . This continuous density of states onset can be approximated by an error function (i.e. erf function), which is actually the convolution between a Gaussian function and a step function. However, the exact position of this onset in energy is not obvious. In the case of the C 1s edge, which is considered in this work, the IP step function is centered around ~ 290 eV roughly. A comprehensive discussion of NEXAFS spectroscopy is found in [92].

The NEXAFS measurements in this work were performed at the ALOISA beamline in the same *in situ* UHV conditions as the XPS experiments. The sample was prepared identically as in the STM and XPS cases. In terms of x-ray induced damage on the adsorbed organic species, NEXAFS can have a significant influence due to the required long x-ray exposure of the sample. To minimize these effects, the measurements were performed with the sample at 150 K following a translation motion in order to obtain a signal from different unaffected sample regions. Because the monolayer case is considered for NEXAFS, we can assume that the signal is not locally dependent.

Chapter 3

Zwitterionic self-assembly of methionine nanogratings on the Ag(111) surface

The engineering of complex architectures from functional molecules on surfaces provides new pathways to control matter at the nanoscale. In this Chapter, we present a combined study addressing the self-assembly of the amino acid *L*-methionine on Ag(111). Scanning tunneling microscopy data reveal spontaneous ordering in extended molecular chains oriented along high-symmetry substrate directions. At intermediate coverages, regular biomolecular gratings evolve whose periodicity can be tuned at the nanometer scale by varying the methionine surface concentration. Their characteristics and stability were confirmed by helium atomic scattering. X-ray photoemission spectroscopy and high-resolution scanning tunneling microscopy data reveal that the *L*-methionine chaining is mediated by zwitterionic coupling, accounting for both lateral links and molecular dimerization, whereas C 1s near-edge x-ray absorption fine structure measurements support a preferential adsorption conformation with a non-flat disposition of the carboxylate plane. This methionine molecular recognition scheme is reminiscent of sheet structures in amino acid crystals and was corroborated by molecular mechanics calculations. Our findings suggest that zwitterionic assembly of amino acids

represents a general construction motif to achieve biomolecular nanoarchitectures on surfaces.

3.1 Introduction

The controlled self-assembly of functional molecular species on well defined surfaces is a promising approach toward the design of nanoscale architectures [15]. By using this methodology, regular low-dimensional systems such as supramolecular clusters, chains, or nanoporous arrays can be fabricated [93–97]. A wide variety of molecular species as well as substrate materials proved to be useful [98], exploiting non-covalent directional interactions including dipole-dipole coupling [93, 94], hydrogen bridges [95, 96, 99–102], and metal-ligand interactions [97, 103–107]. With the exception of multiple H-bonded networks or coordination networks incorporating metal centers, it remains challenging to realize robust systems, and there is a need to develop protocols exploiting stronger intermolecular bonds to realize purely organic low-dimensional architectures. Small biological molecules such as amino acids or DNA base molecules represent an important class of building blocks that are of interest for molecular architectonic on surfaces because they inherently qualify for molecular recognition and self-assembly [72, 74, 107–109]. The interaction between biomolecules and solid surfaces is decisive for the development of bioanalytical devices or biocompatible materials [28, 33, 110] as well as for a fundamental understanding of protein-surface bonding [111]. Moreover, in three dimensions the amino acids provide assets to engineer distinct network structures based on zwitterionic coupling schemes [112–114], which may be categorized as subclass of ionic self-assembly [115], and thus

are promising units to create robust nanoarchitectures. However, to date, the advantages of zwitterionic supramolecular synthons have not been exploited in two dimensions, although numerous studies on the adsorption of amino acids on metal surfaces have been performed [73].

In this Chapter, we report a low-temperature scanning tunneling microscopy (STM) investigation on the self-assembly of *L*-methionine on the close-packed Ag(111) surface under ultrahigh vacuum (UHV) conditions. The results demonstrate that the interplay between both molecule-molecule and molecule-surface interactions drives a previously uncharacterized methionine self-assembly scenario. We realized extended 1D biomolecular nanostructures of distinct widths and with tunable separation controlled by the molecular surface concentration. At intermediate coverages, molecular chains form striking methionine nanogratings, which are ordered mesoscopically in micrometer domains. Complementary helium atomic scattering (HAS) observations confirm the self-assembly characteristics and the high regularity of the gratings. O 1s and N 1s x-ray photoelectron spectroscopy (XPS) measurements were performed to determine the chemical nature of adsorbed *L*-methionine layers. They show conclusively that the organized molecules are in their zwitterionic state ($\text{CH}_3\text{SCH}_2\text{CH}_2\text{CH}(\text{NH}_3)^+(\text{COO})^-$); for a structure model of the neutral species, see Fig. 3.1. C 1s near-edge x-ray absorption fine structure (NEXAFS) experiments support a preferential adsorption geometry of the amino acid molecule with a non-parallel disposition of the carboxylate group with respect to the substrate plane. Molecular-resolution STM data demonstrate that the chaining reflects both a lateral coupling and a dimerization of *L*-methionine molecules involving the ammonium and carboxylate

groups. This methionine molecular recognition scheme is steered by site-specific bonding to the silver substrate and is reminiscent of sheet structures in amino acid crystals [113, 114, 116]. Elementary molecular mechanics calculations corroborate the associated 2D hydrogen-bonding pattern in which the ionic nature of the functional groups accounts for remarkably stable configurations. Because the intermolecular coupling is dominated by the amino acid functional moieties, it is expected that species with different side chains can be used in a similar manner. As such, zwitterionic assembly of amino acids represents a general motif to realize a new class of low-dimensional biomolecular nanoarchitectures.

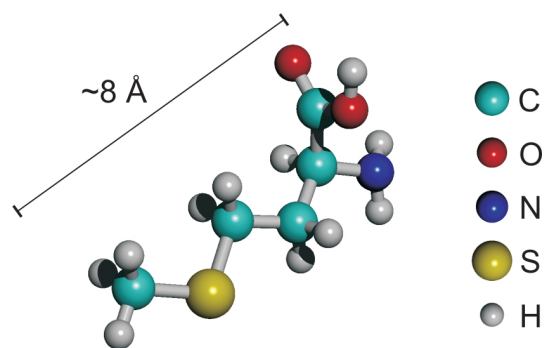


Figure 3.1: Structure model of *L*-methionine in its neutral gas phase state with color-coded atoms. The length of the molecule along its side chain is $\sim 8 \text{ \AA}$.

3.2 Experimental section

STM measurements were performed in a custom-designed ultrahigh vacuum apparatus equipped with a commercial Besocke-type low-temperature STM [84] and standard tools for *in situ* sample preparation and characterization.

All experiments were carried out at a base pressure lower than 3×10^{-10} mbar. The Ag(111) sample ($a_0 = 4.09 \text{ \AA}$ at 300 K) was polished chemomechanically and prepared in ultrahigh vacuum by repeated Ar^+ sputtering cycles at an energy of 0.8 keV and currents of typically $4 \mu\text{A}$, followed by annealing at a temperature of 770 K for ~ 10 min. The enantiomerically pure *L*-methionine and *D*-methionine molecules ($\geq 99.5\%$; Sigma-Aldrich, St. Louis, MO) were vapor-deposited onto the Ag(111) substrate from a glass crucible heated to a temperature of 370 K. During deposition, the substrate was held at a temperature of 320 K. The methionine coverage on the silver sample was derived from STM data and is given in terms of monolayers, where 1 ML corresponds to a saturated molecular layer completely covering the surface. All the molecular depositions exhibited in this Chapter are enantiopure i.e. preparations where both molecular chiralities are present simultaneously are not considered. STM topographic images were obtained with an electrochemically etched W tip, with the bias voltage applied to the sample. Data were recorded by constant-current imaging at temperatures < 15 K. All presented STM images were smoothed out by low-pass and inverse Fourier transform filtering to remove, respectively, the high-frequency noise and the harmonic noise created by external vibrations. XPS, NEXAFS and HAS measurements were performed at the ALOISA beamline (ELETTRA, Trieste, Italy), whereby deposition of methionine on Ag(111) was performed with the substrate held at room temperature. All XPS and NEXAFS spectra have been measured from a freshly deposited film and by keeping the sample temperature below 150 K to minimize the radiation damage. In fact, we observed that exposures to the synchrotron radiation beam causes molecular damage,

manifested in modification of XPS peak profiles [117, 118], which can be reduced to substantially lower rates when the sample is kept below 300 K [89]. The reported XPS spectra have been taken with an overall energy resolution of 300 meV [44] with a beam of photon energy 596.7 eV. The photon beam is characterized by a $\sim 4 \times 10^{10}$ photons/(s \cdot mm²) intensity and an elliptical photon polarization factor of 0.95 which we assume to be close to unity. The binding energy on the shown XPS spectra was calibrated with respect to the substrate Fermi level. The XPS raw data were treated by subtracting the background signal caused by inelastically scattered photoelectrons and fitting with Voigt peaks. C 1s NEXAFS measurements were performed on a saturated monolayer sample with an incident grazing angle of $\sim 9^\circ$. The respective spectra were normalized by dividing the saturated monolayer partial yield signal with the one of the clean substrate. The dependence of the C 1s NEXAFS signal with respect to the x-ray polarization was addressed by rotating the sample around the axis defined by the intersection of the incidence and substrate planes. The absolute photon energy was calibrated by identifying in absorption spectra the C 1s $\rightarrow \pi^*$ resonance of gas phase CO in the ALOISA ionization cell [44]. HAS data were obtained at room temperature with an incident He beam of energy 19 meV and wave vector 6.3 \AA^{-1} . For the molecular mechanics calculations, the software package HyperChem Professional 7.51 was used [119]. The optimal geometrical configuration for the isolated molecules was determined with the semiempirical MNDO/d method [120, 121]. The classical molecular mechanics MM+ [122] force field was used to determine the energy of the two-methionine system.

3.3 Results and discussion

3.3.1 Mesoscopic ordering and spectroscopic signature

Upon deposition of small methionine concentrations, STM observations show 1D features on Ag(111) terraces, reflecting molecular self-assembly. This finding is illustrated by the image reproduced in Fig. 3.2(b), taken for a coverage of ~ 0.05 monolayer (ML), showing 1D arrangements with discrete widths of 19 and 38 Å, respectively. The apparent height of these structures varies between 0.8 and 1.5 Å, depending on the applied imaging bias. Moreover, they exhibit striking extensions; for instance, the length of the right 38-Å-wide methionine stripe exceeds 180 nm. Three different orientations are found that follow the close-packed $\langle 110 \rangle$ high-symmetry substrate orientations (see the Fig. 3.2(b) inset in which the atomic structure of the Ag(111) lattice is depicted). This is a first indication that site-specific bonding at the surface is decisive in the observed *L*-methionine self-assembly scenario.

The molecular surface concentration plays an important role in the mesoscopic ordering and domain formation of the molecular stripes. Although at low coverages any orientation along the close-packed substrate is equiprobable, beyond a critical coverage of ~ 0.10 ML, domains with mutual alignment appear (see Fig. 3.2(b)), i.e., there is a mesoscopic ordering of the methionine stripes. In the data depicted in Fig. 3.2(b), the interstripe distances are in the 85-190 Å range, and their correlated orientation signals long-range interactions. The nature of these presumably indirect substrate-mediated interactions has not been totally identified, but the surface electronic structure, which notably includes the 2D Ag(111) surface-state free electron gas,

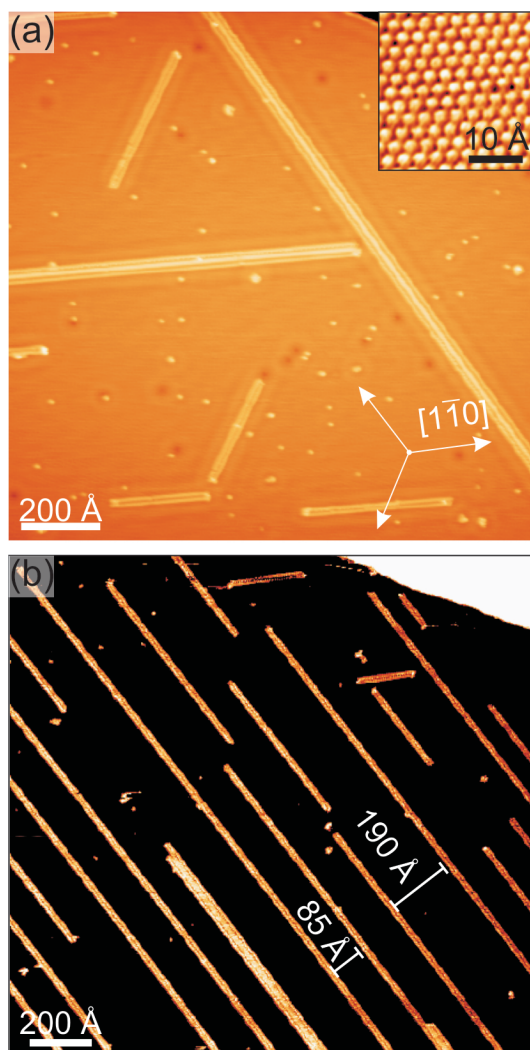


Figure 3.2: 1D ordering of the *L*-methionine amino acid on Ag(111). (a) STM topographic data show the *L*-methionine molecules self-assembling into extended 1D arrangements following the closely packed $\langle 110 \rangle$ orientations of the substrate ($I=0.7$ nA, $U=-120$ mV, $\theta \simeq 0.05$ ML, $\Gamma_{evap} \simeq 0.5$ ML/min). Inset: Atomic resolution of Ag(111). (b) On exceeding a critical coverage of $\theta \simeq 0.1$ ML, the correlated orientation of methionine stripes signals long-range repulsive interactions ($I=0.8$ nA, $U=-200$ mV, $\theta \simeq 0.12$ ML, $\Gamma_{evap} \simeq 2.4$ ML/min).

is expected to play a prominent role. Indeed, tunneling spectroscopy data evidence a striking 1D electron confinement and formation of quantum well states [123], which could mediate long-range interactions [98]. Related cases in which surface-state electrons drive adatom array formation [124, 125] and influence molecular ordering [126] on metal substrates have been reported, and it is likely that with the present system the surface states interfere in the molecular self-assembly. A detailed analysis of the surface electronic structure of the present system will be presented in the next Chapter.

On further increasing the coverage, the mesoscopic ordering becomes more regular. Thus, tunable and regular nanogratings can be fabricated. Figure 3.3(a) and 3.3(b) show two corresponding examples for coverages of ~ 0.15 and ~ 0.38 ML, respectively. In both preparations, all stripes have a single width of 38 \AA . The grating periodicity is 275 \AA (standard deviation $\sigma=40 \text{ \AA}$) in Fig. 3.3(a) and 94 \AA ($\sigma=9 \text{ \AA}$) in Fig. 3.3(b). The nanogratings order in regular domains extending in the micrometer range. An interesting application for these nanogratings with tunable spacing is their potential use as templates for the design of functional linear arrangements such as nanowires. The thermal stability of the nanogratings has been studied by STM for this purpose, with the outcome being that they are stable up to room temperature with molecular desorption occurring only above 370 K.

HAS experiments confirm the linearity of the *L*-methionine structures and the steering influence of the substrate symmetry on the molecular nanogratings. In fact, Fig. 3.3(c) shows the 2D HAS diffraction pattern of the amino acid self-assembly for a 0.6-ML coverage. The hexagonal shape reflects the hexagonal symmetry of the self-assembly, induced by the close-packed

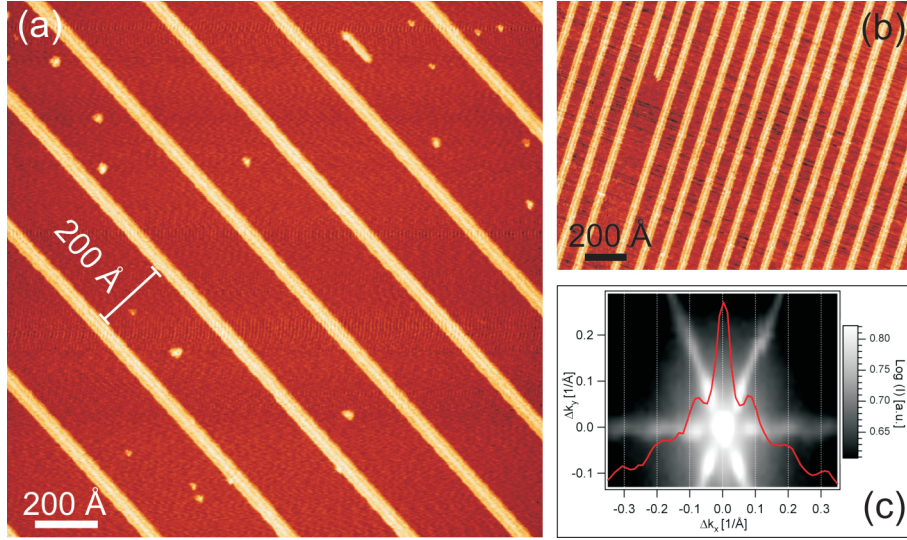


Figure 3.3: Tuning the self-assembly of 1D *L*-methionine nanogratings at intermediate coverages. (a) 275 Å ($\sigma \simeq 40$ Å) periodicity ($I=0.8$ nA, $U=-800$ mV, $\theta \simeq 0.15$ ML, $\Gamma_{evap} \simeq 1.8$ ML/min). (b) 94 Å ($\sigma \simeq 9$ Å) periodicity ($I=0.1$ nA, $U=-500$ mV, $\theta \simeq 0.38$ ML, $\Gamma_{evap} \simeq 0.8$ ML/min). (c) The 2D HAS diffraction pattern of the *L*-methionine deposition on Ag(111) (substrate held at 300 K during preparation, $\theta \simeq 0.6$ ML) shows the amino acid self-assembling after the six-fold symmetry of the underlying substrate. The red curve corresponds to a single scan at $\Delta k_y=0$. Symmetrically placed satellite peaks aside the specular peak demonstrate the periodicity of the nanogratings.

Ag(111) surface. Moreover, the diffraction motif confirms that the directions in which the supramolecular structures extend correspond to the $\langle 110 \rangle$ substrate orientations. The periodicity of the self-assembly attributable to interchain long-range interactions also is reflected in the HAS data. The red curve in Fig. 3.3(c) corresponds to a single HAS scan at $\Delta k_y = 0$. The off-specular diffraction appearing as symmetrically placed satellite peaks aside the specular peak is a complementary demonstration of the periodicity of the supramolecular arrangement. Finally, HAS substantiates the room tempera-

ture stability of the gratings, which is an important feature for their potential application as templating structures [127].

The quality of the nanogratings homogeneity is depicted in Fig. 3.4. Here, the probability of finding a given interchain spacing is given for different coverages from ~ 0.15 to 0.64 ML. The experimental data are fitted with Gaussian curves, showing sharp distributions for inter-row distances between ~ 20 - 200 Å and molecular coverages $0.15 < \theta \leq 0.64$ ML. For values of $\theta < 0.15$ ML, the standard deviation of the distribution increases dramatically from values between 5 - 8 Å to ~ 55 Å: the correlation between self-assembled biomolecular nanowires is lost due to large inter-row distances.

XPS measurements clarify the chemical state of the amino acid moiety. These measurements were performed for a saturated monolayer preparation and are expected to apply for the entire coverage range in which the same coupling motif is identified by STM throughout (see below). The N 1s and O 1s XPS spectra in Fig.3.5(a) and (b), respectively, show a single component at $E_{N1s} = 401.15$ eV and $E_{O1s} = 531.2$ eV, indicating a unique configuration of the amino acid. The observed energies are markedly shifted with respect to those expected for the neutral species. For comparison, XPS experiments performed on the *L*-cysteine/Au(110) system demonstrate that the N 1s spectra related to the neutral amino group NH_2 and the positively charged ammonium group NH_3^+ are characterized, respectively, by a peak at 399.5 eV and a peak at 401.5 eV. Moreover, the O 1s spectra of this same system show peaks at 531.2 eV, 532.3 eV, and 533.6 eV, with the first peak corresponding to the equivalent resonating oxygens of the carboxylate group COO^- and the two others corresponding to the chemically inequivalent oxy-

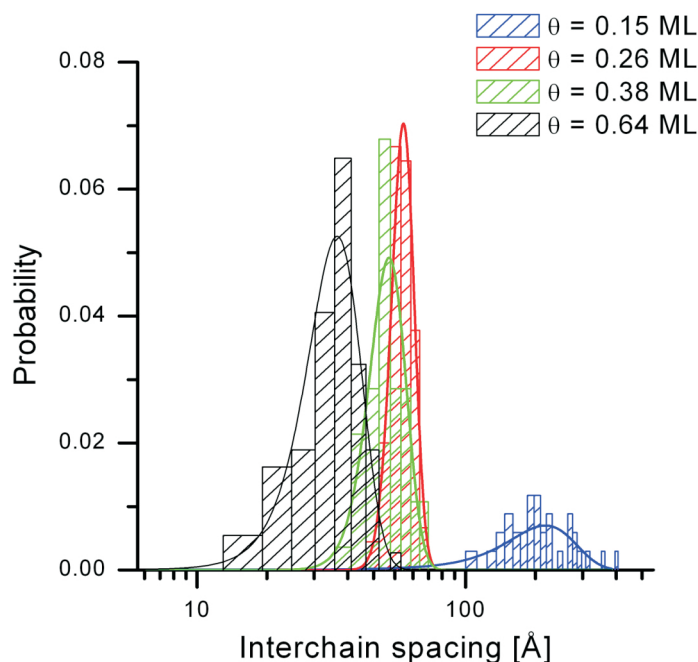


Figure 3.4: Statistics of the nanogratings spacing regularity. Probability of finding a given interchain spacing for θ between values of ~ 0.15 - 0.64 ML. Data is fitted with Gaussian curves. Standard deviation drops from ~ 55 Å to values between 5 - 8 Å for $0.15 < \theta \leq 0.64$ ML, showing the homogeneity of the nanogratings for these coverages.

gens of the neutral carboxylic group COOH [128]. Therefore, we deduce that the N 1s peak at 401.15 eV of our system represents a signature of the positively charged ammonium group NH_3^+ , whereas the singular maximum in the O 1s spectrum at 531.2 eV reflects the oxygen atoms of the carboxylate group COO^- i.e. the methionine molecules are in their zwitterionic state (the slight differences in binding energy are attributed to the different substrates; note that the superstructures occurring in the adsorption of cysteine on Au(110) imply both zwitterionic coupling schemes [128, 129] and substrate

reconstructions [130]). This interpretation is in agreement with observations on the cysteine of the Pt(111) system in which similar trends are encountered [131]. Regarding the side chain sulphur atom, S 2p XPS data showed a doublet at a binding energy of 163.9 ± 0.1 and 165.1 ± 0.1 eV, related to photoemission of the $2p_{3/2}$ and $2p_{1/2}$ core-levels respectively. These values differ from the *L*-cysteine/Au(110) system [117, 128] and show evidence of a non-covalent interaction between the sulphur atom and the Ag(111) surface. Nevertheless, the flat disposition of the adsorbed biomolecules observed in the molecular-level STM topographs below suggest that the sulphur atom might provide a physisorption contribution through its lone electron pairs to the bonding between methionine and silver. This non-covalent involvement of the thioether atom to the amino acid adsorption is in agreement with previous surface-enhanced Raman spectroscopy (SERS) results obtained for methionine in colloidal silver solutions [132–134].

C 1s NEXAFS measurements were carried out for a saturated *L*-methionine monolayer on Ag(111) in order to gain supplementary insight into the intramolecular chemical and conformational states of the adsorbed biomolecules. The high polarization factor of the incident x-ray beam allows addressing the polarization dependence of the C 1s NEXAFS signal and hence to probe features of the intramolecular geometry. Figure 3.6 displays the C 1s NEXAFS spectra for the p (red) and s-polarizations (black). Both spectra are characterized by a sharp peak at a photon energy of 288.5 ± 0.1 eV which we assign to the C 1s π^* resonance of the carboxylate group (label 3 in Fig. 3.6) [129, 135, 136], broad features in the 292.1–303 eV photon energy range (labels 4–6) and a pre-edge elbow at ~ 287.5 eV (label 2). Additionally, the

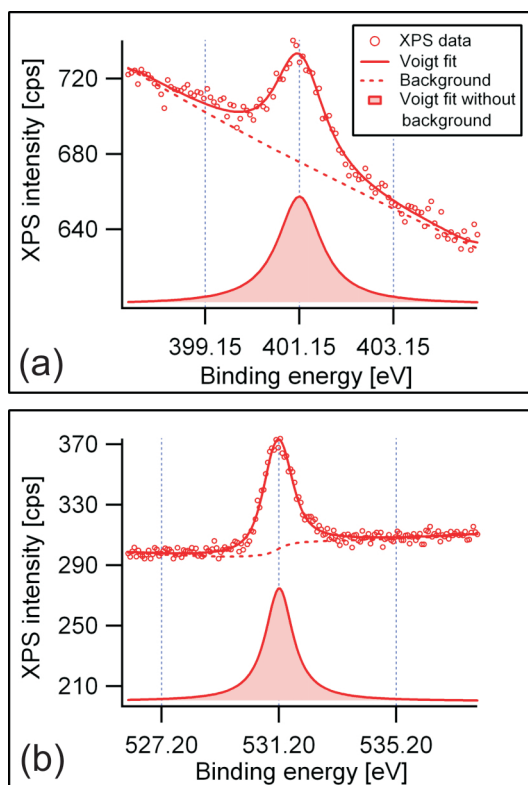


Figure 3.5: XPS measurements reveal zwitterionic amino acid assemblies on Ag(111). (a) N 1s signal with a singular peak at $E_{N1s} = 401.15$ eV, corresponding to a NH_3^+ ammonium group. (b) The O 1s spectrum shows only one peak at $E_{O1s} = 531.2$ eV, corresponding to the resonant oxygen atoms of the carboxylate group. Spectra were obtained for a saturated monolayer structure.

p-polarization spectrum exhibits a pre-edge feature at 286.2 ± 0.1 eV (label 1) which is absent in the s-polarization data. The data for both polarizations were fitted using the building-block approach [92] with a Voigt function for the carboxylate π^* resonance and five asymmetric Gaussian functions for features 1, 2, 4, 5 and 6. The s-polarization spectrum did not require a fitting curve for label 1. The parameters of this fitting procedure as well as

the chemical assignments for each feature are presented in Table 3.1. For the p-polarization (s-polarization, respectively) spectrum, an error function centered at 294.9 eV (294.6 eV, respectively) and with a step height of 0.19 a.u. (0.20 a.u., respectively) was considered in order to take into account the C 1s ionization potential (IP) onset. The discrepancies in photon energy for the peak positions between the p and s cases are due to fitting artifacts and also, in the case of post-IP features, to the intricate convolution between σ^* and continuum state resonances.

The chemical assignments of the different features were obtained through comparison in the literature with NEXAFS experiments performed on other amino acid systems [135, 135, 136]. The dichroism exhibited by the NEXAFS spectra reveals a preferential intramolecular adsorption geometry. In particular, the sharp C 1s $\rightarrow \pi^*$ resonance at 288.5 eV, characteristic of the carboxylate C 1s electrons, shows a strong beam polarization dependence. The inset in Fig. 3.6 displays this dependence of the carboxylate NEXAFS π^* peak amplitude I_3 with respect to β defined as the angle between the polarized photon electric field and the incidence plane ($\beta = 0$ corresponding to a p-polarized beam). Assuming that the x-ray beam presents perfect linear polarization, fitting $I_3(\beta)$ with equation (2.17) yields a value of $\sim 45^\circ \pm 5^\circ$ for the angle γ between the carboxylate and the adsorption planes: the carboxylate π system group is not adsorbed flat within the *L*-methionine supramolecular assembly.

Due to the convolution with excitations of the C 1s electron into unoccupied continuum states, the correlation between the polarization dependence of the broad post-IP features and the dichroism of independent σ^* resonances

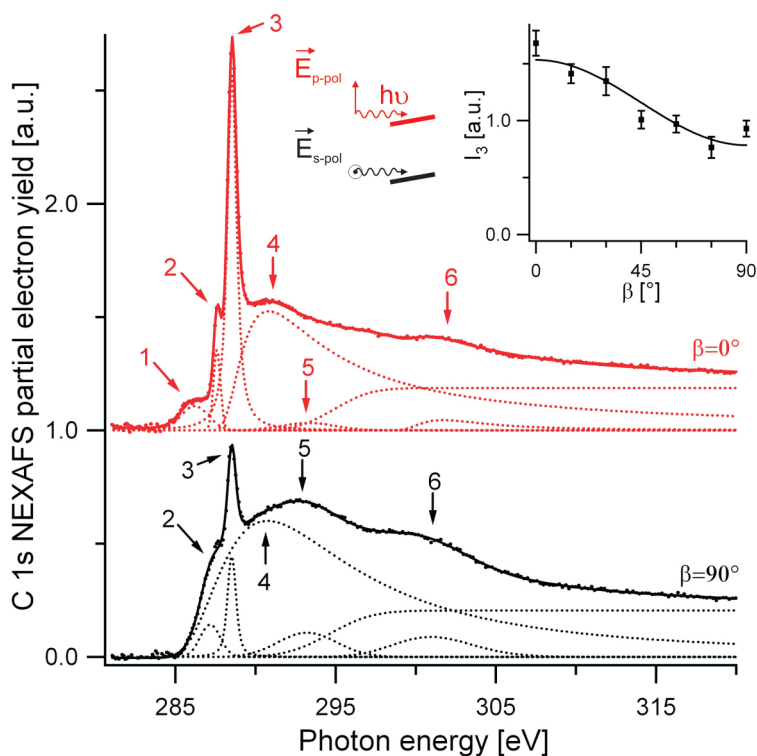


Figure 3.6: C 1s NEXAFS spectra for the saturated monolayer *L*-methionine/Ag(111) system for the p (red) and s-polarizations (black). Strong dichroism reveals a preferential adsorption conformation of the molecule. The sharp pre-*IP* peak corresponds to the carboxylate π^* resonance. Dots are the data points, solid line is the total fit curve, dashed lines are the individual fitting curves. Spectra are shifted for clarity. Inset: dependence of the NEXAFS signal I_3 related to the carboxylate π^* resonance with respect to the angle β between the polarized photon electric field and the incidence plane. Squares are data points, solid line is the fit curve relative to equation (2.17).

is not obvious. For instance, the broad features 4 and 5 in the ~ 292 - 293 eV photon energy window account for σ^* resonances related to C-C and C-N bonds. Their specific individual resolution, however, is hindered by the pres-

Table 3.1: C1s NEXAFS fitting parameters for the p and s-polarization spectra presented in Fig. 3.6. 'V' stands for Voigt function, 'G' for Gaussian.

Pol.	Peak position [eV]	Area [a.u.]	Assignment	Label
p	286.2	0.23 (G)	-	1
s	-	-		
p	287.6	0.19 (G)	C 1s \rightarrow σ^* (C-S)	2
s	287.2	0.23 (G)		
p	288.5	1.59 (V)	C 1s \rightarrow π^* (COO ⁻)	3
s	288.5	0.37 (V)		
p	293.4	7.03 (G)	C 1s \rightarrow σ^* (C-N) or	4
s	292.7	8.18 (G)	C 1s \rightarrow σ^* (C-C)	
p	293.3	0.14 (G)	C 1s \rightarrow σ^* (C-N) or	5
s	293.2	0.49 (G)	C 1s \rightarrow σ^* (C-C)	
p	302.6	0.30 (G)	C 1s \rightarrow σ^* (COO ⁻)	6
s	301.1	0.55 (G)		

ence of the IP onset in the same energy region. The σ^* resonances related to the carboxylate C 1s electrons, which show a larger binding energy, are correlated with feature 6 in the range \sim 301-303 eV. With respect to the pre-edge peak 1 appearing in the p-polarization spectrum, its chemical nature remains unresolved, but could be related either to a resonant signature of the C-S σ bonds or to a normalization artifact.

3.3.2 Molecular-level observations

The high-resolution STM data in Fig. 3.7 reveal the *L*-methionine positioning within the supramolecular structures. The stripes comprise elliptical features with a long axis of 8 Å, which corresponds to the extension of a single molecule along its side chain (see Fig. 3.1). Accordingly, these protrusions are identified with individual molecules bonding in a flat configuration to the

surface. The long axis of the methionine ellipses enclose an angle of $60^\circ \pm 5^\circ$ with respect to the stripe orientation (see Fig. 3.7(b)). Moreover, the separation between two adjacent molecules in this direction amounts to 5.8 \AA . This distance corresponds to twice the Ag(111) surface lattice constant (Ag atom nearest-neighbour distance 2.89 \AA ; see Fig. 3.7(b)) i.e. the substrate coupling also dictates the row periodicity.

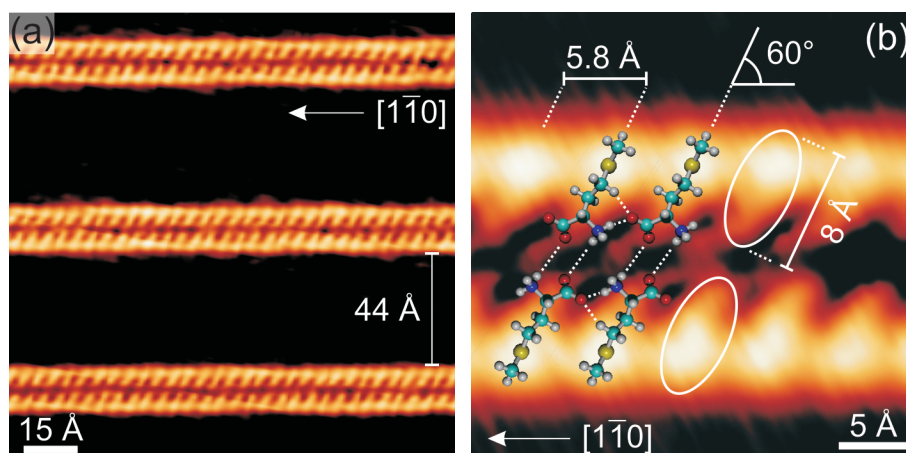


Figure 3.7: Molecular resolution imaging of double rows of *L*-methionine and parallel configuration. (a) Grating of double rows with $\sim 63 \text{ \AA}$ periodicity ($I=0.6 \text{ nA}$, $U=-500 \text{ mV}$, $\theta \simeq 0.12 \text{ ML}$, $\Gamma_{evap} \simeq 2.4 \text{ ML/min}$). (b) Individual molecules appear as elliptical features with a long axis of $\sim 8 \text{ \AA}$ arranged in pairs, with a lateral separation of 5.8 \AA corresponding to twice the nearest-neighbor distance between silver surface atoms. This separation and the 60° angle of the molecules with respect to the stripe orientation reflect the influence of the substrate on the molecular self-assembly ($I=0.9 \text{ nA}$, $U=-80 \text{ mV}$).

The methionine stripes forming the gratings present two discrete widths. The structures shown in Fig. 3.7(a) and 3.8(a) correspond to homochiral *L*-methionine systems and are 19 and 38 \AA wide, respectively. The molecular resolution data demonstrate that they consist of either double or quadruple

molecular rows in which the methionine is oriented at specific angles with respect to the stripe direction. In both cases, the same pairing scheme of the molecules can be discerned. This finding strongly indicates that the reactive amino groups mediate dimerization. Two different molecular configurations can be observed within a dimer. Either the axis of the molecules are parallel with respect to each other or they form an angle of $120^\circ \pm 10^\circ$ (chevron rows).

In Fig. 3.7(b), we depict a tentative model for the parallel molecular configuration, where dimerization between two amino acid zwitterions and lateral coupling are accomplished through hydrogen bonding involving the ammonium and carboxylate groups. Chemical and theoretical evidence concerning the detailed bonding geometry at the substrate is still missing, but NEXAFS data show that the carboxylate plane resides in an oblique fashion with respect to the surface. According to the S 2p XPS results, the sulfur atom may play a non-covalent role in the lateral or surface bonding through its lone electron pairs. A related zwitterionic bonding scheme was identified in the formation of layered amino acid crystals, where it is associated with appreciable bonding energies [113, 116]. As discussed below, this model is supported by molecular mechanics simulations. From an analysis of the molecular coupling scheme, we concluded that the bonding of the molecules is such that the H atom of the α -carbon (C_α) points upward with respect to the substrate. This state is designated 'up'-methionine, and its counterpart is obtained by flipping the molecule about its axis as 'down'-methionine.

Fig. 3.8(b) depicts the molecular arrangement in the chevron configuration, which cannot be explained by the exclusive coupling of up or down

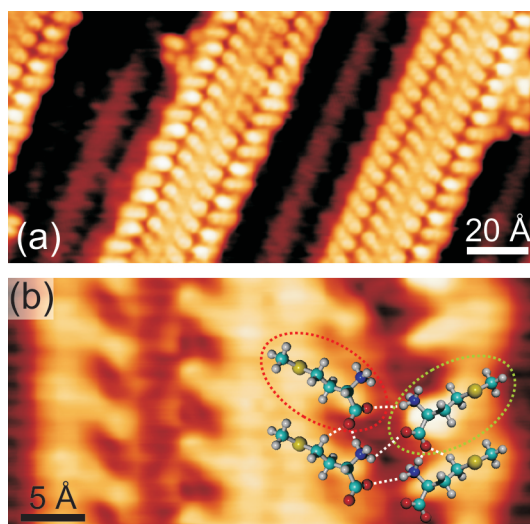


Figure 3.8: Quadruple *L*-methionine stripes and the chevron configuration. (a) Quadruple methionine rows with 30-Å spacing. Chevron and parallel mutual row orientations coexist ($I=0.65$ nA, $U=-1100$ mV, $\theta \simeq 0.50$ ML, $\Gamma_{evap} \simeq 3.0$ ML/min). (b) Quadruple molecular row with parallel and chevron configurations. The chevron dimers correspond to a 'down' molecule (green oval) bonded to an 'up' molecule (red oval).

species. This observation provides an intriguing possible explanation for the coexistence of the parallel and chevron rows in the nanogratings described above. The mirror symmetry of the latter with respect to the line defined by the molecular dimerization could naturally be explained by the pairing of a row of methionine molecules in the energetically preferred up configuration (circled in red in Fig. 3.8(b)) with another one in a down configuration (circled in green in Fig. 3.8(b)) being energetically close and where the lateral coupling would imply the changed orientation.

The quadruple rows correspond to a merging of two-molecule chains. Their formation cannot be explained in terms of lateral hydrogen bonding

(i) because the terminal CH₃ group at the tail of the molecules is unreactive and (ii) because wider stripes composed of an even number of molecules were not found to exist at intermediate coverages. We suspect the deposition coverage θ and the deposition rate Γ_{evap} to determine whether the double or quadruple row is more favorable. Although we could not establish reliable self-assembly protocols for the respective structures, we noted that annealing methionine gratings at $T \simeq 320$ K after deposition promote regular gratings with quadruple rows of up-configured methionine. Hence, stripes of double or quadruple molecular rows are very close in energy, and the latter must be stabilized by interactions beyond direct intermolecular coupling, presumably mediated by the electronic structure or elastic response of the substrate [98].

The chirality of the amino acid species is reflected in its self-assembly. This is observed in the parallel configuration of the molecular arrangement within the stripes: only one of the mirror-symmetric configurations is present in an enantiopure assemblage. In the case of an *L*-methionine homochiral preparation, the molecules are orientated with their axis at an angle of $+60^\circ$ with respect to the chain direction, whereas for a homochiral *D*-methionine system this angle is of -60° (see Fig. 3.9). This enantiomorphism of the nanostructure is only observed at the level of the molecular arrangement within the rows, the morphology of these being otherwise identical for both chiralities of the amino acid. Further studies to identify possible related chiral resolution processes in heterochiral preparations could be undertaken for this purpose [137].

Only with coverages exceeding ~ 0.65 - 0.70 ML do the methionine rows merge and highly anisotropic 2D molecular islands evolve. In Fig. 3.10(a),

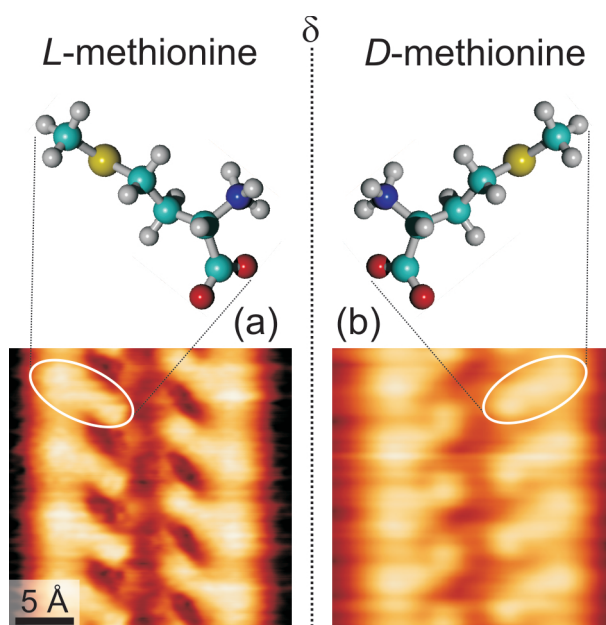


Figure 3.9: Enantiomorphism of the self-assembly in the parallel configuration. (a) Enantiopure *L*-methionine double row ($I=0.1$ nA, $U=-464$ mV). (b) Enantiopure *D*-methionine double row ($I=0.1$ nA, $U=-80$ mV). Both enantiopure assemblies are identical in their morphology, except in their intrachain molecular arrangement, where one is the mirror-image of the other.

the corresponding homochiral *L*-methionine saturated monolayer structure is depicted. The characteristic pairing feature readily identified above in the molecular stripes is identified again. In the corresponding model depicted in Fig. 3.10(b), the red circles represent the Ag(111) atomic lattice. The STM measurements do not allow for us to determine the exact adsorption sites of the molecules at the substrate. The sites on which the molecules are adsorbed in the model are arbitrary, the purpose being to determine the periodicity of the saturated molecular lattice with respect to the substrate periodicity. Considering the vectors \vec{a}_1 , \vec{a}_2 that define the unit cell of the Ag(111) lattice,

the lateral methionine ordering along the growth direction parallel to \vec{a}_1 is commensurate, whereas along \vec{a}_2 there is merely a higher-order commensurability. The vectors \vec{b}_1 and \vec{b}_2 defining the unit cell of the supramolecular lattice can be written as $\vec{b}_1 = 2\vec{a}_1$ and $\vec{b}_2 = -(5/2)\vec{a}_1 + (15/2)\vec{a}_2$. Hence, along the growth direction, the molecule is adsorbed at equivalent substrate sites, whereas within a given molecular dimer two molecules bond differently to the surface. Moreover, in the 2D saturated layer, the lateral molecular ordering is strictly parallel i.e. the chevron arrangements described above are absent. A regular parallel chiral ordering thus is favored in the formation of extended domains to which the methionine rows come in close proximity. In agreement, the orientation of the individual molecular rows at the interior of the quadruple arrangement always was observed to be strictly parallel. This interpretation implies, assuming structures of the chevron type may form transiently in the self-assembly, that a switching of the entire orientation of the molecules with respect to the substrate is possible (from down to up), which represents a generalization of the chiral switching phenomena of specific molecular groups observed recently [138].

3.3.3 Modeling the zwitterionic coupling scheme

To gain further insight into the nature of the 2D H-bonding with the present system, molecular mechanics calculations were performed for a pair of methionine molecules confined into a plane. The classical molecular mechanics force field results lend support to the proposed model for the molecular self-assembly. Only molecule-molecule interactions were taken into account in these calculations, neglecting the influence of the Ag(111) substrate on

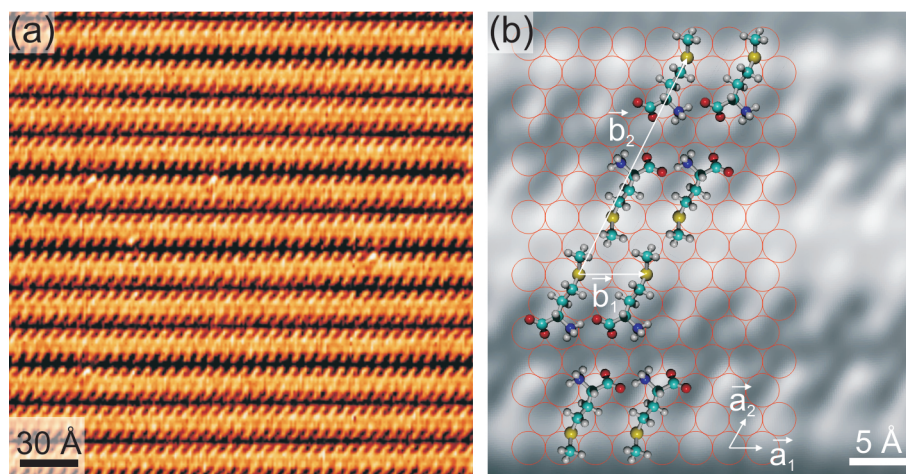


Figure 3.10: Two-dimensional commensurate layer structure. (a) Molecular resolution imaging of saturated *L*-methionine monolayer ($I=0.11$ nA, $U=-250$ mV). (b) Periodicity of the biomolecular self-assembly. The molecular ordering follows the atomic lattice of the Ag(111) substrate. Vectors (\vec{a}_1, \vec{a}_2) define a basis for the unit cell of the Ag(111) atomic lattice ($I=0.30$ nA, $U=200$ mV). The unit cell of the monolayer structure is marked in white.

the system, which is caused by the inaccuracy of a classical force field approach to describe surface-induced phenomena. The molecules were taken in their zwitterionic state, and conformational changes caused by molecule-molecule interactions were not considered. The STM data demonstrate that the molecules are lying flat on the substrate. If we assume that the adsorption is caused by interactions between the surface and the reactive sites of the molecules, the motion of the amino acid is restricted to the two translational degrees of freedom on the adsorption plane defined by the sulfur atom, the nitrogen atom, and one of the oxygen atoms of the carboxylate group. We considered a system composed of two *L*-methionine zwitterions, with their geometry independently optimized. The total energy of the system was de-

terminated with respect to the relative position of the two molecules in the adsorption plane.

Figures 3.11(a) and 3.11(b) represents total energy maps of the two-molecule system when the molecules are in antiparallel (i.e. one molecule rotated 180° on the adsorption plane with respect to other) and parallel configurations, respectively. The origin of the maps corresponds to the center of mass of one molecule, and the coordinates are those of the center of mass of the second molecule. The first map indicates that amino dimerization involving the carboxylate and ammonium groups is energetically favorable, supporting our model. The length of the resulting dimer is 18 \AA , which is in good agreement with the experimental data. The distance between a hydrogen atom of the ammonium group and an oxygen atom of the facing carboxylate group is 1.7 \AA , which is in agreement with the hydrogen bond length of 3D amino acids [113]. For comparison, the length of the same hydrogen bond in the tentative molecular arrangements shown in Figs. 3.7(b) and 3.10(b) is $\sim 3 \text{ \AA}$, which in the calculation still is associated with appreciable bonding. However, for the superposition of the STM data, molecules in an unrelaxed configuration were used under the condition that functional moieties reside on high-symmetry positions. A possible conformational adaptation could reduce the bond length significantly. On the other hand, it is feasible that under the influence of the surface the H-bond is stretched to allow for commensurability with the substrate atomic lattice [95, 139].

Furthermore, the calculation for the parallel configuration reveals that the lateral coupling proposed in our model also is energetically favorable (Fig. 3.11(b)). Intermolecular bonding involving the carboxylate group and

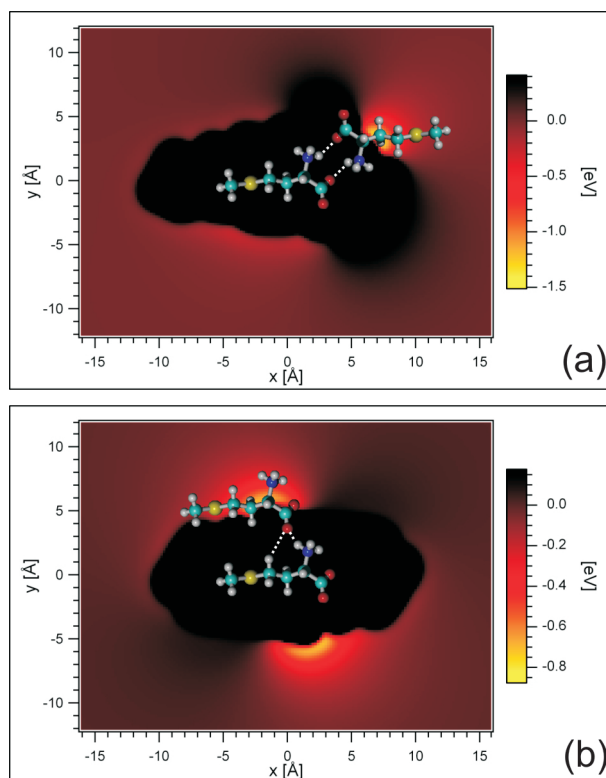


Figure 3.11: Total energy maps of a system composed of two interacting *L*-methionine molecules obtained with molecular mechanics calculations. The origin of the 2D plots is defined by the center of mass of the immobile molecule, and xy coordinates represent the position of the center of mass of the second molecule with respect to the immobile one. The color scale indicates total energy of the system versus the relative position between the two molecules. The energy of a non-interacting two-molecule system defines the zero of the energy scale. (a) Antiparallel configuration. Amino dimerization through zwitterionic bonding of self-complementary carboxylate and ammonium groups is shown. (b) Parallel configuration. Lateral hydrogen bonding involving ammonium and carboxylate moieties is shown.

the terminating methyl group of the side chain is very weak, as expected. Here, the hydrogen bond length between an oxygen atom of the carboxylate

group and a hydrogen atom of the ammonium group is 2.1 Å, whereas the hydrogen bond length between this same oxygen atom and the terminating methyl group of the side chain is 2.5 Å. All these hydrogen bonds are represented by dashed lines in Fig. 3.11, and the distances are in good agreement with those extracted from the tentative model based on the STM images (1.9 Å and 2.2 Å, respectively).

The combination of these results qualitatively supports our model for the molecular self-assembly and explains the formation of the double methionine rows. Furthermore, an additional stabilizing factor could result from cooperative effects, as demonstrated for example in the self-assembly of guanine on Au(111) in which resonance-assisted hydrogen bonding occurs [108]. Nevertheless, the existence of quadruple rows cannot be explained in this description and is associated with substrate-mediated indirect interactions, which should be considered in further experimental or theoretical studies. Notably, the interplay between surface electronic structure and molecular self-assembly remains to be investigated in depth. In particular, the influence of the biomolecular adsorption and self-assembly on the Ag(111) electronic properties will be discussed in the next Chapter.

It is of interest to point out that the described low-dimensional self-assembly is reminiscent of the layer structure observed in three-dimensional amino acid crystals, where the supramolecular structure is similarly given by hydrogen bridges linking zwitterions through their carboxylate and ammonium groups [112, 113, 140]. The results exposed in this Chapter illustrate thus the first steps of the amino acid crystallization at the molecular level.

3.4 Conclusion

This Chapter described the molecular self-assembly of the methionine amino acid on the Ag(111) surface. This system provides the possibility of engineering extended biomolecular nanogratings with tunable periodicity that are mesoscopically ordered in regular domains extending in the micrometer range. The long-range linear ordering and the molecular chaining appear as a result of the molecular confinement at the surface. The driving forces underlying the observed self-assembly scenario are a combination of site-specific adsorption, zwitterionic hydrogen bonding, and long-range indirect interactions. The stability of the biomolecular superlattices, up to room temperature, coupled with their remarkable tunable geometrical characteristics make them good candidates as organic templates for the design of functional 1D nanostructures or 3D amino acid sheet structures. Because the superlattice formation exploits essentially the functionality of the amino group, the rich chemical diversity of the side chains can be exploited to realize a variety of nanogratings. Altogether, our findings suggest that zwitterionic assembly of amino acids is a general motif to realize a new class of robust molecular nanoarchitectures on surfaces.

The results exposed in this Chapter were partially published in the journal *Proceedings of the National Academy of Sciences* [141]. The experiments were performed at the Advanced Materials and Process Engineering Laboratory (AMPEL) at the University of British Columbia in collaboration with Dr. A. Riemann, Dr. W. Auwärter, Dr. Y. Pennec, Dr. A. Weber-Bargioni and Dr. J.V. Barth, and at the ALOISA beamline of the ELETTRA synchrotron light source in collaboration with Dr. D. Cvetko, Dr. A. Cossaro,

and Dr. A. Morgante. We thank Roman Fasel for assistance with computational procedures for molecular mechanics calculations.

Chapter 4

Supramolecular gratings for tunable confinement of electrons on metal surfaces

Here we use the self-assembly capabilities of the methionine amino acid exposed in the previous Chapter as a novel bottom-up method for the fabrication of nanoscale confinement structures on the Ag(111) surface. Scanning tunneling spectroscopy data show that self-assembled biomolecular gratings act as one-dimensional resonators, and allow us to tune the characteristics of quantum-well states. We also demonstrate zero-dimensional confinement in quantum corrals down to $20 \times 50 \text{ \AA}^2$ in size by positioning single Fe atoms, which act as additional electron reflectors, in the molecular gratings.

4.1 Introduction

The control of electronic states in reduced dimensions has allowed researchers to explore and visualize fundamental aspects of quantum mechanics [142, 143] and has also led to new ideas for advanced materials and devices [144, 145]. In the particular case of noble metal (111) surfaces, the Schrödinger equation of the semi-infinite periodic crystal system allows a Bloch state solution which has a complex wave vector and an energy in the projected band gap at the Fermi level along the (111) direction (p. 367 in [146], p. 67 in [37], [147]).

The normalization of such state is possible due to the break of translational symmetry perpendicular to the surface, and the respective electronic probability density decays exponentially into the vacuum and into the bulk. In the case of Ag(111), such electronic state has a decay length of about 6 interatomic layers, corresponding to ~ 14 Å. Therefore, these electrons are practically localized at the surface. Due to the translational symmetry parallel to the surface, these so-called surface states behave as a two-dimensional free electron gas presenting a quadratic dispersion, which in the case of Ag(111) is characterized by an effective mass $m^* = 0.42m_e$ (where m_e is the electron mass) and a band energy onset $E_S = -67$ meV with respect to the substrate Fermi energy [56]. Because scanning tunneling spectroscopy (STS) permits accessing the local density of states of the observed surface with atomistic precision, the properties of the surface state band can be addressed [148], representing an interesting case for the fundamental investigation of quantum phenomena.

To date, two principal approaches have been pursued to confine and control electrons in two dimensions on surfaces. In the first, the scanning tunneling microscope (STM), in particular, has been used to create two-dimensional structures such as quantum corrals by moving individual atoms on metal surfaces and then probing the quasi two-dimensional surface state electron gases confined therein [57, 149–153]. However, this serial approach is time-consuming and not suited to producing ensembles of nanostructures for the control of electrons. A second method consists in confining the electrons by exploiting the periodic arrangement of atomic step arrays on vicinal substrates [144, 154–157]. The former concept has the advantage of possessing

utmost atomic precision, but is not suitable for the production of large quantities of quantum structures, and the latter offers only limited control over the structures. In the strategy presented here we take advantage of molecular self-assembly on surfaces [15, 95, 98] to create ensembles of regular and tuneable low-dimensional electron resonators.

Our STM observations in the previous Chapter revealed that the amino acid methionine spontaneously self-assembles into regular one-dimensional (1D) gratings and domain structures [141]. Methionine molecules were chosen because the sulphur atoms incorporated in the side chain can lead to appreciable surface interactions, but avoid the substrate reconstructions frequently encountered with S-terminated species. Underneath the adsorbed molecules the Ag(111) Shockley surface state is quenched. As a consequence, stripes of pristine Ag exist separated by highly regular linear molecular walls reflecting surface state electrons. The quantum well states associated with this one-dimensional confinement lead to characteristic changes in STS data at low temperatures. Furthermore, we succeeded in aligning single iron atoms on the Ag(111) stripes at low temperatures to produce a zero-dimensional (0D) system, and were able to fine-tune the spectroscopic signature of the remaining silver patches using atom manipulation techniques.

4.2 Experimental section

The measurements were performed in an ultrahigh vacuum (UHV) chamber equipped with standard tools for surface preparation and characterization and a low-temperature STM operated at $T \simeq 8$ K [84]. For the self-assembly, enantiomerically pure methionine molecules were vapour-deposited from a

glass crucible heated to 370 K onto the Ag(111) surface held at 300 K (both chiral species work equally well and lead to mirror-symmetric arrangements, as seen in the previous Chapter) [141]. Iron atoms were deposited by heating an Fe filament with the substrate held at $T < 10$ K and manipulated with the tip of our STM using standard techniques [57]. A tungsten (W) tip was employed, using the Ag crystal for tip forming. For constant-current imaging we used a sample bias in the +500 mV range and a 100 pA current. The STS measurements were typically acquired with a 3 mV r.m.s. modulation and a 20 ms time constant with 1024 initial points averaged to 200 points.

4.3 Results and discussion

4.3.1 1D electronic confinement by self-assembled biomolecular nanogratings

Figure 4.1 gives an overview of the tuneable confinement of the Ag(111) surface electrons by the use of self-assembled molecular reflectors. The electronic structure of the pristine surface (Fig. 4.1(a)) is illustrated by a STS dI/dV map overlaid on a constant-current topograph to emphasize the standing-wave pattern arising from the surface-state electron scattering at atomic step edges [148, 158]. The density of states (DOS) in large silver terraces resolved by STS (Fig. 4.1(b)) shows the characteristic step-like feature (~ 67 meV below the Fermi level) due to the onset of the Shockley surface-state band [56]. This two-dimensional (2D) electron system is first confined in one direction by a methionine superlattice. Figure 4.1(c) presents an STM topograph of an example of a self-assembled grating with ~ 60 Å periodicity. STS spectra taken between the molecular chains (4.1(d)) drastically differ from those

of the free surface and display the peaked features typical of an electronic system confined in one dimension [154]. A row of Fe monomers in a molecular resonator with 26 Å topographic width is depicted in Fig. 4.1(e) (there are stochastic deviations of the atom positions away from the centre line). This preparation adds a new level of confinement. Tunneling spectra taken between two atoms show peaks with Lorentzian-like shape typical of closed 0D resonator systems [159].

Similar to 1D supramolecular nanostructures self-assembled on Ag(111) in previous studies [99], the methionine gratings are highly regular and their periodicity can be simply tuned by the molecular surface concentration. They are realized in a single-step non-covalent synthesis procedure simply by directing a beam of pure molecules onto the well-prepared substrate. The resulting methionine superlattices are homogeneous, stable at room temperature, and consist of molecular chains following the substrates high-symmetry $\langle 110 \rangle$ crystallographic axes extending in micrometre-sized domains. The high-resolution STM in Fig. 4.2(a) shows the wire backbone consisting of a pair of protrusions, each of them with the expected 8 Å length for a single flat-lying methionine molecule. This conformation reflects a zwitterionic bonding scheme, discussed in detail in the previous Chapter and in [141]. The asymmetry of the protrusions at the wire outer edge might be due to the sulphur-mediated bonding to the Ag substrate, previously suggested from surface-enhanced Raman scattering [134]. The nearest-neighbour distance of laterally coupled molecules along the chains (5.8 Å) is twice the substrate atomic nearest-neighbour distance. Three different morphology regimes can be observed as the methionine surface concentration is varied between ~ 0.1

and 1 ML (where 1 ML corresponds to a surface completely saturated with a close-packed methionine layer). In regime I (0.1-0.5 ML), regular micrometer-extended gratings with periodicities from approximately 200 Å down to 60 Å

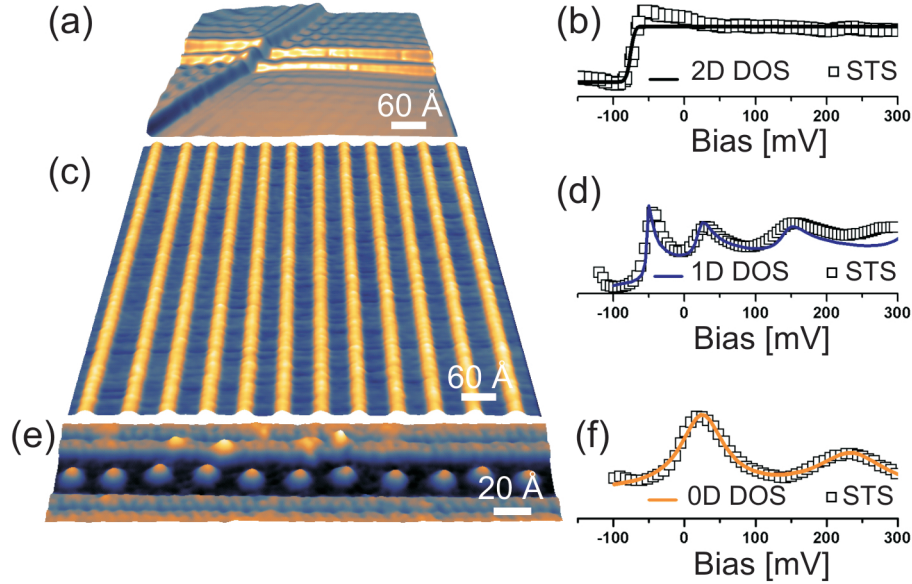


Figure 4.1: Standing waves of the Ag(111) surface state 2D electron gas (2DEG) and its confinement in one and zero dimensions by self-assembled molecular gratings and Fe atoms. (a) Topography of Ag(111) surface overlaid with a dI/dV STS map in order to enhance the standing wave pattern of the surface state electrons reflected at the step edges. (b) STS of the Ag surface state revealing the stepwise onset in the density of states typical for a 2D electron gas. (c) Self-assembled regular methionine grating on Ag(111). (d) Tunneling spectrum taken in between the molecular chains demonstrating the 1D confinement of surface state electrons. (e) Chain of Fe atoms in a molecular resonator. (f) Tunneling spectrum taken at Ag patches between Fe atoms revealing quantum corral formation. There is a continuous increase of the surface state onset energy with increasing confinement. The y-scale of (b), (d) and (f) is in arbitrary units. The Fermi level is at zero bias; the solid lines in (d) and (f) are best fits from models described below.

prevail. The overall excellent regularity of the gratings does not reflect a possible mesoscale distance quantization. However, the methionine rows occupy specific substrate bonding sites and thus are locally commensurate with the substrate atomic lattice. When the coverage exceeds ~ 0.5 ML (regime II), mesoscopic order is slowly lost and the formation of wider methionine ribbons occurs, which are separated by ~ 20 to 40 -Å-wide Ag stripes with regular boundaries. Even narrower silver bands down to a topographic width of 10 Å are found close to monolayer saturation between extended 2D methionine islands (regime III). The methionine superstructures are in registry with the substrate atomic lattice over the entire coverage range, as a result of which the same boundaries between molecular assemblies and free Ag surface areas are always present. It also must be noted that the 2D surface state electrons themselves mediate long-range interactions, which may represent a decisive factor for the self-assembly of both atoms or molecules [95, 125, 160]. With the present system substrate-mediated, indirect interactions can even be exploited to steer the alignment of atom rows, such as the one depicted in Fig. 4.1(e). However, here we focus on the net consequences for the surface electronic structure and quantum-well states without addressing details of the self-assembly scenario. This point will be discussed in detail in the next Chapter.

The data and analysis presented in Fig. 4.2 detail the properties of the 1D electron confinement. The molecular-resolution STM topograph in Fig. 4.2(a) depicts an element of a grating with 63 Å periodicity. In Fig. 4.2(b) we show the corresponding differential conduction map obtained by measuring a series of tunneling spectra in the voltage range -100 to 250 mV, at 100 positions

along the grating. The electronic ground level of the surface state at E_0 , with its characteristic single maximum, is clearly resolved. Similarly, the energy quantization and nodal structure of higher levels are directly visualized. In order to rationalize the systems electronic properties, the measured quantum confinement is modelled with a Fabry-Pérot interferometer. For the quantification of the methionine boundaries scattering properties (reflection amplitude and phase shift at boundaries) we follow the approach used by Bürgi *et al.* [58] to calculate the spatial variation of the surface DOS, which is expressed as:

$$\rho_{surf}(E, x) = \rho_b + \frac{\rho_{2D}}{\pi} \int_0^k dq \frac{2}{\sqrt{k^2 - q^2}} \times \frac{(1 - r^2)[1 + r^2 + 2r \cos(qL_{C1} + \varphi) \cos(q(L_{C1} - 2x))]}{1 + r^4 - 2r^2 \cos(2qL_{C1} + 2\varphi)} \quad (4.1)$$

where x is position, the wavenumber $k = \sqrt{2m^*(E - E_S)/\hbar^2}$, L_{C1} is the effective resonator width, $\rho_{2D} = m^*/(\pi\hbar^2)$ is the DOS of the pristine Ag(111) surface state electron gas and m^* is the effective electron mass. For the normalization procedure applied to the experimental spectra, we set the bulk contribution $\rho_b = 0$. $E_S = -67$ mV is the bottom of the surface state band and r and φ are the mirrors reflection coefficient and phase shift, respectively. Other than an unavoidable proportionality factor between STS and the real DOS, the model has four free parameters. First, systematic parameter variation for a series of resonators revealed that the reflection plane for the methionine wires appears located at the centre of the molecular wire, that is $L_{C1} = 63$ Å for the geometry in Fig. 4.2. One could have expected the

mirror plane to rather have been placed at the outer side of the rows where the sulphur interacts with the surface [134]. However, the effective reflection plane is located inside the molecular assembly, a behaviour similarly encountered with adsorbed single complex molecules [161] (with the present system the charge distribution associated with the zwitterionic coupling represents an additional factor). Second, the parameters φ and r play a very different role, allowing a confident separate fitting procedure for the data [58]. The positions of the peaks are strongly dependent on the boundary phase shift φ . Both peak broadening and oscillation amplitude depend predominantly on the reflection factor r . Altogether, the features of all experimental data are quantitatively reproduced for $\varphi = -\pi$ and an energy dependent reflection factor, which was determined to be $r \simeq 0.85$ at E_0 and follows an empirical $1/E$ decay law to reach $r \simeq 0.7$ at E_2 . The methionine boundary reflective characteristics are thus surprisingly similar to the ones reported for atomic step edges [58]. Nevertheless, not all 1D arrangements of scatterers on surfaces behave this way, and the tailoring of the confining barrier for surface states by step decoration has already been demonstrated [156, 162]. Accordingly, the use of methionine analogues holds promise for similar purposes, provided that the self-assembly characteristics can be sustained.

An essential feature of a quantum mechanical particle in a box model is that the energy levels obey an inverse quadratic dependence law on the confinement length. With the present self-assembled molecular resonators, this can be verified systematically over a wide range of lengths. A compilation of an extensive data set (more than 200 spectra acquired on different samples with different tips) where the surface state onset was extracted is represented

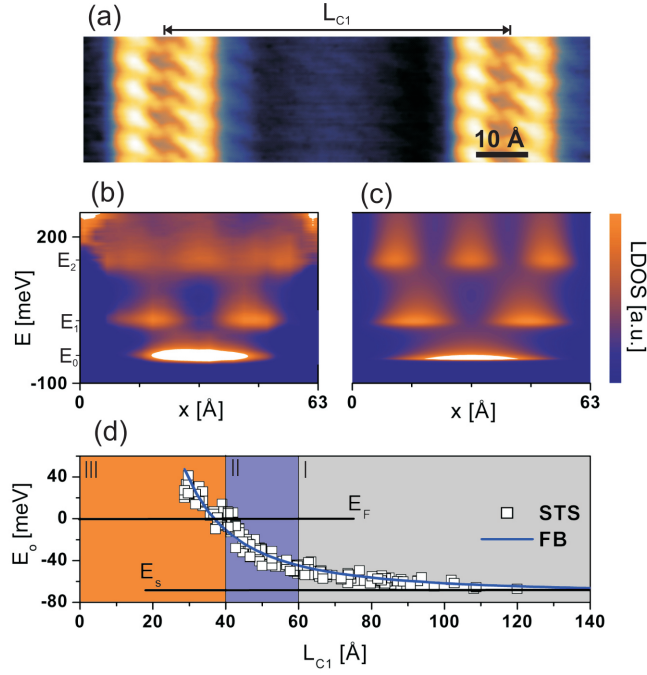


Figure 4.2: Quantum-well states in a molecular resonator. (a) High-resolution STM topograph of twin chain elements in a grating with individual methionine molecules resolved as rod-like protrusions. A model for the molecular arrangement within a nanowire is presented in the previous chapter. The actual confinement length (or equivalently, the effective width of the molecular resonator) L_{C1} is larger than the topographic width of the Ag stripe and the effective scattering plane for the electrons, as derived from the modelling, is located at the center of the wire. (b) Corresponding spatially resolved STS showing the first resonance of the surface state (E_0), and the energy level quantization and spatial nodes for resonances at higher energies (E_1 , E_2). (c) Quantitative description of the resonator by a Fabry-Pérot interferometer model. (d) The onset of the surface state can be continuously tuned by varying L_{C1} over the three morphology regimes (I, II and III) and follows an inverse square law. When L_{C1} falls below 38 \AA , the bottom of the first resonance is shifted above the Fermi level E_F . The blue line labelled FP describes the fit with the FabryPérot model described in the text. $E_S = -67 \text{ mV}$ is the bottom of the surface state band.

in Fig. 4.2(d). It reveals that the confinement characteristics are similar in all self-assembly regimes described above and follow the expected law: $E_0 = (\hbar\pi)^2/(2m^*L_{C1}^2) + E_S$, where E_S is the natural onset of the surface-state energy band, and $m^* = 0.4m_e$ the corresponding electron effective mass. Note that for resonator widths $L_{C1} < 38 \text{ \AA}$, the first resonance is shifted above the Fermi level, that is, the surface state is entirely depopulated, a behaviour similarly observed on narrow Ag(111) terraces [163].

In the silver stripes the electrons are free to propagate parallel to the molecular boundaries, and there is a continuum of states in this direction. Along the orientation of the resonator the dispersion relation of an unperturbed electron gas should thus prevail, and the band onset is defined by the resonator geometry. When an additional barrier is closing the resonator at one side, standing-wave patterns are expected that represent the lower-dimensional analogue of those encountered at atomic steps [148, 158](see also Fig. 4.1(a)). Such a situation is naturally occurring at rotational domain boundaries of methionine gratings. For the STM topograph in Fig. 4.3(a) we chose a particular location on the sample where a U-shaped confinement geometry is realized. This allows us to extract information about the propagative wavefunction within the resonator. In Fig. 4.3(b) an STS map of the interference pattern of the reflected electrons at the enclosure is shown, revealing the pertaining electronic DOS modulation. From the series of tunneling spectra taken at increasing distance from the scattering wall at the left compiled in the differential conductance map (Fig. 4.3(b)), the electronic dispersion curve is extracted by performing a 1D Fourier transform [164, 165]. The resulting dispersion curve in k -space depicted in Fig. 4.3(c) is parabolic,

with an effective mass of $0.43 \pm 0.04 m_e$, which is again in agreement with the properties of unconfined surface state electrons. Thus the molecular resonators have no effect on the 2D electrons other than confinement.

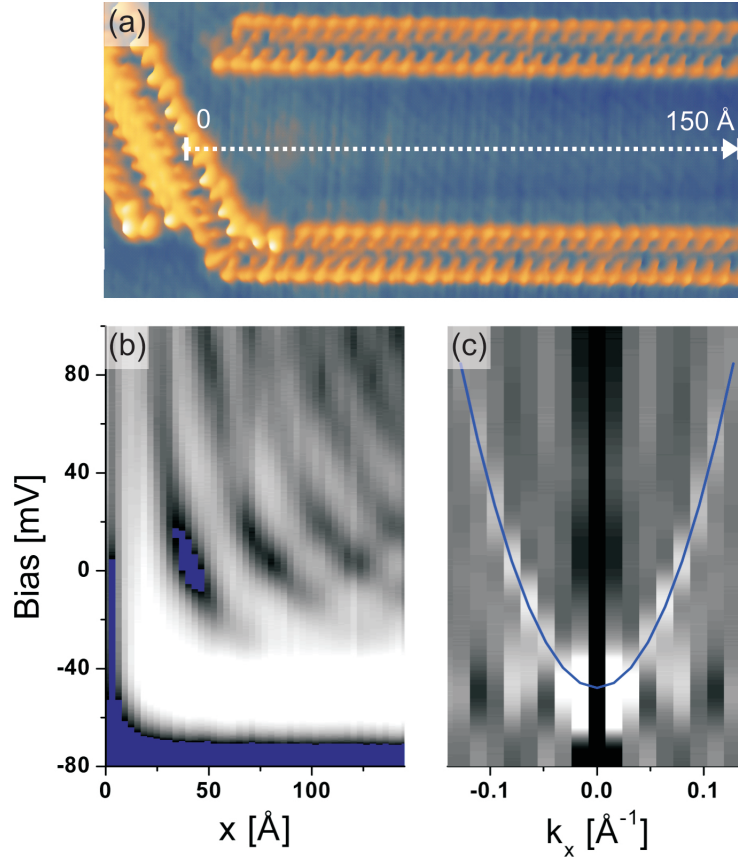


Figure 4.3: Reflection of electron waves freely propagating along molecular walls at a domain boundary. (a) STM topograph showing U-shaped confinement geometry at the intersection of two rotational methionine grid domains. (b) Spatially resolved STS map acquired along the 150-Å line indicated in (a) in the 80 to +90 mV range. (c) The corresponding 1D Fourier transform allows a straightforward visualization of the electron dispersion curve, which shows the quadratic signature of a 1D free electron gas highlighted in blue.

4.3.2 Zero-dimensional electron confinement by Fe adatoms

In a further step, we used single metal atoms to act on the one-dimensional electron gas in the Ag stripes. This procedure allows us to create one of the smallest man-made electron confinement structures to date in the form of $20 \times 50 \text{ \AA}$ quantum corrals. The approach is illustrated by the STM topograph in Fig. 4.4(a), where two iron atoms from a row thermally aligned (via indirect interactions [95, 125, 160]; this adatom alignment in the trenches is discussed more in detail in the next Chapter) along the central axis of a methionine resonator are highlighted (for an image of a more extended Fe atom chain, see Fig. 4.1(e); these data also reveal that a fraction of the co-adsorbed Fe monomers can stick right on the methionine gratings). In agreement with earlier observations [57], the atoms are found to be efficient scattering centres for surface-state electrons, where the distance between the Fe defines a second-level confinement length L_{C0} . The resulting consequences for the original 1D continuum states become apparent in the STS data.

In Fig. 4.4(e) we present two tunneling spectra acquired at and off the centre for a $40 \times 50 \text{ \AA}$ quantum corral. They both show well-defined peaks at 18 mV, which are fitted confidently with Lorentzians, conventionally associated with the broadening of 0D systems in general and closed surface state electron resonators in particular [159]. The STS dI/dV map acquired at the same bias as shown in Fig. 4.1(b) reveals a central maximum in the spatial electron density distribution associated with this state, which is consequently identified as the first resonance of the corral confining the electrons to a square-like geometry.

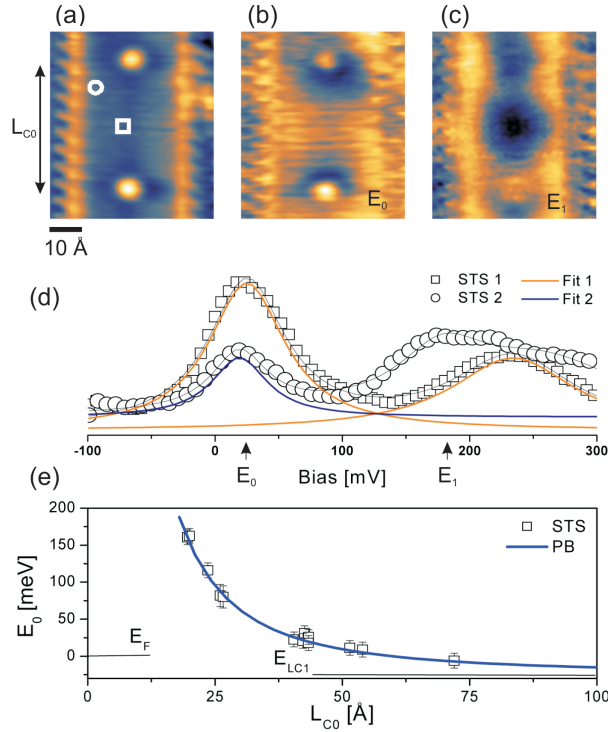


Figure 4.4: Zero-dimensional electron confinement in a quantum corral. (a) STM topograph showing two Fe atoms (orange/white blobs) aligned along the symmetry axis of a 40-Å-wide molecular resonator. The 50-Å interatomic distance L_{C0} defines the boundary of a 0D quantum well structure. (b),(c) STS dI/dV maps acquired at the first and second resonance showing the expected nodal structure. (d) Tunneling spectra at the two positions indicated in (a). The spectrum acquired at the well center (square symbols) can be deconvoluted as the sum of two Lorentzians (orange lines), typical for a quantum corral. In the off-centre spectrum (circles), only the first resonance has a Lorentzian shape. (e) The onset of the first resonance can be tuned by atom manipulation and obeys a particle in a box quadratic power law with varying L_{C0} (blue curve). E_{LC1} is the ground-state energy of the unperturbed 1D resonator. The blue line fit labelled PB describes the quadratic behaviour of a particle in a box model.

The second resonance occurs at 170 mV, where the STS intensity is maximum away from, and minimum at the center of the corral, respectively, as visualized in Fig. 4.4(c). The shown dI/dV map acquired at this second resonance reveals the expected central minimum. The shape of the off-centre tunneling spectrum is not as well described by single Lorentzians, which is attributed to the non-perfect symmetry breaking the degeneracy. Furthermore, the centre spectrum shows a second well-defined Lorentzian peak at 225 mV (the contrast asymmetry between top and bottom Fe atoms, particularly pronounced in the dI/dV map obtained at 170 mV suggests that the monomers are presumably adsorbed at two different substrate lattice sites that we could not determine exactly, and are not necessarily exactly centered in the molecular resonator).

Finally, in order to fully validate the proposed description, we systematically varied the spatial and spectral distribution of the surface-state electrons in the quantum corral by atom manipulation. Using established procedures, the confinement length L_{C0} was thus controlled in the 20-80Å range. The pertaining shifts of the first resonance as determined by STS are shown in Fig. 4.4(e) and demonstrate controlled population or depopulation of a quantum level at the discretion of the experimentalist displacing a single atom. Moreover, they again elegantly validate the expected quadratic dependence of a particle in a box ground-state energy versus resonator length, thus substantiating the interpretation of electron confinement in a quantum corral.

4.4 Conclusion

In conclusion, our findings demonstrate that the self-assembly of molecular superlattices on surfaces provides a novel and versatile approach to realize ensembles of low-dimensional quantum confinement geometries. It is suggested that this strategy can be widely applied to engineer electron wavefunctions in controlled nanoscale environments.

The results exposed in this chapter were published in the journal *Nature Nanotechnology* [123]. The experiments were performed at the Advanced Materials and Process Engineering Laboratory (AMPEL) at the University of British Columbia in collaboration with Dr. Y. Pennec, Dr. W. Auwärter, Dr. A. Weber-Bargioni, Dr. A. Riemann and Dr. J.V. Barth. We appreciate discussions with Dr. F. Baumberger, Dr. Th. Greber and Dr. G.A. Sawatzky.

Chapter 5

Self-alignment of transition metal adatoms in surface-supported biomolecular nanogratings

The spontaneous one-dimensional ordering of Co and Fe atoms adsorbed on Ag(111) in self-assembled methionine nanogratings was studied by means of low-temperature scanning tunneling microscopy. The transition metal species, evaporated *in situ* onto the methionine/Ag(111) system self-align upon annealing to $T > 15$ K into homogeneously distributed chains in the nanoscale biomolecular trenches, with an interatomic spacing of ~ 25 Å. For Co, the dynamics of the self-alignment was monitored, revealing a markedly reduced mobility in comparison with isolated Co atoms on the pristine substrate. The effect of the electronic surface states on the atomic self-alignment is revealed by tunneling spectroscopy mapping and *ab initio* calculations.

5.1 Introduction

The prospective design of functional devices at the nanoscale requires exquisite control of matter at the molecular and atomic level. Notably the direct investigation of self-assembled supramolecular architectures on solid surfaces yields a promising approach for bottom-up methodologies in nanoscience [94–

96, 141]. The procedure here consists in predefining a system composed by specific substrate, molecular species and/or adatoms which, through their inherent chemical and electronic characteristics in combination with external controlling parameters, mediate a desired equilibrium configuration [15, 98]. With appropriate self-assembly protocols it is possible to engineer low-dimensional nanostructures such as hydrogen-bonded one-dimensional molecular gratings [95, 141] or 2D metal-organic coordination networks [103, 166], whereby nanoporous systems can be realized serving as specific templates to accommodate and organize functional guest molecules such as fullerenes [97]. The chemical functionalities and molecular recognition capabilities of the adsorbed building units play a key role in such systems by mediating selective hydrogen bonding and metal centre coordination, as well as dipole-dipole or other Coulombic interactions [95, 141]. Moreover, the supporting substrate, through its crystal structure, defects, chemical nature and electronic properties, is a critical element in the relaxation of these systems. A particularly interesting case is the one of close-packed noble metal surfaces, whose surface electronic configuration steers dramatically the dynamics and final state of the adsorbed species. Notably, the influence of the surface state band on atomic self-ordering on metal surfaces has been extensively studied in the past, both experimentally [80, 97, 167, 168] and theoretically [125, 160, 169–173], including the consideration of adatom organization in quantum corrals [171, 174]. Adsorbed molecules and atoms, and other defects such as step edges, perturb the surface electronic states by scattering and confining the substrate electrons [57, 58, 174], which can even lead to partial or total depopulation of the band by regular superstructures [58, 123].

Tuning the substrate surface state band by electronically confining nanotemplates of well-defined morphology can add a supplementary control parameter to develop novel self-assembly methodologies.

In this Chapter we present a low-temperature scanning tunneling microscopy (STM) and spectroscopy (STS) study of the self-alignment of Fe and Co adatoms in regular methionine biomolecular nanogratings on Ag(111). The transition metal species, which are immobile in the trenches at low temperature, are found to spontaneously order into 1D chains once thermal diffusion is allowed, which could be directly monitored at temperatures between ~ 16 and 18 K. Within these 1D nanostructures, the metallic atoms are regularly distributed following a non-random trend: we find for the Fe chains a most probable nearest-neighbor distance of 23 Å, whereas for Co it is of 25 Å. These values reveal a long-range interaction which is mediated by the electronic structure of the underlying Ag(111) substrate, similar to findings for 2D hexagonal atomic lattices [80, 167, 168]. For the case of the Co, the dynamics of the ordering process could be monitored: the adatoms start diffusing at 15 K, align into a 1D chain at 18 K, whereby their motions obey an Arrhenius law with a decreased mobility in comparison with isolated adatoms on the bare Ag(111) substrate. This restrained atomic motion appears in our experimental measurements of the hopping rates. The one-dimensional self-ordering is associated with long-range row-adatom and adatom-adatom interactions mediated by the Ag(111) surface state electrons. To test this hypothesis, we model the respective interaction potential mediated by the substrate electronic configuration using the KKR Green's function method [125, 169–173], providing a very satisfactory

agreement with the experimental data.

5.2 Experimental section

The experiments for this study were carried out in a custom-designed ultra-high vacuum (UHV) chamber operating at a base pressure of $\sim 2 \times 10^{-10}$ mbar and equipped with a commercial He bath-cryostat low-temperature STM [84]. The sample preparation was performed *in situ*: the chemomechanically polished Ag(111) monocrystalline substrate (lattice constant: 2.89 Å at 300 K) was cleaned by repeated Ar⁺ sputtering cycles at an energy of 0.8 keV and currents of typically 4 μA, followed by annealing at a temperature of 770 K for ~ 10 min. The enantiopure methionine amino acid molecules (purity $\geq 99.5\%$, Sigma-Aldrich) were vapor-deposited onto the Ag(111) substrate by heating at a temperature of 370 K, with the substrate held at 320 K. After preparation, the sample is cooled down to $T < 10$ K for Fe or Co adatom deposition, and STM and STS measurements. The Fe and Co adatoms are deposited *in situ* by evaporating onto the sample from a properly degassed pure filament of respectively Fe and Co wound around a W wire. The metal adatoms are evaporated onto the substrate at 8 K. The STM and STS data are obtained with an electrochemically etched W tip, with the bias voltage applied to the sample, and in a temperature range from 8 to 18 K, the sample temperature being controlled with a Zener diode. STM topographical images correspond to constant-current data. The dI/dV maps are obtained with a lock-in technique, with measurements typically performed with a 5 mV rms, a ~ 3 kHz modulation, and a time-constant of 20 ms. STM and STS data were treated with the WSxM software package [86].

5.3 Results and discussion

5.3.1 Non-random 1D self-alignment of metal adatoms

As seen previously, the methionine amino acid deposited onto a Ag(111) substrate at ~ 320 K self-assembles into regular 1D nanogratings which follow the $\langle 110 \rangle$ crystalline orientations of the underlying substrate. Figure 5.1(a) recalls the amino acid arrangement within a double *L*-methionine chain, where the molecules are in their zwitterionic chemical state. The supramolecular 1D nanostructures consist in molecules dimerizing and bonding adjacently through hydrogen bonds involving the carboxylate and ammonium groups, respectively. These 1D biomolecular rows spread in unidirectional mesoscopic domains reaching several μm^2 . For molecular coverages between 0.1 and 0.6 ML, the interchain separation can be tuned between widths of 20 to 200 Å. The amino acid species are thereby in their zwitterionic chemical state, and the supramolecular 1D nanostructures consist in molecules dimerizing and bonding adjacently through hydrogen bonds involving the carboxylate and ammonium groups. Double or quadruple molecular rows coexist in the shown assembly, quadruple rows corresponding to two merged double chains. As seen in Chapter 3, the difference between the *L*-methionine and *D*-methionine homochiral self-assemblies is exclusively in the intrachain molecular arrangement: the *D* molecular dimer is oriented at a -60° angle with respect to the 1D chain growth orientation, whereas the *L*-dimer forms an angle of $+60^\circ$. Otherwise, the morphology of the *L* and *D* self-assemblies are identical, as well as their influence on the electronic properties of the Ag(111) surface. Consequently we do not specify the chirality characteristics of the systems

investigated in the following. In this study, only results related to homochiral preparations are presented.

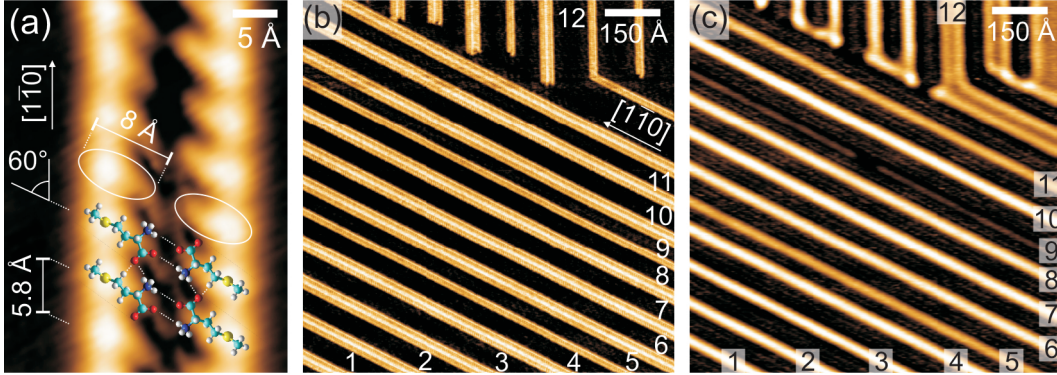


Figure 5.1: STM and STS data of the methionine biomolecular nanogratings on Ag(111) and the influence on the substrate electronic structure. (a) STM topographical data of the biomolecular arrangement within a *L*-methionine nanowire ($I=0.9$ nA, $U=-80$ mV). Color code for the molecular model: cyan(C), blue (N), red (O), yellow (S) and white (H). (b) STM image of a methionine nanograting with bare Ag(111) trenches of average width ~ 45 Å i.e. confinement length of ~ 65 Å. The bare Ag(111) trenches in between the biomolecular rows are numbered from 1 to 12 ($I=0.1$ nA, $U=-34$ mV, $\theta=0.43$ ML). (c) STS dI/dV map of the methionine/Ag(111) system in (b) imaging occupied states at -34 mV bias ($I=0.1$ nA): the substrate surface electrons are confined in the undecorated Ag(111) trenches. Brighter color corresponds to higher dI/dV signal, thus higher electronic density of states.

Figure 5.1(b) depicts a topographical constant-current STM image of a self-assembled regular methionine nanograting. Thinner and wider stripes correspond respectively to double and quadruple biomolecular chains. The black colored strips are bare Ag(111) trenches (numbered from 1 to 12). Here, the average width of these trenches is 45 Å, which corresponds to an electronic confinement length of ~ 65 Å. The amino acid self-assembly perturbs the electronic properties of the underlying Ag(111) substrate by

locally quenching the surface state. The surface state electrons thus become confined into the bare patches of silver: the biomolecular trenches act as nanoscale quantum resonators. We recall from the previous Chapter that the density of states of the confined surface state electrons are modeled by the Fabry-Pérot theoretical formalism, and the definition of what we call the electronic confinement length (consisting in the length between the middle of two adjacent double methionine rows) is extracted from this model. The local density of states of the system is visualized in the STS dI/dV map in fig. 5.1(c) obtained at -34 mV, where brighter color corresponds to higher dI/dV signal, thus higher electronic density of states: we observe in the trenches the electronic resonant modes caused by the electronic surface state confinement, whereas this surface state is clearly quenched beneath the biomolecular rows. The confined surface state band is shifted following a quadratic trend with respect to the confinement length, analogous to the quantum particle-in-box system. In trench 9 for example, no electronic state is observed: the trench being too narrow, the surface state onset is above the energy of -34 meV corresponding to this dI/dV map. On the other hand, we observe in the wider trench number 12 two maxima for the surface electronic density, corresponding to the second resonant mode. In general, the STS data reveal the remarkable homogeneity of the surface density of states within the individual trenches.

After characterizing the molecular assembly, Fe or Co adatoms are deposited onto the methionine nanogratings on Ag(111) *in situ*, with the system held initially at 8 K. The adatom coverage of both Co and Fe is typically chosen to be approximately 5×10^{-3} ML. First, we concentrate

on a dataset where the Co metal atoms were evaporated onto a methionine/Ag(111) preparation with a molecular coverage θ of 0.42 ML, corresponding to an average biomolecular trench width of 35 Å with standard deviation of 2.9 Å. Herewith we illustrate the dynamics and self-alignment process of the metal atoms in the bare Ag(111) trenches in between the biomolecular nanogratings. Figure 5.2(a) shows a STM constant-current topographic image at 12 K of a 35 Å wide trench with Co adatoms on the Ag(111) patch. At this temperature, both Co and Fe single adatoms are 'frozen': they start to diffuse at a temperature of 15 K. During surface atomic diffusion, the experimental observation reveals hopping lengths of single Ag(111) lattice units. This demonstrates that the adatoms prefer specific adsorption with respect to the underlying substrate, which is in agreement with previous theoretical studies of other adatom/substrate systems [175]. When annealed at 18 K, the adatoms diffuse and self-arrange into 1D ordered chains in the middle of the trench, without forming any dimers or clusters.

Figures 5.2(a) to 5.2(e) illustrate this self-ordering process of originally randomly distributed Co adatoms into regularly ordered 1D metallic chains (the single protrusions at the methionine rows are captured Co atoms that serve simultaneously as markers). The positioning of the atoms in the center of the trench, and the regular spacing between the species reveal a mesoscale interaction with the biomolecular rows and in between the adatoms respectively.

The Fe alignment in Fig. 5.2(f) was obtained with a preparation with molecular coverage θ equal to ~ 0.60 ML, giving substrate trenches with an average width of 25.5 Å and standard deviation 5.0 Å. It reveals a regularly

ordered Fe chain at 12 K, after being annealed at 18 K: the initially frozen and disordered system diffuses at 18 K, organizes in a dynamic equilibrium dictated by Boltzmann statistics. Upon cooling, the single atomic species are trapped in the local minima of the 2D energy landscape imposed by the supporting substrate atomic lattice and the nanoscale local environment.

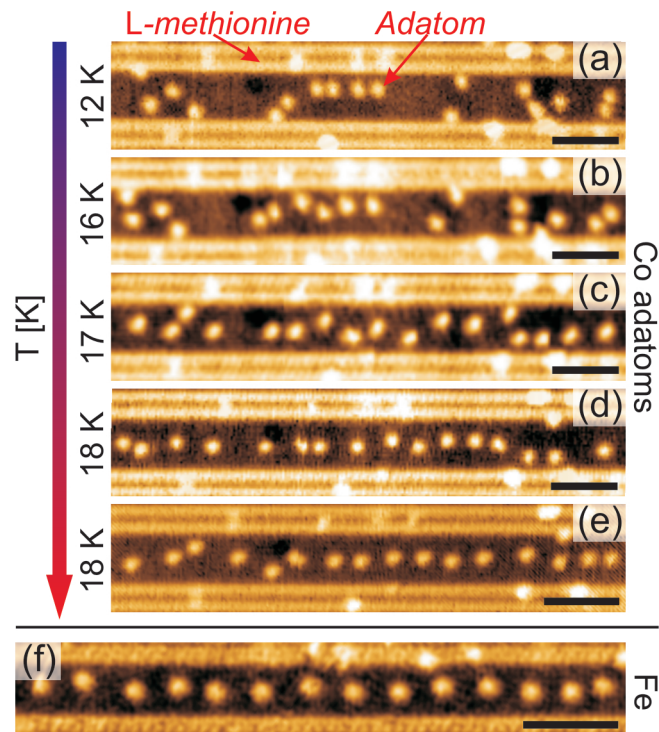


Figure 5.2: Adatom 1D self-alignment in between methionine biomolecular chains. (a)-(e) Randomly distributed Co adatoms at 12 K in the bare Ag(111) trenches self-align into regular chains after annealing to 18 K. The bare substrate trench is 35 Å wide i.e. confinement length of ~ 55 Å ($I = 0.06$ nA, $U = -400$ mV). (f) Fe adatom row in a biomolecular nanograting with interchain distance of 25 Å i.e. confinement length of ~ 45 Å. Image acquired at 12 K, after annealing to 18 K ($I = 0.06$ nA, $U = -1770$ mV). Scale bars: 50 Å.

The entropic pressure against which the self-aligning process competes has to become compensated by a gain in energy resulting from the interaction between the components of the system i.e. the biomolecular assemblies and the metal adatoms.

5.3.2 Dynamics and statistics of the self-alignment process

The dynamics of the Co self-alignment in between methionine chains was followed at the single atom level and compared with the diffusion of isolated Co on a bare Ag(111) surface. For this purpose, we took into account the diffusion of 200 Co adatoms in biomolecular trenches of 25 to 35 Å width. Their hopping rate was determined from STM data for temperatures between 15 and 18 K. The potential interference of the tunneling parameters was carefully considered, the outcome being that, in the range of $0.05 \leq I_t \leq 1$ nA and $50 \leq |U_{bias}| \leq 1000$ mV where the experiments were considered, the experimental method does not perturb the intrinsic dynamics of the system. The measurements corresponding to the adatoms in between the biomolecular trenches were carried out with the tunneling parameters $I_t=0.06$ nA and $U_{bias}=-400$ mV, whereas for the bare Ag(111) the parameters $I_t=0.1$ nA and $U_{bias}=-80$ mV were taken. For isolated atoms and specific site adsorption (as observed experimentally), the adatom hopping rate Γ at a temperature T is given by:

$$\Gamma(T) = -\frac{1}{\Delta t} \ln (P(\Delta t)) \quad (5.1)$$

Here $P(\Delta t)$ is the probability that an adatom remains immobile after

a delay time Δt [65]. $P(\Delta t)$ was evaluated experimentally by continuous sequences of STM images for the adatoms in between methionine trenches at the temperatures of 15 and 16 K, where single hopping events could be tracked from image to image. For the temperatures of 17.2 K and 18 K, the scanning speed of our setup could not follow single events and the more general definition of Γ for an isolated adsorbate had to be considered:

$$\langle \|\Delta\vec{r}(\Delta t)\|^2 \rangle = \Gamma \langle \lambda \rangle^2 \Delta t \quad (5.2)$$

$\langle \lambda \rangle$ being the average hopping length and $\langle \|\Delta\vec{r}(\Delta t)\|^2 \rangle$ the average square displacement of an adatom after time Δt . Assuming single hopping events, $\langle \lambda \rangle$ is equal to the atomic lattice constant, and Γ can be evaluated by measuring $\langle \|\Delta\vec{r}(\Delta t)\|^2 \rangle$ through STM image sequences. This method is also used to determine Γ on the bare Ag(111) substrate. The use of this definition for Γ implicitly includes the hypothesis that the atomic mobility in the trenches follows an unrestricted random walk. This can seem abusive, but the approach is on the one hand necessary in order to compare the confined and free cases. On the other hand, care was taken to select data sets of adatoms near the center with displacements much smaller than the width of the silver trench. Because the energy landscape is rather flat there, a quantitative measure of the mobility is obtained (*vide infra*).

The experimental values of Γ in relation to T are plotted in Fig. 5.3. It is obvious that for the entire investigated temperature range the hopping rates of the Co between the rows are decreased by more than an order of magnitude compared to that of isolated adatoms. The motion of Co on the bare substrate can be described by transition state theory (TST) [65], which

states that the adsorbate diffusion is mediated by the substrate heat bath and that Γ follows an Arrhenius behavior: $\Gamma(T) = \Gamma_0 \exp(-E_m/k_B T)$, where E_m is the migration barrier and Γ_0 the prefactor. The experimental data yields for the bare case the values of $\Gamma_0 = 2.7 \times 10^{-10} \text{ s}^{-1}$ and $E_m = 40.0 \text{ meV}$. It is important to note that here $E_m \ll k_B T$ in our temperature range, which is a necessary condition to model the adsorbate diffusion behavior with TST. A similar fitting procedure for the Co diffusion in the biomolecular trenches yields the values of $\Gamma_0 = 6.7 \times 10^{-10} \text{ s}^{-1}$ and $E_m = 44.6 \text{ meV}$. The increased value of E_m with respect to the uncorrelated bare Ag(111) case reveals the decreased atomic mobility at every considered temperature due to the electron confinement and the resulting indirect substrate-mediated interactions.

The Co atomic self-alignment is quantitatively summarized in Fig. 5.4. Here, we tracked the movement of 11 Co adatoms at 18 K in a 35 Å wide trench, i.e., with an electronic confinement length of $\sim 55 \text{ Å}$. The experimental data allowed us to evaluate the probability densities $p(r_{r-a})$ and $p(r_{a-a})$ of finding respectively an adatom within the distance interval $[r_{r-a}, r_{r-a} + dr_{r-a}]$ from the center of a methionine double row (Fig. 5.4(b)), and of finding a nearest-neighbor within the distance interval $[r_{a-a}, r_{a-a} + dr_{a-a}]$ (Fig. 5.4(c)). In a random configuration, the probability density of finding an adatom in a trench of width w at a distance r_{r-a} is equiprobable and is given by $1/w$. Figure 5.4(b) depicts the non-randomness of the adatom distribution and of the 1D self-alignment: the adatoms strongly prefer the center of the trench and strictly avoid the molecular boundaries. This provides direct evidence of a repulsive interaction between adatoms and molecular walls.

Now, considering the adatom distribution in the direction along the rows, the random probability of finding a nearest-neighbor adatom at a distance r_{a-a} is given by:

$$p_{ran}^{1D}(r_{a-a}) = \frac{2n}{L} \times \left(1 - \frac{2r_{a-a}}{L}\right)^{n-1} \quad (5.3)$$

The first term represents the probability of finding an adatom in the distance interval $[r_{a-a}, r_{a-a} + dr_{a-a}]$, the second term the probability of not

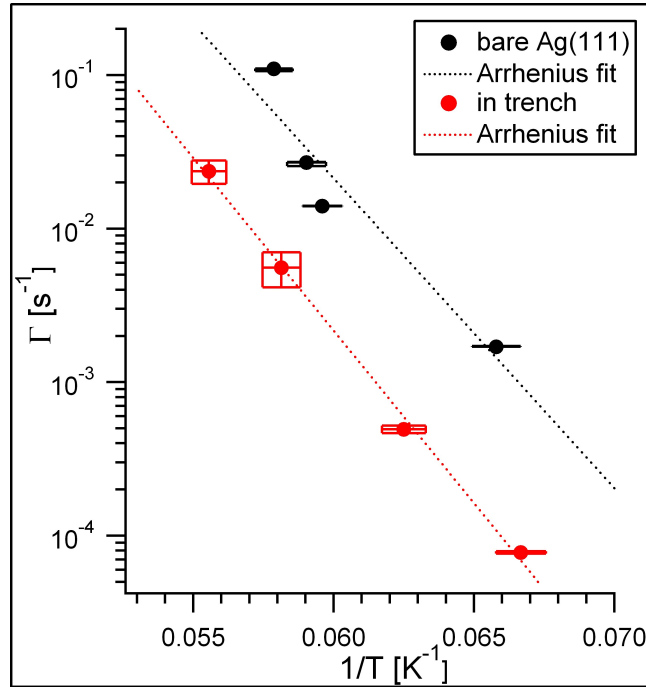


Figure 5.3: Temperature dependence of Co adatom hopping rates. Compared to isolated atoms on bare Ag(111) (black symbols), the mobility of Co confined in between methionine biomolecular trenches of widths 25 to 35 Å (red symbols) is markedly reduced. Arrhenius fit parameters: bare substrate ($\Gamma_0 = 2.7 \times 10^{10} \text{ s}^{-1}$ and $E_m = 40 \text{ meV}$), biomolecular trenches ($\Gamma_0 = 6.7 \times 10^{10} \text{ s}^{-1}$ and $E_m = 45 \text{ meV}$).

finding an adatom at a distance smaller than r_{a-a} , n the total number of adatoms, and L the trench length. The experimental probability density in

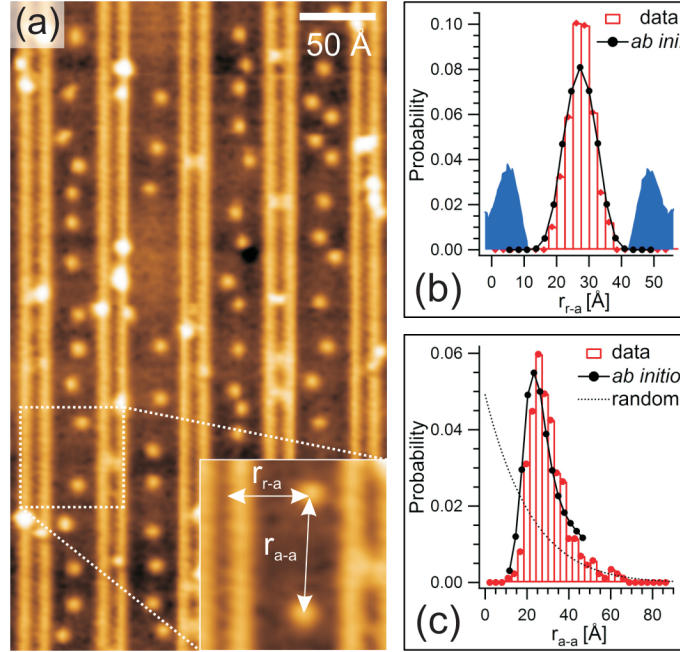


Figure 5.4: Statistics of adatom-chain and nearest-neighbor adatom-adatom distances in 35 Å wide methionine trenches. (a) STM topographical image of Co adatoms in between biomolecular trenches separated of 35 Å (confinement length of ~ 55 Å) at 18 K: r_{r-a} represents the adatom distance to the centre of the amino acid row, r_{a-a} is the adatom-adatom nearest-neighbor distance ($I=0.06$ nA, $U=-400$ mV). (b) Experimental probability density of adatom-row distances r_{r-a} (in red). The Boltzmann theoretical probability density (in solid black) given by *ab initio* calculations matches the experimental data. The blue curve represents the height profile of the methionine rows. (c) Experimental probability density of adatom-adatom nearest-neighbor distances r_{a-a} (in red). The distribution indicates a non-random positioning of the adatoms in the trenches and can be fitted with a Boltzmann probability density derived with the results from *ab initio* calculations (black dots).

Fig. 5.4(c) is a direct indication of the non-random 1D adatom distribution along the chains. Here, the most probable nearest-neighbor distance is 25.4 Å. A similar statistical study was performed for the Fe case, given a most probable nearest-neighbor distance of 23 Å.

5.3.3 Influence of the substrate electronic properties on the adatom self-ordering phenomenon

The principal suspect which may mediate the interaction enabling this self-ordering process is the electronic surface state band of the Ag(111) substrate, as previously demonstrated for atomic superlattices [125, 167, 168]. Figure 5.5 illustrates a low density Co deposition onto the methionine/Ag(111) system, where three Co adatoms (labeled 1 to 3) are positioned in a 35 Å wide trench (Fig. 5.5(b)). The STS dI/dV landscapes in Fig. 5.5(c) to 5.5(e) are a direct measurement of the local density of states and show how the interchain adatoms scatter and confine the Ag(111) surface electrons in the trench: Co atoms 2 and 3 represent electronic scattering potentials and define box-like border conditions for the surface electron eigenstates, which implies constructive electronic interferences (and thus electronic resonant states) only for specific energies. For instance, the spectroscopic maps of Fig. 5.5(c) to 5.5(e), with bias voltages -59 mV, -39 mV and -9 mV respectively, visualize the electron density of states close the first, second and third resonant modes of the surface electrons in the box defined by the Co adatoms and the confining methionine chains. Figure 5.5(f) plots the apparent topographic (A) and spectroscopic profiles (B, C, D) along the trench and emphasizes the different surface electron modes.

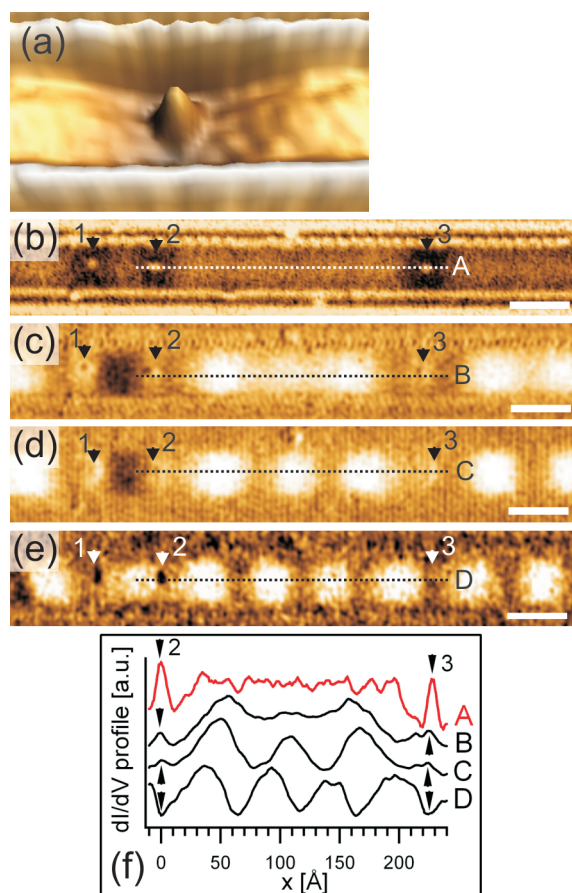


Figure 5.5: Confinement of surface electrons in a methionine supramolecular nanostructures with Co adatoms: mediation of the repulsive interaction. (a) 3D representation of a single Co adatom on Ag(111) in between two methionine chains ($I=0.1$ nA, $U=-20$ mV). (b) STM topographical image of three Co adatoms in between methionine rows separated of 35 Å ($I=0.06$ nA, $U=-80$ mV). (c)-(e) dI/dV maps of the same location at $U=-59$ mV, $U=-39$ mV, and $U=-9$ mV respectively ($I=0.06$ nA). Data acquired at 12 K, after annealing sample to 16 K. Scale bars: 50 Å. (f) Intensity profiles of the constant-current STM topographic data (red) and of the STS first derivative maps along lines A, B, C and D. Different resonant modes appear at the selected bias voltages.

To probe the hypothesis according to which the self-alignment is driven by the substrate electronic configuration, the row-adatom and adatom-adatom interaction energies were assessed theoretically using the Korringa-Kohn-Rostocker (KKR) Green's function formalism [160, 167, 170, 171, 173]. The results are summarized in Fig. 5.6. The calculations are performed for both Co and Fe adatoms, and the system is modeled by positioning a metal adatom in the middle of a Ag(111) trench with a confinement length of 50 Å (simulating a biomolecular trench of width 30 Å). The methionine chains and the Ag(111) step edges having similar electronic scattering properties [123, 163], the biomolecular rows are actually modeled by two Ag step edges. Figure 5.6(a) represents the surface electron mediated interaction energy between the adatom and the rows. The results for Fe and Co are identical, and the energy minimum at the center of the trench steers the adatom 1D self-ordering. The theoretical adatom-adatom interaction which is mediated by the substrate is similar to that of adatom pairs on a pure Ag(111) surface. This interaction potential is plotted in Fig. 5.6(b). Finally, Fig. 5.6(c) represents the 2D energy landscape showing both the adatom-row and adatom-adatom interaction. The interatomic interaction is similar for Fe and Co, with an energy minimum positioned at a nearest-neighbor distance slightly smaller for Fe, due to different electron scattering properties of the respective adatoms.

The theoretical results were compared to the experimental data by defining theoretical probability densities for $p(r_{r-a})$ and $p(r_{a-a})$ in the case of the Co adatoms, that are expressed assuming a Boltzmann equilibrium distribution as follows:

$$p(r_{r-a}) = \frac{1}{Z} \exp\left(\frac{-E_{r-a}(r_{r-a})}{k_B T}\right) \quad (5.4)$$

and

$$p(r_{a-a}) = \frac{1}{Z} p_{ran}^{1D}(r_{a-a}) \exp\left(\frac{-E_{a-a}(r_{a-a})}{k_B T}\right) \quad (5.5)$$

$p_{ran}^{1D}(r_{a-a})$ being the random 1D distribution defined in equation (5.3) and Z the partition function guaranteeing a properly normalized distribution.

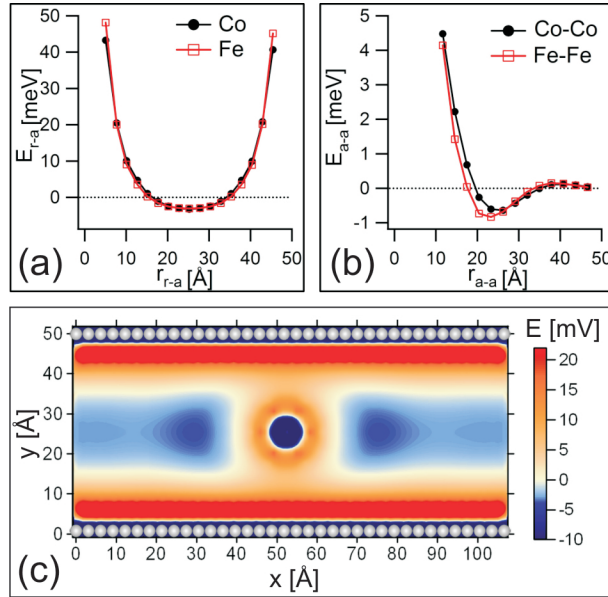


Figure 5.6: KKR Green's function calculations of the interaction energy between Fe and Co adatoms and a quantum resonator with 50 Å confinement length. (a) Plot of the energy landscape perpendicular to the resonator walls. (b) Adatom-adatom interaction potential along the symmetry axis of a resonator revealing preferential spacings of ~ 26 Å for Co and ~ 23 Å for Fe, respectively. (c) 2D interaction energy map for a Co adatom approaching the Co adatom positioned in the middle of the quantum resonators.

These theoretical expressions are plotted in Fig. 5.4(b) and 5.4(c), where they are compared with the experimental statistics taken at 18 K. The confinement length taken in the theoretical approach being of 50 Å and the one in the experiments of 55 Å, the abscissa of the theoretical distribution was rescaled by a factor of 1.1 for the $p(r_{r-a})$ case. The agreement between theory and experiment is remarkable, for both the cases of $p(r_{r-a})$ and $p(r_{a-a})$, showing the irrefutable role of the surface electrons in the adatom 1D arrangement. In the case of the nearest-neighbor distance probability, the theoretical most probable value for r_{a-a} is 23.3 Å, whereas the experiment showed 25.4 Å. This small difference can be due to the fact that the system is not completely equilibrated, corresponding to a thermal expansion of the spatial distribution. All in all, the agreement between theory and experiment is very satisfactory, confirming that the atomic 1D self-alignment is driven by electronic substrate mediated interactions.

5.4 Conclusion

Our study demonstrates a novel bottom-up approach for the organization of one-dimensional Co and Fe strings by using the inherent self-assembly capability of methionine biomolecular nanotemplates on a noble metal substrate. The dynamics and equilibrium statistics of this 1D self-alignment process have been determined, confirming that the surface state electrons are the vehicle driving such phenomena. This is a successful illustration of how the spatial arrangement of single atoms can be steered by the combination of self-assembled functional biomolecular species and the long-range electronic interactions mediated by a nanostructured template. It is suggested that this

methodology can be generally employed for nanoscale control of matter and the positioning of single atomic or molecular species in surface-supported supramolecular architectures.

At the moment of the submission of this thesis, the results exposed in this Chapter were submitted to a peer-reviewed journal. The respective experiments were performed at the Advanced Materials and Process Engineering Laboratory (AMPEL) at the University of British Columbia in collaboration with Dr. J. Reichert, Dr. W. Auwärter, G. Jahnz, Dr. Y. Pennek, Dr. A. Weber-Bargioni and Dr. J.V. Barth. The theoretical *ab initio* calculations were performed in collaboration with Dr. V.S. Stepanyuk, Dr. L. Niebergall and Dr. P. Bruno from the Max Planck Institute for Microstructure Physics in Halle, Germany.

Chapter 6

Self-assembly of *L*-methionine on Cu(111): steering enantiomorphous biomolecular nanostructures by substrate reactivity and thermal activation

The self-assembly of the amino acid *L*-methionine on Cu(111) was investigated in ultrahigh vacuum (UHV) conditions by means of scanning tunneling microscopy (STM), helium atom scattering (HAS) and x-ray photoelectron spectroscopy (XPS). The system is strongly influenced by the substrate reactivity and temperature during molecular deposition. The STM and HAS structural analysis yields that, for temperatures below 273 K, the biomolecules assemble in anisotropic extended clusters oriented with a -10° rotation off the $\langle 110 \rangle$ crystalline orientations of the substrate. For temperatures above 283 K, a regular and ordered one dimensional phase arises with a $+10^\circ$ rotation with respect to the high-symmetry substrate orientations. High resolution STM data of this ordered 1D arrangement evidences molecular dimerization and second-order commensurability with the underlying atomic lattice in the chain direction. XPS measurements reveal that the

high temperature ordered phase consists in an exclusively anionic ensemble with a deprotonated carboxylic group and a neutral amino group, while the low temperature case is heterogeneously composed of both zwitterionic and anionic species, depending on whether the molecules are immobilized on the free terraces or at the low-coordinated adsorption sites of the substrate step-edges. These combined results evidence a structural transformation of the supramolecular assembly which is triggered by a thermally activated chemical process and which carries the intrinsic chiral signature of the adsorbed molecular units.

6.1 Introduction

As investigated in the previous Chapters, molecular self-assembly on surfaces comprises promising potential for the prospective design of functional architectures at the nanoscale [15, 98]. Notably, the group of biologically relevant species such as amino acids or nucleic acids possess inherent molecular recognition and functional self-organization properties which directly promote them as potential building units for the noncovalent synthesis of two-dimensional nanostructures [72–74, 108]. In general, the state of stable configurations at thermodynamic equilibrium is not only defined by the properties of the molecular entities, but also by the influence of the chemical and structural characteristics of the underlying support. Consequently, the same adsorbed molecules can behave and relax dramatically different depending on the nature of the substrate-molecule interactions [176, 177]. In the case of chiral species particularly, it occurs that the punctual chiral signature of the adsorbate can be translated into a mesoscopic enantiomorphism of the

two-dimensional supramolecular self-assembly [73, 74, 178]. This process is ensured by the molecular-recognition capabilities of the molecular units, but the final state of the relaxed adsorbate-substrate system is defined by the global thermodynamic conditions, and, for instance, thermally activated chiral switching phenomena has been already observed on surfaces [138].

In this Chapter we report a low-temperature scanning tunneling microscopy (LT-STM) study on the self-assembly of the amino acid *L*-methionine on Cu(111) under ultra-high vacuum (UHV) conditions. Methionine provides functionalities which are both relevant for zwitterionic self-assembly and for metal binding sites in peptide chains. The previous Chapters revealed that on Ag(111) the amino acid dimerizes and self-assembles in extended one-dimensional nanostructures running parallel to the close-packed crystallographic orientations of the underlying atomic lattice (Fig. 6.1(a)). These commensurate chains arranged mesoscopically into regular biomolecular gratings whose mesoscopic ordering can be tuned by the molecular coverage, as confirmed by STM and complementary helium atomic scattering (HAS) observations. By contrast, on Cu(111) the molecular ordering is strongly influenced by the higher reactivity and the smaller lattice constant ($a_{Cu(111)} = 2.55 \text{ \AA}$) of the substrate. At low temperatures ($< 273 \text{ K}$), disordered molecular clusters evolve for submonolayer coverages, whereas the saturated monolayer exhibits partial ordering arising from the influence of the substrate, with linear structures growing with a -10° shift with respect to the $\langle 110 \rangle$ crystalline orientations (Fig. 6.1(b)). On the other hand, following deposition on the substrate held at temperatures above 283 K, a regular one dimensional phase arises with a $+10^\circ$ rotation with respect to the $\langle 110 \rangle$

orientations (Fig. 6.1(c)) coexisting with patches of the disordered phase. Molecular resolution measurements of the ordered 1D arrangements indicate dimerization and a second-order commensurability with the atomic lattice of the substrate along the chain direction. These results are confirmed by HAS observations. In combination with the STM data, x-ray photoelectron spectroscopy (XPS) experiments show that the high temperature ordered phase comprises the molecules in their anionic state, with a deprotonated carboxylic group and a neutral amino group. In contrast, the low temperature disordered phase reflects an heterogeneous zwitterionic and anionic self-assembly, the anionic deprotonated state apparently being linked to the metal-ligand binding of the amino acid molecules with the more reactive, less coordinated copper atoms at the step-edges. It is concluded that the structural transformation which the supramolecular assembly undergoes from low to high temperature is triggered by a thermally activated chemical process, this transformation carrying the intrinsic chiral signature of the adsorbed molecular units.

6.2 Experimental section

The morphological and structural properties of the system were studied by means of real space STM data, supported by the HAS diffraction information. XPS provided the spectroscopic elements for the chemical resolution of the biomolecular self-assembly. The STM experiments were performed at a base pressure 2×10^{-10} mbar in a custom-designed ultra-high vacuum (UHV) system comprising a commercial Besocke-type LT-STM [84] and standard tools for *in situ* sample preparation and characterization. The chemomechanically

polished Cu(111) sample was prepared *in situ* by cycles of Ar⁺ sputtering at an energy of ~ 0.8 keV and currents of typically 4 μA , followed by an annealing procedure at a temperature of 770 K. The *L*-methionine amino acid ($\geq 99.5\%$, Sigma-Aldrich) was deposited by thermal evaporation at a temperature of approximately 370 K and with a deposition rate Γ in the order of 1 ML/min. The morphology and chemical state of the molecular self-assembly was studied in dependence of the substrate temperature during the deposition, which varied between 240 and 320 K. Following the preparation, the sample was cooled down to temperatures below 15 K for the acquisition of the STM topographic data. The constant-current images were obtained with an electrochemically etched W and with the bias voltage applied to the sample.

XPS and HAS experiments were carried out to provide chemical insight and supplementary morphological diffraction information on the biomolecular self-assembly. These measurements were performed at the ALOISA beamline (ELETTRA), whereby deposition of the *L*-methionine amino acid on Cu(111) was performed under the same UHV conditions as for the STM experiments. The HAS diffraction patterns were obtained with an incident He beam of energy 19 meV and wavevector 6.3 \AA^{-1} . The XPS spectra were obtained with the sample cooled down to 193 K after preparation in order to minimize the radiation damage [89]. The overall binding energy resolution is 300 meV with a photon energy of 596.7 eV [44]. The binding energy on the shown spectra is given relative to the substrate Fermi level. The XPS raw data was treated by subtracting the background signal due to inelastically scattered photoelectrons and fitting with Voigt functions.

6.3 Results and discussion

6.3.1 Thermally activated enantiomorphic orientational switch

Our previous study of *L*-methionine deposited on Ag(111) showed that the amino acid adsorbed in its zwitterionic chemical state, forming regular one dimensional nanogratings with tunable periodicity (Fig. 6.1(a)). On Cu(111), the picture is slightly different due to the higher reactivity and different lattice periodicity of this surface. Depending on the substrate temperature during the molecular deposition, methionine assembles into two distinct supramolecular structures α and β . At 240K, the molecules nucleate into small stick-like clusters showing partial linear ordering (Fig. 6.1(b)), this pattern being defined as the structure α . These formations grow following a 10° clockwise tilt with respect to the high-symmetry axis of the underlying lattice. At higher substrate temperatures during deposition, an additional self-assembly pattern β arises. One-dimensional arrays with long-range order emerge along an orientation shifted off 10° counter-clockwise relative to the high-symmetry axis of the substrate (Fig. 6.1(c)). Both phases coexist in a given temperature range, indicating a non trivial transition process between both entities. However, the ratio between the two phases is highly temperature dependent: at a higher temperature, the well-ordered linear pattern prevails (Fig. 6.1(d)).

The low-temperature STM data were supported by complementary XPS and HAS experiments in order to, respectively, resolve the chemical state of the adsorbed molecules and provide confirming diffraction elements on the growth orientations and periodicities of the biomolecular formations. As for

the STM data, the dependence of the system on the temperature during preparation was considered. The HAS 2D diffraction maps comprise orientational information on the supramolecular real space geometries on the surface. At temperatures below 280 K, an hexagonal diffraction pattern with diffuse features and rotated 10° clockwise with respect to the high-symmetry directions of the Cu(111) substrate, indicates a partially ordered surface mor-

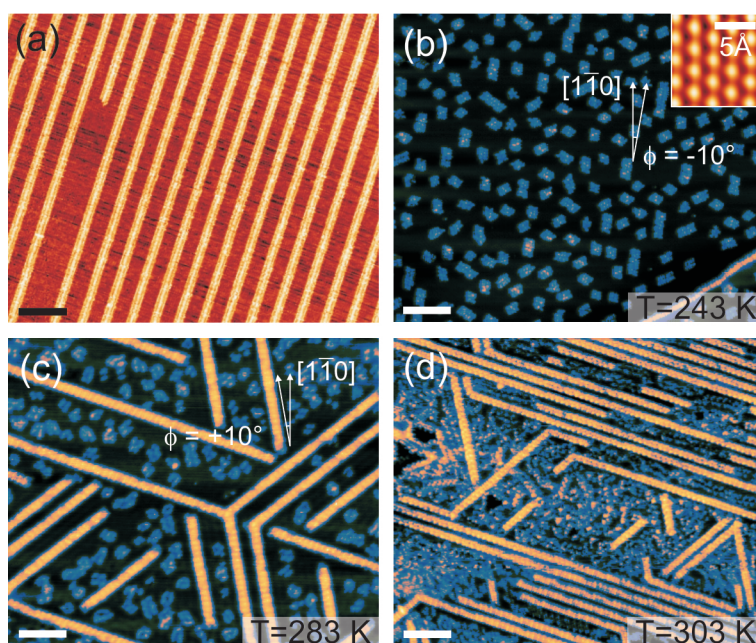


Figure 6.1: STM images of the self-assembly of the *L*-methionine amino acid on Ag(111) and Cu(111). (a) Regular and tunable 1D biomolecular nanogratings on Ag(111) ($I=0.1$ nA, $U=-500$ mV, $\theta=0.38$ ML). Scale bar: 200 Å. (b) *L*-methionine deposited on Cu(111) at $T=240$ K ($I=0.1$ nA, $U=-100$ mV, $\theta = 0.25 \pm 0.05$ ML). Scale bar: 100 Å. Inset: atomic resolution of the Cu(111) substrate. (c) Deposition on Cu(111) at $T=280$ K: 1D ordered phase emerges ($I=0.1$ nA, $U=-100$ mV, $\theta = 0.42 \pm 0.05$ ML). Scale bar: 100 Å. (d) Deposition at $T=300$ K ($I=0.06$ nA, $U=-100$ mV, $\theta = 0.90 \pm 0.05$ ML) showing small domains of a nanograting. Scale bar: 100 Å.

phology which we associate with the phase α (Fig. 6.2(b)). With increasing sample temperatures, the diffraction features become better defined, which is visualized in Fig. 6.2(c) through the diffraction intensity profiles showing the arising of pronounced satellite maxima at $\|\Delta\vec{k}\| = 0.20 \pm 0.03 \text{ \AA}^{-1}$, corresponding to a $31 \pm 4 \text{ \AA}$ periodicity perpendicular to the chain direction. This is accompanied by a 20° counter-clockwise rotation of the diffraction hexagon (Fig. 6.2(a)), and can be assigned to the well-ordered phase β observed in the STM topographic images. For this highly ordered phase, the STM real-space data reveal a regular spacing between the linear biomolecular nanowires, which corroborates the appearance of the sharp satellite peaks on the HAS patterns. The interchain periodicity of these regular arrangements indicated by STM is similar in magnitude to the 31 \AA HAS periodicity, but varies with molecular coverage, the periodicity for the saturated monolayer β -patches being of $25 \pm 2 \text{ \AA}$. Therefore, a direct correlation between the HAS diffraction $\|\Delta\vec{k}\|$ values and the real-space periodicities is not possible.

This thermally activated orientational switch represents an enantiomorphic reordering of the system, and must be related to the chiral signature of the molecular building units. Such transfer of the molecular chiral 'footprint' into a mesoscopic supramolecular chirality has already been observed in previous studies of adsorbed amino acids on metal surfaces [179, 180], depicting a supplementary degree of morphological control on low-dimensional self-assembled nanostructures.

6.3.2 Correlation with a catalytically induced heterogeneous ammonium deprotonation

Whereas the HAS data confirms the STM orientational and morphological observations, the XPS data allows resolving the chemical state of the ad-

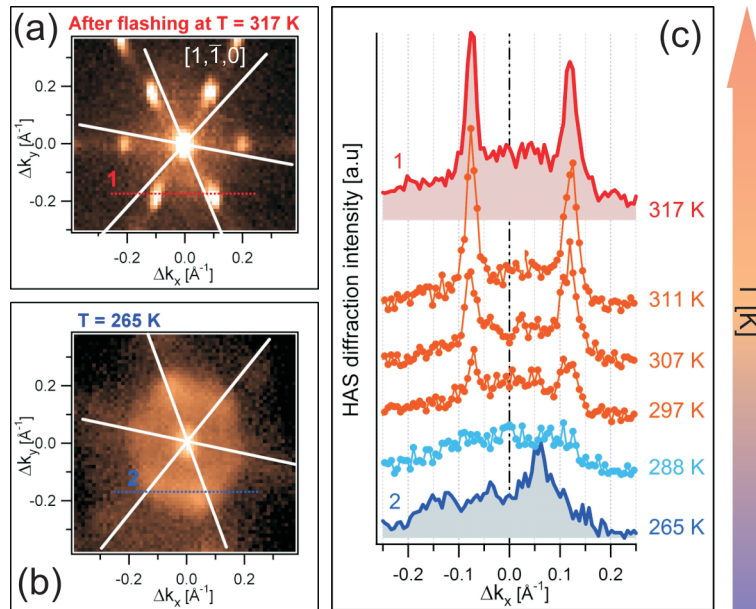


Figure 6.2: HAS data of the *L*-methionine/Cu(111) system. (a) Two-dimensional HAS diffraction map of the *L*-methionine/Cu(111) system after flashing to $T=317$ K: we observe an hexagonal pattern with pronounced satellite maxima and with a 10° counter-clockwise tilt relative to the $\langle 110 \rangle$ orientations of the substrate, which we associate with the supramolecular phase β . (b) HAS diffraction map of the sample preparation at 265 K: hexagonal pattern with diffuse features and a 10° clockwise tilt with respect to the $\langle 110 \rangle$ orientations. This case is related to supramolecular phase α . (c) HAS intensity profiles along $\Delta k_y = -0.20 \text{ \AA}^{-1}$ for substrate temperatures from 265 K to 317 K: pronounced satellite maxima appear for temperatures above 288 K. These satellite peaks correspond to real-space periodicities of $31 \pm 3 \text{ \AA}$.

sorbed molecules. The N 1s XPS spectra in Fig. 6.3 were obtained for a full monolayer coverage. Spectra for the C 1s, S 2p and O 1s core electrons were also measured, showing no dependence on the sample temperature during deposition. The O 1s signature reveals a single peak at a binding energy of $E_{O1s} = 531.55 \pm 0.07$ eV, which corresponds to the deprotonated resonating oxygen atoms of the amino acid carboxylate group, similar to what was found for the carboxylate group in the *L*-methionine/Ag(111) system. The case of the N 1s analysis is more complex and the related spectra are shown in Fig. 6.3. For a substrate temperature of 265 K during deposition (blue curve), we find two distinct peaks: one at a binding energy of $E_{N1s}^{(1)} = 399.54 \pm 0.18$ eV, another one at $E_{N1s}^{(2)} = 401.30 \pm 0.12$ eV. After heating to 317 K, only the $E_{N1s}^{(1)}$ peak at 399.54 eV remains with an increased amplitude (red curve). This thermally induced transition is a signature of a chemical reaction occurring in the nitrogen group. By comparing with XPS experiments performed on the *L*-cysteine/Au(110) system [128], we deduce that $E_{N1s}^{(1)}$ corresponds to the amino group NH_2 whereas $E_{N1s}^{(2)}$ can be assigned to the ammonium group NH_3^+ . The presence of both peaks for the low temperature preparation is an intrinsic property of the system and it is not due to a beam induced artifact. This point was studied in detail with specific time-dependent XPS experiments focusing on the N 1s peak for the low temperature case, the outcome being that the N 1s⁽¹⁾ and N 1s⁽²⁾ are stable to beam exposure. Taking into account that the O 1s spectrum represents the chemical trace of the carboxylate group, we conclude that the low temperature phase α consists in a mix of zwitterionic and anionic assembly, whereas the high temperature phase is composed of purely anionic species

of the amino acid. Along with the STM data, the HAS and XPS measurements confirm that the phase transition consists in a continuous chemical process within a temperature window between ~ 280 and ~ 290 K, where the ammonium group NH_3^+ of the zwitterionic portion deprotonates. This anionic chemical state with a neutral amino group and a negatively charged carboxylate group for temperatures above 290 K is identical to the chemical configuration of other amino acids such as alanine and glycine adsorbed on low-index Cu surfaces at room temperature [181–184].

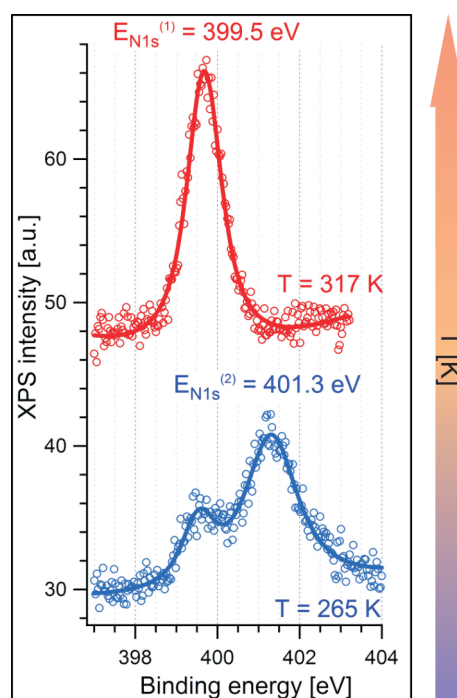


Figure 6.3: N 1s XPS spectra of *L*-methionine on Cu(111) for the low (blue) and high (red) temperature phases: the phase transition from α to β is associated to the deprotonation of the ammonium group.

The fact that the high temperature phase is composed exclusively of an-

ionic species is irrefutably demonstrated by the XPS experiments. However, the ambivalent chemical composition of the low temperature is more intricate. Figures 6.4(a) and 6.4(b) focus on the XPS N 1s peaks for the low temperature phase. The inset in Fig. 6.4(a) represents the ratio r between the areas of the Voigt curves fitting N 1s⁽²⁾ and N 1s⁽¹⁾ respectively, depending on the molecular coverage θ . The molecular coverage of the preparation was evaluated by measuring the HAS specular beam during molecular deposition. It becomes clear that there is an increasing trend of r with respect to θ , meaning that there is an increase of the zwitterionic species with coverage. Morphologically, it has been observed on the STM data that, the molecules having enough thermal energy to diffuse at the deposition temperature (for high as well as for the low temperature cases), the amino acid binds first to the substrate step-edges, where the Cu atoms are less coordinated and therefore their interaction with the biomolecules is stronger. Thus, one might think that the amino acid molecules bound to the substrate step edges are in their anionic form and are related to the N 1s⁽¹⁾ XPS peak. Once there are enough species to saturate the step edges, the zwitterionic cluster-like assembly emerges. The intensity of the N 1s⁽²⁾ XPS peak increases once the molecules have decorated the step edges. From this point of view, the low coordinated step-edge atoms play a catalytic role, inducing the deprotonation of the ammonium group. The STM image in Fig. 6.4(c) shows the decoration of the step edges by the biomolecules for the low temperature case, indicated by the white arrows. This hypothesis is corroborated in the N 1s XPS spectrum in Fig. 6.4(b), where a substrate with a higher density of step edges was considered for the low temperature molecule deposition.

This rougher surface was obtained by Ar⁺ sputtering at 0.3 keV after the usual cleaning procedure of the sample. Here, the N 1s⁽²⁾ peak related to the ammonium group is almost unnoticeable, whereas the amino group N 1s⁽¹⁾ peak at 399.5 eV is clearly predominant. When the system is heated above a critical temperature situated between 283 and 298 K, the deprotonation of the ammonium group becomes thermally activated and the XPS N 1s spectrum consists in the N 1s⁽¹⁾ peak exclusively, like in Fig. 6.3 (red curve). Only the anionic entities remain. This temperature dependence evidences a lower activation barrier for the catalytically induced ammonium deprotonation at the low-coordinated step-edges adsorption sites. The thermal excitation of the system not only yields a chemical process: in addition, the morphology of the substrate step edges is altered by the amino acid adsorption, becoming indented, as seen in Fig. 6.4(d). This adsorbate induced step-edge faceting phenomenon has been already observed for other amino acids adsorbed on Cu surfaces [185, 186], as well as for other functional molecular units on Ag surfaces [187]. Moreover, one can observe that the nucleation of the ordered 1D assembly at high temperature is linked to the perturbation of the step edges by the molecular adsorption and that this highly ordered phase is in fact an extension of the molecules decorating the step edges, giving supplementary evidence that these species are likely to be chemically identical.

6.3.3 Molecular arrangement in the ordered high temperature anionic phase

From the real space topographic perspective, the low temperature STM data allow resolving the molecular arrangement of both phases. Figure 6.5(a)

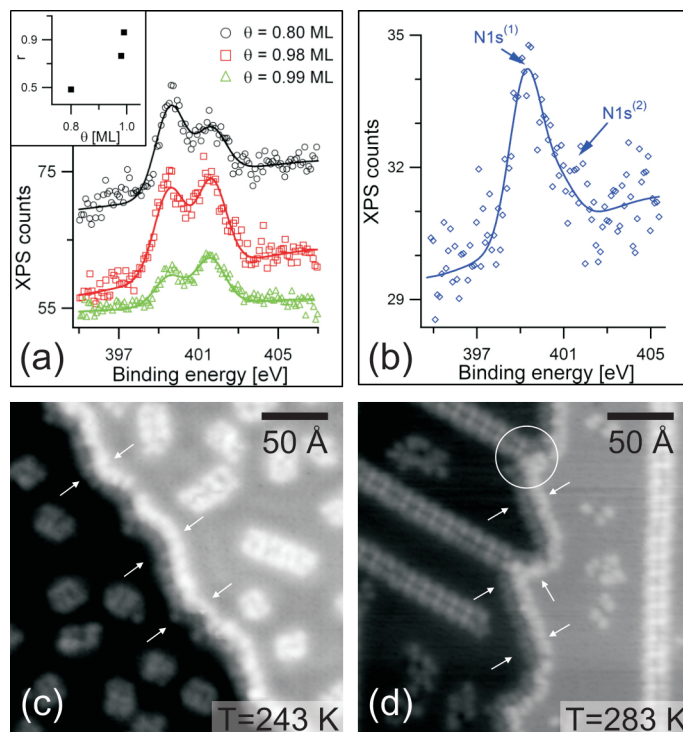


Figure 6.4: Dependence of the N 1s XPS spectra on the molecular coverage θ and on the low-coordinated nucleation site density for the low temperature phase. (a) Variation of the relative intensity of XPS peaks N 1s⁽¹⁾ and N 1s⁽²⁾ in dependence of θ for the low temperature phase: relative intensity of the N 1s⁽²⁾ peak increases with molecular coverage. Inset: ratio r between the area of the Voigt curves for peaks N 1s⁽²⁾ and N 1s⁽¹⁾ in dependence of θ . (b) N 1s XPS spectrum for a higher step-edge density: Voigt fit shows a relatively high N 1s⁽¹⁾ peak, revealing a high density of species bonded to the substrate step-edges. (c) STM topographical image ($I=0.1$ nA, $U=-200$ mV) of the low temperature phase prepared at 243 K shows the biomolecules bonded to the step-edges (white arrows) related to the N 1s⁽¹⁾ XPS peak. (d) STM topographical image ($I=0.1$ nA, $U=-500$ mV) of the high temperature phase prepared at 283 K: the step-edges are perturbed by the bonded molecular species (white arrows) and the nucleation of the ordered molecular phase is linked to the low coordinated adsorption sites (white circle).

shows details within the clusters composing phase α and reveal molecular dimerization. The XPS measurements having demonstrated that this phase corresponds to the self-assembly of the amino acid molecules in their zwitterionic state, we can assume that the intermolecular bonding scheme is similar to the one found in the *L*-methionine/Ag(111) system. The 10° clockwise rotation with respect the $\langle 110 \rangle$ orientations being necessary to match the energetically favorable adjacent intermolecular distance to the smaller lattice constant of the Cu(111) substrate. In contrast to the highly linear regularity of the gratings found on Ag(111), the zwitterionic assembly on Cu(111) shows only restrained one dimensional extensibility, which could be related to the reduced mobility and higher nucleation density of the adsorbate on Cu(111) due to the higher substrate reactivity. On the other hand, the anionic phase β (Fig. 6.5(b) and 6.5(c)) shows extended 1D order and a 10° counter-clockwise tilt relative to the $\langle 110 \rangle$ orientations of the substrate revealing a chiral switching process within the nanostructures. The rows in this phase are also composed of strings of dimers. It becomes clear in the high resolution STM images that the regularity in this dimer arrangement is significantly higher. Along the growth direction, a second order commensurability pattern becomes evident (Fig. 6.5(b)), evidenced by the height profile on Fig. 6.5(d) along line B. Adjacent dimers appear with an apparent height difference of $\sim 0.3 \text{ \AA}$, every second dimer showing the same features. This contrast pattern can be explained with an atomistic model of the molecule-substrate system (Fig. 6.5(c)). With the periodicity of 5.8 \AA given by the STM data, and the 10° tilt counter-clockwise to the high-symmetry axis of the substrate, every second dimer exhibits the same adsorption site. The in-row periodicity

is remarkably close to the one found in *L*-methionine/Ag(111) system, and hence the tilt can be an adjustment to match the smaller lattice constant of 2.55 Å of the Cu(111) surface. This adjustment within the molecular arrangement can be related to specific binding sites of the different amino acid functional groups with respect to the underlying atomic lattice. For instance, previous experimental [182, 183] and theoretical [188, 189] studies performed on the adsorption of alanine and glycine on copper surfaces revealed that the amino acids bind to the metal substrate through their amino and carboxylate groups, the nitrogen and oxygen atoms preferentially sitting on top sites of the Cu crystal. Our results could therefore hint a similar adsorption scenario. The molecular dimerization and the topographic characteristics of the self-assembly shown by the STM images suggest a hydrogen-bond driven head-to-head assemblage between two molecules along their main axis, where one of the negatively charged oxygen atoms of the carboxylate group faces an amino hydrogen atom. The linear growth can be explained by adjacent H-bonding involving again the carboxylate and amino groups. The proposed bonding scheme is related to the one for the *L*-methionine/Ag(111) system.

The high regularity of phase β allows us to examine its binding scheme in more detail. The XPS experiments having revealed that the species in this phase are anionic, a question remains concerning how an attractive interaction is possible between negatively charged entities. The polarizability of the metallic substrate plausibly enables the assembly process by screening the molecular negative charge through charge density redistribution. To reinforce the head-to-head dimerization and the adjacent H-bonding in our model of the molecular arrangement, molecular mechanics simulations were con-

ducted. We considered a system composed of two *L*-methionine molecules, whose interacting energy was determined using a MM+ [122] force field approach. To qualitatively include the screening effect of the substrate, image

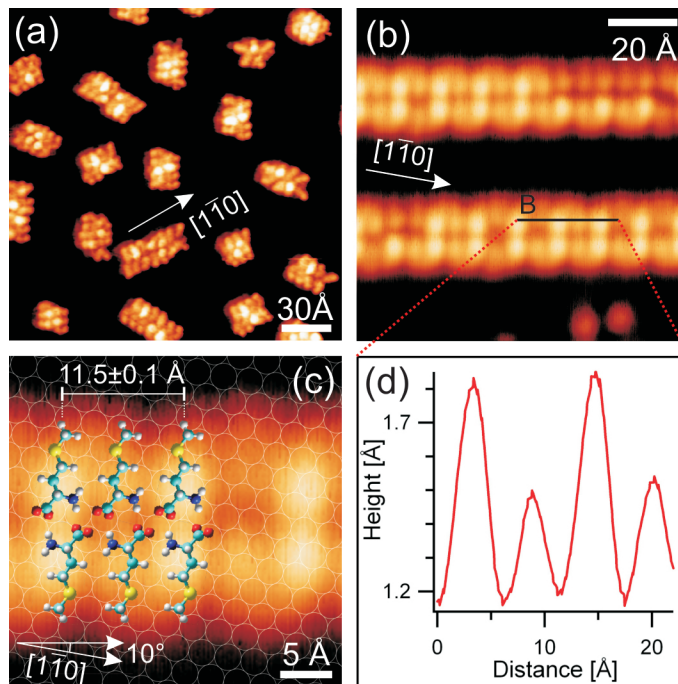


Figure 6.5: Molecular resolution STM data of phases α and β . (a) Molecular resolution of clusters in phase α : dimerization and partial directional growth is observed along directions tilted 10° clockwise of the substrate $\langle 110 \rangle$ orientations ($I=0.1$ nA, $U=-100$ mV). (b) Molecular resolution and Moiré pattern along the growth direction of the highly ordered phase β : every second molecule in this direction shows the same apparent height, revealing equivalent adsorption sites on the substrate ($I=0.1$ nA, $U=-600$ mV). (c) Molecular resolution and model of the molecular arrangement within the ordered phase β : the underlying atomic lattice is illustrated by the white circles. The biomolecular nanostructure is commensurate with the substrate atomic periodicity. ($I=0.1$ nA, $U=-600$ mV). (d) Apparent height profile along line A in (b) evidencing the second order Moiré pattern.

charges were included in our model by placing oppositely charged mirrored molecules below the surface plane of the Cu(111) (Fig. 6.6(a)). The presence of the image charges in this simplified model of the molecules-substrate system allows the appearance of an attractive inter-molecular interaction. This is depicted in Fig. 6.6(b) and 6.6(c), where we observe energy minima in the two-dimensional interacting energy landscape of the system. Figure 6.6(b) corresponds to the anti-parallel molecular configuration, indicating that head-to-head dimerization is energetically favorable. The calculation of the interaction energy landscape for the parallel configuration is illustrated in Fig. 6.6(c), suggesting bonding of adjacent dimers driving the linear extensibility of the nanostructures. This simplified image charge calculation endorses the proposed model of the molecular arrangement in phase β .

The results above present a scenario where the thermally activated ammonium deprotonation is the mediation for the orientational transformation between the low and high temperature cases. The low temperature preferential orientation of the supramolecular arrangement along a 10° clockwise tilt with respect to the high-symmetry axis represents already an adsorbate induced breakdown of the threefold symmetry imposed by the surface crystalline structure: the molecular adsorption removes from the system its mirror-symmetric properties. This symmetry breakdown has to carry the intrinsic chiral signature of the individual amino acid species, and although the low temperature case only shows partial ordering, the structure enantiomorphism exposes a preferential adsorption configuration. Work by Weigelt *et al.* showed how the enantiomorphic characteristics of two-dimensional supramolecular assemblies can be alternated through thermal

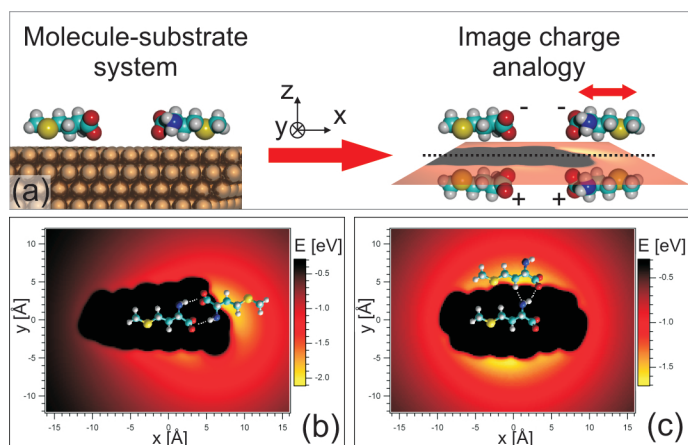


Figure 6.6: MM+ molecular mechanics calculations for the ordered anionically composed phase β . (a) The two-molecule *L*-methionine system adsorbed on Cu(111) is considered as a 4-molecule system: the two real *L*-methionine molecules interact with 2 virtual *D*-methionine molecules of opposite charge and placed symmetrically with respect to the plane defined by the substrate. (b) Two-dimensional interaction energy landscape of the molecular system in the antiparallel configuration: minimum energy position implies H-bonded head-to-head dimerization. (c) Interaction energy landscape in the parallel configuration: adjacent H-bonded network supports long-range 1D order.

activation [138]. Nevertheless, whereas in their case the chiral switching was due to thermally driven conformational changes of the molecular units, our system is characterized by an enantiomorphic change mediated by a thermally activated catalytic chemical reaction. The ammonium deprotonation reassigns a preferential adsorption configuration, and the chiral properties of the system are altered as a consequence. A key feature of this mechanism is its primary localization at the step-edges, demonstrating the heterogeneous catalytic properties of the surface due to its increased chemical reactivity at the low coordinated one-dimensional defects. This picture is in agreement

with previous work related to molecular dissociation and heterogeneous catalysis on surfaces [82].

6.4 Conclusion

In conclusion, the self-assembly of the *L*-methionine amino acid was entirely resolved, in terms of morphology through STM and HAS measurements, but also in terms of its chemistry through XPS experiments. The point of this study resides in the supplementary parameter of control on the biomolecular nanostructures: the thermal activation of the system triggers a chemical process which dramatically alters the final state of the self-assembly. Here, the thermally activated ammonium deprotonation catalytically induced by the Cu(111) substrate reactivity drives a morphological chiral switching process within the biomolecular ensemble and reveals an entirely new supramolecular configuration. The equilibrium outcome of the self-assembly process is not only dictated by the intrinsic properties of the adsorbed entities, but also the supporting substrate plays a key role in the process.

The experiments of this Chapter were performed at the Advanced Materials and Process Engineering Laboratory (AMPEL) at the University of British Columbia in collaboration with Dr. J. Reichert, Dr. Y. Pennec, Dr. W. Auwärter, Dr. A. Weber-Bargioni, M. Marschall, and Dr. J.V. Barth, and at the ALOISA beamline of the ELETTRA synchrotron light source in collaboration with Dr. D. Cvetko, Dr. A. Cossaro, Dr. G. Bavdek, M. Dell'Angela and Dr. A. Morgante.

Chapter 7

L-tyrosine on noble metal surfaces: comparison with the *L*-methionine bonding scheme

In this Chapter we present a combined study of the self-assembly of the *L*-tyrosine amino acid on the closed-packed noble metal surfaces Ag(111) and Cu(111) in ultrahigh vacuum (UHV) conditions by means of low-temperature scanning tunneling microscopy (LT-STM), x-ray photoelectron spectroscopy (XPS) and near-edge x-ray absorption fine structure (NEXAFS). Whereas on Cu(111) the adsorbed molecules show a strong interaction with the substrate and undergoes a catalytically induced dissociation, on Ag(111) the biomolecules self-assemble above a critical temperature into linear structures primarily following the substrate crystalline symmetry. Our high resolution topographical STM data reveal non-covalent molecular dimerization within the highly ordered one-dimensional nanostructures, which recalls the geometrical pattern already seen in the *L*-methionine/Ag(111) system and supports a universal self-assembling scheme for amino acids on the Ag(111) surface. The molecules desorb above 350 K, indicating a relative weak interaction between the molecules and the substrate. XPS measurements reveal a zwitterionic adsorption, whereas near-edge x-ray absorption fine structure (NEXAFS) experiments show a non-flat adsorption of the phenyl ring, making an

angle of $\sim 38^\circ \pm 9^\circ$ with respect to the substrate plane. This allows possible $\pi - \pi$ interactions between adjacent molecules within the supramolecular self-assembly.

7.1 Introduction

Biological order, life itself, is glued together as well as operated by supramolecular interactions. At the molecular scale, the behavior of such complex systems is driven by fundamental processes such as molecular self-assembly, self-recognition and geometry conformation [16, 19, 190, 191], to name a few. In these biomolecular systems, catalytically triggered chemical reactions [35] and induced conformational geometry changes of the supramolecular structures [138, 192–194] can occur, altering their functionality. A better understanding of such fundamental processes can bring insight in the characterization of more complex biological systems. On metal surfaces, the examination of biomolecular self-assemblies can lead to such elementary portrayal. Furthermore, the control of these assembly processes defines a promising approach for the design of unidimensional [107, 195] and bidimensional [166, 196] functional nanostructures by employing the inherent functionality and specific non-covalent bonding capacity of the molecular building units. The choice of a supporting substrate is also critical for the determination of the state for such nanostructures: the structural symmetry and chemical properties of the underlying lattice have dramatic effects on the conformational and chemical state of these systems [177]. This bioinspired procedure for nanostructuring and functionalization surfaces can emerge into a new paradigm of 'bottom-up' design to go beyond the limitations dictated by

'top-down' approaches.

Studying non-covalent intermolecular interactions on surfaces with interdisciplinary efforts has become a major field of research [15]. Scanning tunneling microscopy (STM) and spectroscopy (STS) represents a powerful analytical tool to locally describe the interactions between biomolecules in a perfectly controlled environment. By the means of this method, the self-assembly of amino acids and other organic molecules on metallic surfaces has been studied, along with the chemical and morphological effects on the system induced by the substrate properties [72, 73, 197].

In this Chapter we present a low-temperature scanning tunneling microscopy (LT-STM) study and characterization of the self-assembly of the *L*-tyrosine amino acid on the closed-packed noble metal surface Ag(111) and Cu(111) in ultrahigh vacuum (UHV) conditions. The interest in studying the behavior of single amino acids on metal surface resides in their inherent potentiality as functional building nano-units, but also in the fact that this approach might yield further fundamental insight in the role of specific amino acids composing more complex peptide chains with a given biological relevance. In the particular case of *L*-tyrosine, it is suspected to be involved in metal-ligand interactions which might alter the biological function of specific peptides [198]. Morphological studies of amino acid adsorption (*L*-tyrosine included) on metal surfaces have already been addressed in the past [72, 141, 199, 200], as well as their chemical considerations in solid-state thin films [128, 135, 201–204]. An interesting example of amino acid self-assembly on a metal surface is the submonolayer adsorption of *L*-methionine on Ag(111) which has been considered in the previous Chapters. This sys-

tem is characterized by regular nanogratings composed of linear biomolecular nanowires which consist in hydrogen-bonded zwitterionic dimers. Therefore, by considering the case of *L*-tyrosine on Ag(111), the influence of the amino acid side chain on the equilibrium configuration of the supramolecular assembly can be addressed. A combined morphological and chemical study of the case of *L*-tyrosine on the weakly reacting Ag(111) surface in ultrahigh vacuum (UHV) conditions has not been undertaken. Whereas on Cu(111) the adsorbed molecules show a strong interaction with the substrate and undergoes a catalytically induced dissociation, on Ag(111) the biomolecules self-assemble above a critical temperature into linear structures primarily following the substrate crystalline symmetry. Our high resolution topographical STM data reveals hydrogen-bonded molecular dimerization within the highly ordered one-dimensional nanostructures, which recalls the geometrical pattern already seen in the *L*-methionine/Ag(111) system and supports a universal self-assembling scheme for amino acids on the Ag(111) surface. Moreover, the molecules desorb when the system is heated above 350 K indicating that the interaction force between the molecules and the Ag(111) surface is relatively weak. Supporting x-ray photoelectron spectroscopy (XPS) and near-edge x-ray absorption fine structure (NEXAFS) experiments were carried out in order to obtain chemical and intramolecular conformational information on the system. Whereas XPS shows a zwitterionic adsorption, the NEXAFS measurements show a non-flat adsorption of the phenyl ring with respect to the substrate plane, allowing possible $\pi - \pi$ interactions between adjacent molecules.

7.2 Experimental section

All experiments were carried out in UHV at a base pressure of 2×10^{-10} mbar. The STM measurements were performed in a custom-designed UHV chamber equipped with a commercial state-of-the-art Besocke-type low-temperature STM [84]. The monocrystalline Ag(111) and Cu(111) substrates were cleaned by successive cycles of Ar⁺ sputtering at 4 μ A and 1 eV, and annealing at 770 K. The L-tyrosine molecules (Sigma-Aldrich, purity $\geq 99.0\%$) were deposited onto the noble metal surfaces by organic molecular beam epitaxy. The amino acid powder was evaporated by resistive heating at 370 K from a quartz crucible. During the sample preparation, the substrate was held at temperatures between 170 and 320 K. After preparation, the sample was cooled down below 15 K for *in situ* STM observations. All the presented topographical STM images were obtained by the constant-current method. The x-ray experiments were accomplished at the ALOISA beamline of the ELETTRA synchrotron. The x-ray beam is characterized by an intensity of 4×10^{10} photons/(s \cdot mm²) and an elliptical photon polarization factor of 0.95 [44]. Due to this high polarization factor, we assume that the beam exhibits perfect linear polarization. The samples were prepared *in situ* under the same conditions as for the STM section. The XPS measurements were performed for submonolayer and saturated monolayer preparations, the spectra showing no molecular coverage dependence, whereas for NEXAFS only the saturated monolayer case was considered. During these x-ray measurements, the sample was held at a temperature of ~ 200 K to minimize x-ray induced effects [89]. The XPS spectra were obtained with a photon beam energy of 600 eV and an incident beam grazing angle of 3°. The absolute

binding energy was calibrated by tuning the spectra with the substrate Ag 3d peaks. The NEXAFS data were acquired with a incident grazing angle of 7° and were normalized by dividing the saturated monolayer partial yield signal with the one of the clean substrate. The high photon polarizability permits studying the polarization dependence of the NEXAFS spectra and therefore gaining intramolecular conformational information. The sample can be rotated around the axis defined by the intersection of the incidence and substrate planes, hence the x-ray absorption dependence with respect to photon polarization is considered for the same photon incident angle. The absolute photon energy was calibrated by identifying in absorption spectra the C 1s $\rightarrow \pi^*$ resonance of gas phase CO in the ALOISA ionization cell [44].

7.3 Results and discussion

7.3.1 Mesoscopic biomolecular self-assembly into two-dimensional zwitterionic nanoribbons

The morphology of the *L*-tyrosine self-assembly on Ag(111) is illustrated in the topographical STM images in Fig. 7.1(b) and 7.1(c). Figure 7.1(a) depicts the structure model of the *L*-tyrosine amino acid. We define here the angle γ as the angle between the phenyl ring and the molecular adsorption plane. When the molecules are deposited onto the Ag(111) held at 170 K, the system has access to enough thermal energy allowing the molecules to diffuse to the step edges. However, the molecules gather in clusters and show no particular ordering pattern (Fig. 7.1(c)). The STM image in Fig. 7.1(b) illustrates the same sample preparation that in Fig. 7.1(c), but after being annealed at a temperature 320 K for 5 minutes. Here we observe the emer-

gence of supramolecular ribbons. These features show a bias-independent apparent height of 2.0 ± 0.2 Å. The thermally induced molecular rearrangement observed from Fig. 7.1(c) to Fig. 7.1(b) implies that a certain activation barrier has to be overcome to form the linear ordering of the supramolecular arrays. The inset represents an atomic resolution image of the underlying Ag(111) substrate, allowing to determine the growth orientations of the linear biomolecular self-assembly with respect to the Ag(111) atomic lattice. The supramolecular architectures can be segregated in two different groups α and β , α being composed of biomolecular entities following the $\langle 110 \rangle$ crystalline orientations of the substrate, whereas the structures β follow a $-40^\circ \pm 2^\circ$ tilt with respect to the α entity. These preferred orientations of the molecular growth demonstrates the influence of the substrate symmetry on the self-assembly and can be the reflection of different commensurate structures. Moreover, the extension of phase β with a -40° angle is non-mirror symmetric with respect to the substrate close-packed crystallographic axis. This reveals the enatiomorphism of the biomolecular self-assembly, which is the consequence of the chirality of the amino acid. However, the substrate-molecule interaction seems not stringent, as reflected by the fact that the nanostructures can be easily manipulated in their orientation during the STM data acquisition. This is corroborated by the low molecular desorption temperature, occurring when the system is heated above 350 K.

When adsorbed on Cu(111) at a substrate temperature of 290 K, the *L*-tyrosine amino acid dissociates into three different types of fragments which one assigns to distinctive parts of the biomolecule (Fig. 7.1(d)). The molecules being deposited on Cu(111) under the same conditions as on Ag(111)

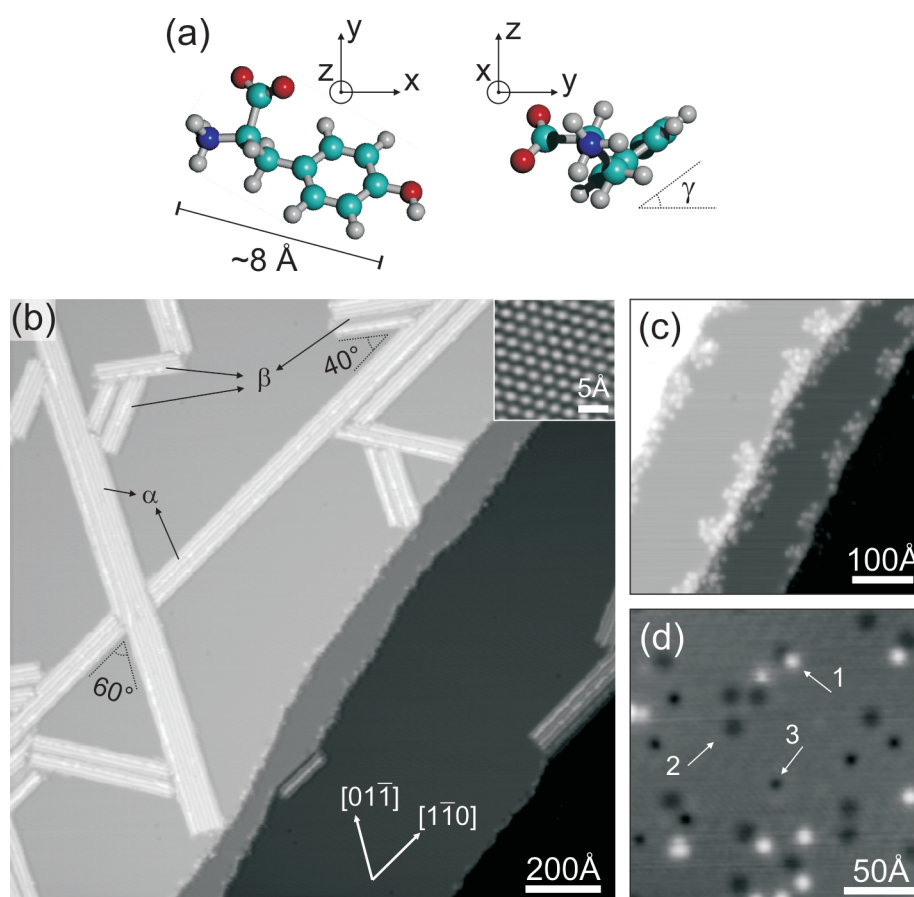


Figure 7.1: STM topographs of *L*-tyrosine on Ag(111) and Cu(111). (a) Structure model of the *L*-tyrosine amino acid zwitterion. We define γ as the angle between the adsorption plane and the phenyl plane. Color code: cyan (C), red (O), blue (N), white (H). (b) *L*-tyrosine on Ag(111) deposited at 170 K and annealed at 320 K: biomolecular domains extend under the influence of the substrate symmetry ($I=0.1$ nA, $V=500$ mV). Inset: atomic resolution of Ag(111). (c) Deposition on Ag(111) at 170 K: molecules diffuse into unordered clusters and decorate the step edges ($I=0.1$ nA, $V=500$ mV). (d) *L*-tyrosine on Cu(111) at 290 K: substrate-mediated dissociation of the molecules into three distinct types of fragments ($I=0.06$ nA, $V=-400$ mV).

irrefutably demonstrates that these observed entities correspond to fragments of the amino acid and not to a possible contamination of the surface. The chemical nature of the submolecular units was not established, and further spectroscopic studies would be required for this purpose. This molecular fragmentation can be explained by a chemical dissociation catalytically triggered by the Cu(111) surface, the latter being highly reactive in comparison with the Ag(111) surface. This phenomenon is different from the cases of *L*-methionine on Cu(111) and more surprisingly different than *L*-tyrosine on Cu(111) in solution [199]. In comparison with the *L*-methionine/Cu(111) system, this dissociation process can be due to the increased reactivity of the side-chain containing the hydroxyl group, whereas in the case of *L*-tyrosine on Cu(111) studied in solution by Wang *et al.* the solvent might stabilize the molecular structure by screening the reactivity of the amino acid functional groups or/and occupying the adsorption sites on the surface.

In order to resolve the chemical and conformation state of the molecules within the self-assembly on Ag(111), we performed XPS and NEXAFS spectroscopy measurements. Figure 7.2 illustrates the N 1s and O 1s XPS spectra resolving the chemical state of the amino acid functional groups. These data correspond to the low temperature sample preparation at 170 K. Measurements for the high temperature preparation were also carried out, showing no temperature dependence on the system chemical state. The NEXAFS data also showed no variation with the sample preparation temperature, demonstrating that the ordered high temperature phase is not triggered by a chemical reaction or a conformational change of the molecular geometry, but that it is only dictated by the growth kinetics. The XPS data was fitted with

Voigt functions in order to identify the associated chemical environments of the N and O atoms. The N 1s spectrum in Fig. 7.2(a) could be fitted with only one Voigt peak centered at a binding energy of 402.31 ± 0.01 eV. By comparing with the *L*-methionine self-assembly on the same Ag(111) substrate, we conclude that this peak corresponds to an ammonium group NH_3^+ . This ammonium related N 1s peak for the *L*-methionine/Ag(111) system was centered at a binding energy of 401.15 eV, showing a discrepancy of more than 1 eV with respect to the *L*-tyrosine case. This variation in binding energy can be due to an increased distance between the ammonium group and the metal surface, resulting in a reduced screening process of the nitrogen nucleus positive potential by the substrate conduction electrons. The assignment of this peak to an ammonium group is confirmed by Fig. 7.2(c): here, a second N 1s peak appears induced by x-ray exposure. This peak, positioned at a binding energy of 399.76 ± 0.48 eV, is associated with an amino group and provides evidence of an x-ray mediated deprotonation of the ammonium group. This is deduced through comparison with work from Zubavichus *et al.* [202]. On the other hand, the O 1s XPS spectrum in Fig. 7.2(b) was fitted with two Voigt peaks of similar intensities placed at binding energies of 532.00 ± 0.17 and 533.44 ± 0.09 eV. By comparing with the literature [202], these are assigned respectively to the equivalent resonant oxygens of the carboxylate group and the hydroxyl group of the side chain. According to this interpretation, we deduce a zwitterionic state for the adsorbed species, similar to the *L*-methionine/Ag(111) system. The similar intensities of both O 1s XPS peaks might seem surprising given the 2:1 stoichiometric ratio between the carboxylate and hydroxyl oxygens. A plausible explanation could

be linked to the possible partial coverage of one of the carboxylate oxygen atoms within the supramolecular assembly, causing the attenuation of the related O 1s XPS peak.

7.3.2 NEXAFS measurements

NEXAFS measurements were performed for the C 1s edge in order to obtain orientational information of the phenyl group with respect to the Ag(111) substrate plane. These measurements were carried out for the low and high temperature phases, the spectra showing no temperature dependence. Therefore, the intramolecular conformational geometry can be considered identical for both phases. The high temperature phase spectra for the p (red) and s (black) polarizations are summarized in Fig. 7.3. The partial electron yield spectra were fitted, in both cases, using the building-block approach [92] by Voigt (labeled 'V' in Table 7.1) and Gaussian (labeled 'G') functions. A step function was considered to take account of the ionization potential IP . The fit parameters for these spectra are summarized in Table 7.1.

The different chemical assignments of the peaks were determined by comparing with previous work from Kaznatcheyev *et al.* [135]. In Table 7.1, Ph stands for the side chain phenyl ring, C_α for the chiral center carbon atom, and $C_\#$ for the carbon atom on the phenyl ring which is attached to C_α . For the p-polarization case (s-polarization, respectively), the step-like onset at IP was approximated by an error function of height 0.47 [a.u.] (0.36 [a.u.], respectively) centered at a photon energy of 294.2 eV (293.0 eV, respectively). The sharp features on the spectra positioned at photon energies below the ionization potential are related to the π^* resonances of the system

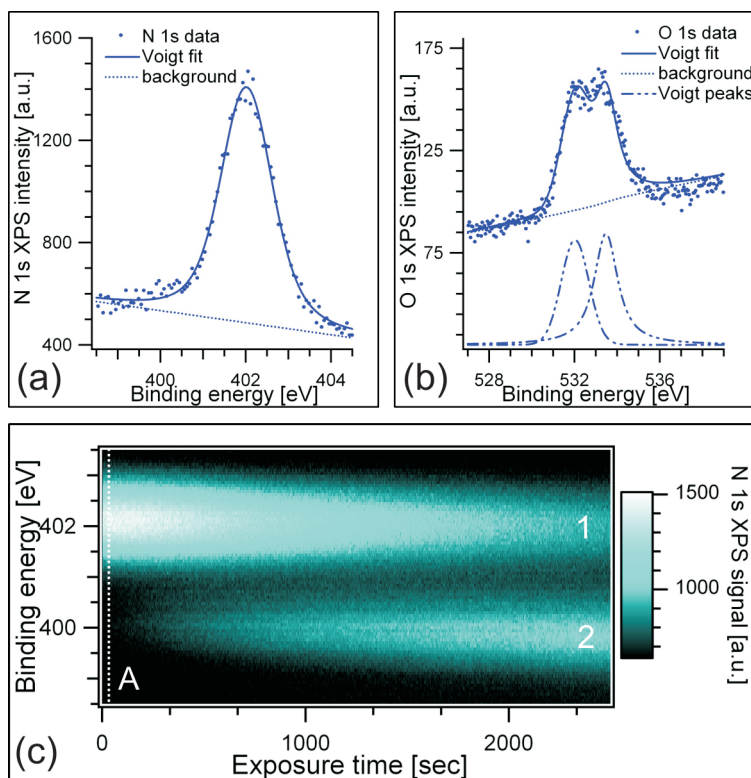


Figure 7.2: N 1s and O 1s XPS measurements of *L*-tyrosine on Ag(111) for the low temperature phase. (a) Data points are fitted with a single Voigt curve and a linear background. The single XPS N 1s peak at a binding energy of 402.31 ± 0.01 eV is assigned to the ammonium group NH_3^+ . (b) Data points are fitted with two Voigt curves and a linear background. The two XPS O 1s peaks at binding energies of 532.00 ± 0.17 eV and 533.44 ± 0.09 eV are assigned to the equivalent resonant oxygen atoms of the carboxylate group COO^- and to the oxygen atom of the hydroxyl group OH respectively. Dot-lined curves represent the two fitting Voigt functions. (c) N 1s XPS data with respect to x-ray exposure time: appearance of a second N 1s peak at a binding energy of 399.76 ± 0.48 eV reveals x-ray induced deprotonation of the ammonium group into a neutral amino group NH_2 . The XPS profile along line A corresponds to the XPS spectrum in (a).

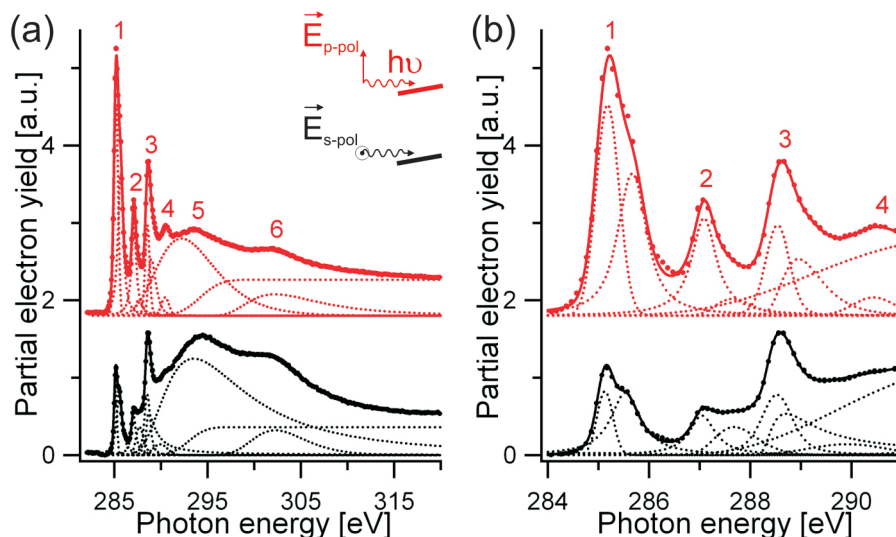


Figure 7.3: C 1s NEXAFS measurements of the *L*-tyrosine/Ag(111) system for the saturated monolayer high temperature phase. (a) C 1s absorption edge for p-polarized (red) and s-polarized (black) x-rays. Dots represent the experimental data, dotted lines represent the fitting peaks and the solid line represents the resulting total fit. Decreased signal intensity of the π^* resonances for the s-polarization data reveals a preferred adsorption orientation of the phenyl π system. The phenyl ring adsorbs in an oblique fashion with respect to the substrate. (b) Detail of the pre-ionization potential zone related to the π^* resonances. Spectra are shifted for clarity.

and were approximated by Voigt functions. The broader features are related to the σ^* resonances and were fitted with Gaussian curves [92]. The fluctuations in energy of the peak positions for the same assigned resonance are due to the fitting procedure. The sharp feature appearing between ~ 285.0 - 285.5 eV (see Table 7.1) corresponds to the π^* resonances related to the phenyl π system. Its strong dichroism reveals a preferred adsorption angle for the phenyl group with respect to the surface plane and a preferred intramolecular conformation upon adsorption: if the adsorbed molecules showed a random

Table 7.1: C 1s NEXAFS fitting parameters for the p and s-polarization spectra presented in Fig. 7.3. 'V' and 'G' stand for Voigt and Gaussian fitting functions respectively.

Pol.	Peak position [eV]	Area [a.u.]	Assignment	Label
p	285.2	1.52 (V)	C 1s(C-H) \rightarrow π^* (Ph)	1
s	285.1	0.33 (V)		
p	285.7	1.83 (V)	C 1s(C _#) \rightarrow π^* (Ph)	1
s	285.5	0.90 (V)		
p	287.1	1.69 (V)	C 1s(C-OH) \rightarrow π^* (Ph)	2
s	287.1	0.49 (V)		
p	287.7	0.20 (G)	C 1s \rightarrow σ^* (C-H)	2
s	287.7	0.38 (G)		
p	288.5	0.75 (V)	C 1s \rightarrow π^* (COO ⁻)	3
s	288.5	0.75 (V)		
p	289.0	0.75 (G)	C 1s \rightarrow σ^* (C-N-H)	3
s	289.1	1.02 (G)		
p	290.4	0.24 (G)	C 1s \rightarrow σ^* (C-C,Ph) or C 1s(C _{α}) \rightarrow σ^* (C-N)	4
s	289.9	0.27 (G)		
p	292.7	8.11 (G)	C 1s(C _{α}) \rightarrow σ^* (C-C)	5
s	295.2	16.8 (G)		
p	303.35	2.99 (G)	C 1s(C-OH) \rightarrow σ^* (C-OH)	6
s	302.63	2.33 (G)		

internal geometry, both p and s-polarization signals should average to the same value. The temperature independence of the spectra reveals the same conformation for both phases and the thermal activated ordering of the ribbons is not related to an intramolecular conformational change, but to the system kinetics. Also, the non-null signal of the s-polarization peak related to the phenyl π^* (Ph) resonances indicates a non-flat adsorption of the phenyl ring with respect to the substrate plane. Now, given the threefold symmetry of the substrate, and that the π^* (Ph) orbital is oriented perpendicular to the phenyl plane following an angle δ with respect to the polarized photon

electric field $\vec{\epsilon}$, equation 2.17 yields for the angle γ between the phenyl and the substrate planes:

$$\gamma(I_p, I_s) = \arcsin \sqrt{\frac{2 \cos^2 \theta}{(I_p/I_s) + 3 \cos^2 \theta - 1}} \quad (7.1)$$

where θ is the photon incident angle (here, $\theta \cong 7^\circ$), and I_p and I_s are respectively the p and s-polarization NEXAFS intensities related to the $\pi^*(\text{Ph})$ resonances. In this expression, a perfectly linear polarization of the x-ray beam is assumed. The intensities I_p and I_s are given by the areas of the fitting Voigt functions corresponding to the $\text{C } 1s \rightarrow \pi^*(\text{Ph})$ transitions, and deriving an angle γ for each of the three $\pi^*_{(\text{Ph})}$ resonances related to the phenyl ring (see Table 7.1 for the respective orbital assignments of the NEXAFS peaks), we obtain an average adsorption angle of $\langle \gamma \rangle = 38^\circ \pm 9^\circ$. The error on this value due to the hypothesis of a perfect linear polarization is of the order of 0.1° , which is negligible compared to the error related to the fitting procedure.

7.3.3 Molecular arrangement within the nanoribbons: zwitterionic coupling scheme

Details on the molecular disposition within the ordered biomolecular arrays on Ag(111) are displayed in the high resolution STM topographs in Fig. 7.4(a) and 7.4(b). We focus here on the nanoribbons composing structure α of the high temperature phase i.e. the one expanding along the $\langle 110 \rangle$ orientations of the substrate. Figure 7.4(a) displays a STM image of a biomolecular chain which self-assembled with the substrate held at 240 K. The one-dimensional structure is composed of identically-shaped elliptical units, each of which

we assign, due to geometrical arguments, to a single *L*-tyrosine zwitterion. Within these 1D chains, the amino acid molecules appear always in pairs bonded adjacently in the 1D extension direction: no odd numbered structures are observed. This molecular dimerization and adjacent bonding pattern has been already revealed in the self-assembly of the *L*-methionine amino acid on Ag(111) (see previous Chapters). Along the linear extension orientation, the *L*-tyrosine chain shows a molecular periodicity of 5.7 ± 0.1 Å (inset in Fig. 7.4(a)), showing commensurability of the structure in this direction, as this value corresponds to the double of the Ag(111) lattice constant along the closed-packed orientations $\langle 110 \rangle$ ($a_{\text{Ag}(111)} = 2.89$ Å).

A key difference between the *L*-methionine and *L*-tyrosine self-assemblies on the same substrate is the lack of formation of regular nanogratings in the latter. This is observed in Fig. 7.4(b), where wider molecular domains evolve after annealing the system up to 320 K. The absence of repulsive interactions between these simpler chains allowing the formation of the wider domains are most likely due to the chemical reactivity of the amino acid side chain. Effectively, the hydroxyl group and aromatic system of the side-chain can mediate hydrogen bonding and π - π stacking respectively, the latter being enabled by the oblique adsorption geometry of the phenyl ring revealed by the NEXAFS measurements.

The molecular arrangement within these wider domains is periodic, as seen in Fig. 7.4(b). The supramolecular unit cell is defined by the vectors \vec{a}' and \vec{b}' . Considering the periodic atomic lattice of the Ag(111) substrate and its unit cell given by vectors \vec{a} and \vec{b} , one can explicitly associate the supramolecular and substrate periodicities, and write $\vec{a}' = 2\vec{a}$ and $\vec{b}' = \vec{a} - 5\vec{b}$.

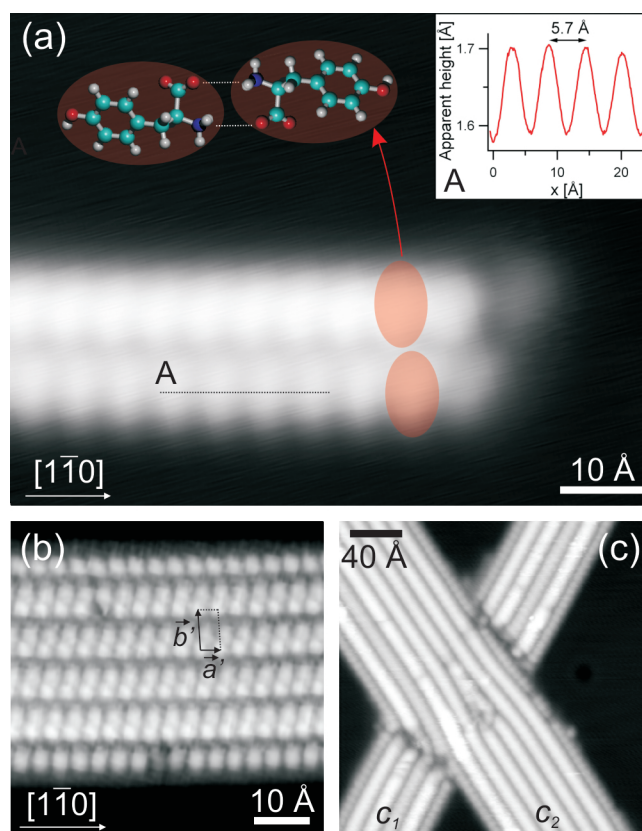


Figure 7.4: High resolution STM data of the biomolecular self-assembly of *L*-tyrosine on Ag(111). (a) Biomolecular chain extending along the $[1, \bar{1}, 0]$ crystalline orientation of the Ag(111) substrate. Molecules dimerize along their long axis and bind adjacently and commensurably with the atomic lattice along the chain direction ($I=0.2$ nA, $V=500$ mV). The two red ellipses represent two molecules forming a hydrogen-bonded dimer. Inset: apparent height profile along A. (b) Molecular arrangement in wider domains which appear after annealing at 320 K: the intermolecular bonding scheme is more complex than for simple bimolecular rows ($I=0.07$ nA, $V=500$ mV). (c) Chain merging and inter-crossing evidences the complex dynamics of the molecular self-assembly process ($I=0.1$ nA, $V=500$ mV).

The biomolecular domain is therefore commensurate with the underlying

substrate.

The STM data reveals also the complexity of the dynamics of the self-assembly process. This is depicted in Fig. 7.4(c), where a biomolecular domain which we label as c_1 is segmented by a wider domain c_2 . The fact that both segments of c_1 present the same width, growth orientation and intradomain imaging contrast is a strong indication that these sections were part of the same initial structure, and that the segmentation is directly due to the merging of c_1 with the wider structure c_1 . This demonstrates an intricate dynamic behavior during the self-assembly process, motivating further studies.

7.4 Conclusion

To conclude, our high-resolution low-temperature STM observations resolved the anisotropic self-assembly of the *L*-tyrosine amino acid on Ag(111). Our data revealed the influence of the substrate symmetry on the morphology of the biomolecular nanostructures and the molecular organization pattern within the supramolecular domains. The XPS data showed evidence of a zwitterionic adsorption configuration at all temperatures, and NEXAFS results provided proof that the side chain aromatic system adsorbs in an oblique fashion with respect to the substrate plane.

We want to emphasize here the similarity of the self-assembly with the *L*-methionine/Ag(111) system and the strong hint that the self-assembly scheme of amino acids on the Ag(111) surface must follow a universal trend driven by non-covalent attractive interactions between the carboxylate and ammonium functional groups. The difference between the two systems re-

garding their mesoscopic ordering is a consequence of the intramolecular geometry and chemical reactivity of the side chains.

It is important to point out that this study on the biomolecular self-assembly of *L*-tyrosine on Ag(111), whose one-dimensionality have been proposed beforehand, has proven that the knowledge of supramolecular interactions is progressing from trial-and-error-type experiments to predictable and systematic exploitation of certain functionalities. In this particular case, the linear ordering of the molecular assembly could be directly associated with the amino and carboxylic acid functional groups. This approach can represent a general pathway for the non-covalent synthesis of one dimensional architectures at the nanoscale, yielding an example of control and nanopatterning potentiality on surfaces for a possible and applicable 'bottom-up' miniaturization procedure in the perspective of designing novel functional devices.

The experiments were performed at the Advanced Materials and Process Engineering Laboratory (AMPEL) at the University of British Columbia in collaboration with Dr. J. Reichert, Dr. Y. Pennec, Dr. W. Auwärter, Dr. A. Weber-Bargioni, M. Marshall and Dr. J.V. Barth, and at the ALOISA beamline of the ELETTRA synchrotron light source in collaboration with Dr. D. Cvetko, Dr. A. Cossaro, Dr. G. Bavdek, M. Dell'Angela and Dr. A. Morgante.

Chapter 8

Outlook

The work presented in this thesis expounds the characterization of novel molecular self-assemblies of the amino acids methionine and tyrosine on the closed-packed noble metal surfaces Ag(111) and Cu(111). The systems were structurally resolved at the molecular level by means of real-space STM measurements supported by diffraction HAS data, whereas the spectroscopic x-ray absorption techniques XPS and NEXAFS provided information on the chemical and conformational states of the adsorbed species, respectively. The inherent properties of these biomolecules were used for the 'bottom-up' design of self-assembled nanostructures. This approach demonstrated exquisite control of matter at the molecular level, in terms of nanoscale morphology, engineering of electronic quantum well states, and steering the alignment of single atoms.

On Ag(111), both homochiral amino acid self-assemblies are driven by zwitterionic hydrogen-bonded molecular dimerization involving the carboxylate and ammonium groups, where the high-symmetry axis of the underlying silver substrate influence the directionality of the biomolecular nanostructures. The long-range linear order of the biomolecular nanostructures mediated by the H-bonded dimerization process suggests a universal trend for the one-dimensional zwitterionic non-covalent synthesis of amino acid superstructures on Ag(111). Exploiting this molecular self-assembly properties exhibits

potentialities for the two-dimensional control and patterning of matter at the nanoscale. Beyond these similarities, the morphological discrepancy between both supramolecular equilibrium configurations is due to the different chemical reactivity of the respective side chains. In the case of methionine, it resides in the formation of extended one-dimensional chains composing regular biomolecular nanogratings with tunable periodicity, whereas tyrosine's arrangements consist in two-dimensional ribbon-like domains. If the general amino acid self-assembly phenomenon can be exploited for the design of robust molecular nanoarchitectures on surfaces, the tuning of the amino acid side chain is a key control parameter for the structural determination of the final relaxed supramolecular state.

The regularity, tunability and low-dimensionality of the methionine/Ag(111) system were successfully exploited as one-dimensional electronic resonators, the variation of the electronic confinement length allowing to set the quantum boundary conditions and therefore to influence in a controlled fashion the surface electronic state. The nanoscaled low-dimensional biomolecular architectures were also used as templates for the steering of the one-dimensional self-alignment process of transition metal adatoms. Here, it was demonstrated how electronic and positioning control on surfaces can be gained by taking advantage of the inherent self-assembly capabilities of biomolecules and their influence on the substrate electronic structure.

The characteristics of the stable molecule-substrate system are not only determined by the interactions between the adsorbed organic species, but the influence of the substrate plays a key role, as revealed in the methionine/Cu(111) system. In the latter, the chemical properties of the sup-

porting copper substrate have a catalytic function which mediates thermally induced chemical reactions of the supramolecular ensemble, implying consequent structural alterations of the adsorbed nanosystem. Moreover, our combined topographic and spectroscopic analysis revealed the heterogeneity of the active site distribution on the surface, providing an example of heterogeneous catalysis on biomolecules at the molecular level.

The results of this work bring new interrogations which motivate further studies. For instance, the nature of the long-range substrate-mediated inter-chain repulsion between the methionine nanowires on Ag(111), which is responsible for the high regularity of the nanogratings, has not been completely elucidated. The main suspects for this repulsive mediation are the surface state electrons and strain. If the influence of the biomolecular adsorption on the electronic surface state band has been successfully determined, the effect of these electronic states on the self-assembly process still needs to be investigated. For this purpose, theoretical considerations and the use of crystalline substrates not presenting a surface state band should be considered. Furthermore, heterochiral systems composed of both enantiomers of the same amino acid should be studied in order to address plausible general chiral recognition patterns and their correlation with enantioselectivity in more complex biological systems. Such chiral selectivity processes have already been observed in specific systems at the molecular level [72], but a general mechanism still needs to be depicted. In terms of applications of such self-assembly processes, the combination of 'bottom-up' approaches with 'top-down' techniques can be envisaged and, for example, self-assembled masks can be developed for nanoscaled lithographic procedures [30]. Moreover, supramolecular

self-assembly protocols can be considered to create nanotemplates steering robust covalently bound nanostructures with specific functionalities. From the fundamental biological point of view, elementary interactions between amino acids and small peptides with metal centers can be envisioned in order to unravel their effects in physiological conditions.

The conclusions exposed in this thesis are the result of the synergy between atomic scale structural data and spectroscopic measurements providing chemical and electronic information on the studied systems. This strategy requires to combine local nanoscopic details of the system's morphology with a macroscopic average of the its spectroscopic properties, which can render the interpretation problematic in the case of heterogeneous systems. The nanoscale characterization of organic species adsorbed on surfaces demands further development in the field of local chemical probes with high spatial resolution. For instance, inelastic electron tunneling spectroscopy (IETS) with STM allows probing the chemical identity of single adsorbed species as well as the nature of the substrate-molecule bonding. Developed by Ho *et al.* [40, 205], this approach, consisting in the spectroscopic detection of molecular vibrational modes excited by inelastic interactions with the tunneling electrons, is highly sensitive to the chemical environment of the adsorbed molecule. This promising technique yields however complex characteristic spectra for the determination of specific functional groups in large organic molecules. Further non-destructive techniques showing potential for probing the local chemical properties of adsorbed organic systems include surface-enhanced Raman spectroscopy (SERS) [132, 133, 206], x-ray based spectroscopic methods with nanoscopically focused beams [207, 208] and near-field

scanning optical spectroscopy (NSOM) [209].

Finally, it is important to point out that the results exhibited here have a fundamental character, and that a rather wide gap still remains in order to reach relevance in industrial device technology exploiting the molecular self-assembly paradigm. As an example, in terms of electronic nanodevices, two-dimensional systems need to be electronically decoupled from the supporting substrate electronic states, and further studies of molecular self-assembly on insulating layers should be undertaken. Although the electronic properties of single adsorbed species on insulating substrates have already been studied by means of STM [210–212], a molecular self-assembly route on such surfaces still needs to be considered. What we defined as Moore’s Law in our introductory remarks represents more an empirical requirement to maintain the growth of the semiconductor industry than a simple statistical trend, and there is strong economical pressure for the development of novel mass-scale nanofabrication procedures.

Chapter 9

Publications

A. Schiffrin, A. Riemann, W. Auwärter, Y. Pennek, A. Weber-Bargioni, D. Cvetko, A. Cossaro, A. Morgante, and J.V. Barth. Zwitterionic self-assembly of *L*-methionine nanogratings on the Ag(111) surface. *Proceedings of the National Academy of Science of the United States of America*, 104 (13): 5279-5284, 2007.

Y. Pennek, W. Auwärter, A. Schiffrin, A. Weber-Bargioni, A. Riemann, and J.V. Barth. Supramolecular gratings for tuneable confinement of electrons on metal surfaces. *Nature Nanotechnology*, 2 (2): 99-103, 2007.

W. Auwärter, A. Weber-Bargioni, A. Riemann, A. Schiffrin, O. Gröning, R. Fasel, and J.V. Barth. Self-assembly and conformation of tetrapyrrolyl-porphyrin molecules on Ag(111). *Journal of Chemical Physics*, 124 (19): 194708, 2006.

W. Auwärter, A. Weber-Bargioni, S. Brink, A. Riemann, A. Schiffrin, M. Ruben, and J.V. Barth. Controlled metalation of self-assembled porphyrin nanoarrays in two dimensions. *Chemphyschem*, 8 (2): 250-254, 2007.

W. Auwärter, F. Klappenberger, A. Weber-Bargioni, A. Schiffrin, T. Strun-

skus, C. Wöll, Y. Pennec, A. Riemann, and J.V. Barth. Conformational adaptation and selective adatom capturing of tetrapyrrolyl-porphyrin molecules on a copper (111) surface. *Journal of the American Chemical Society*, 129 (36): 11279-11285, 2007.

A. Weber-Bargioni, W. Auwärter, F. Klappenberger, J. Reichert, S. Lefrançois, A. Schiffrin, Y. Pennec, T. Strunskus, Ch. Wöll, and J.V. Barth. Visualizing the frontier orbitals of a conformationally adapted metalloporphyrin. *ChemPhysChem*, 9 (1): 89-94, 2008.

W. Auwärter, A. Schiffrin, A. Riemann, A. Weber-Bargioni, Y. Pennec, and J.V. Barth. Molecular nanoscience and engineering on surfaces: research activities at UBC. *Int.J.Nanotechnol.*In print.

A. Weber-Bargioni, J. Reichert, A.P. Seitsonen, W. Auwärter, A. Schiffrin, and J.V. Barth. Interaction of cerium atoms with surface-anchored porphyrin molecules. *J. Phys. Chem. C.* In print.

A. Schiffrin, J. Reichert, W. Auwärter, G. Jahnz, Y. Pennec, A. Weber-Bargioni, V.S. Stepanyuk, L. Niebergall, P. Bruno, and J.V. Barth. Self-alignment of transition metal adatoms in surface-supported biomolecular nanogratings. Submitted.

A. Schiffrin, J. Reichert, Y. Pennec, W. Auwärter, A. Weber-Bargioni, M. Marschall, D. Cvetko, A. Cossaro, A. Morgante, and J.V. Barth. Self-

assembly of *L*-methionine on noble metal surfaces: steering enantiomorphic biomolecular nanostructures by substrate reactivity and thermal activation. To be published.

J. Reichert, A. Schiffrin, Y. Pennec, W. Auwärter, A. Weber-Bargioni, M. Marshall, D. Cvetko, A. Cossaro, A. Morgante, and J.V. Barth. *L*-tyrosine on Ag(111): universality of the amino acid bonding scheme. To be published.

M. Eichberger, M. Marschall, J. Reichert, A. Weber-Bargioni, W. Auwärter, Y. Pennec, A. Schiffrin, and J.V. Barth. Dimerization boosts 1D mobility of conformationally adapted porphyrins on a hexagonal surface atomic lattice. To be published.

A. Weber-Bargioni, A. Schiffrin, F. Klappenberger, W. Auwärter, and J.V. Barth. Conformation, chemical nature and metal-directed assembly of tetrapyrrolyl-porphyrin on Cu(111). To be published.

W. Auwärter, N. Negulyayev, A. Weber-Bargioni, A. Schiffrin, V. Stepanyuk, and J.V. Barth. Diffusion and superlattice formation of Fe atoms on Cu(111). To be published.

Bibliography

- [1] Gordon E. Moore. Cramming more components onto integrated circuits. *Electronics*, 38(8), 1965.
- [2] B. D. Gates, Q. B. Xu, M. Stewart, D. Ryan, C. G. Willson, and G. M. Whitesides. New approaches to nanofabrication: Molding, printing, and other techniques. *Chemical Reviews*, 105(4):1171–1196, 2005.
- [3] M. Switkes, R. R. Kunz, M. Rothschild, R. F. Sinta, M. Yeung, and S. Y. Baek. Extending optics to 50 nm and beyond with immersion lithography. *Journal of Vacuum Science & Technology B*, 21(6):2794–2799, 2003.
- [4] J. Mulkens, D. Flagello, B. Streefkerk, and P. Graeupner. Benefits and limitations of immersion lithography. *Journal of Microlithography Microfabrication and Microsystems*, 3(1):104–114, 2004.
- [5] R. Tiron, L. Mollard, O. Louveau, and E. Lajoinie. Ultrahigh-resolution pattern using electron-beam lithography HF wet etching. *Journal of Vacuum Science & Technology B*, 25(4):1147–1151, 2007.
- [6] Z. N. Yu, W. Wu, G. Y. Jung, D. L. Olynick, J. Straznicky, X. M. Li, Z. Y. Li, W. M. Tong, J. A. Liddle, S. Y. Wang, and R. S. Williams.

-
- Fabrication of 30 nm pitch imprint moulds by frequency doubling for nanowire arrays. *Nanotechnology*, 17(19):4956–4961, 2006.
- [7] C. R. K. Marrian and D. M. Tennant. Nanofabrication. *Journal of Vacuum Science & Technology A*, 21(5):S207–S215, 2003.
- [8] D. Bratton, D. Yang, J. Y. Dai, and C. K. Ober. Recent progress in high resolution lithography. *Polymers for Advanced Technologies*, 17(2):94–103, 2006.
- [9] G. Y. Jung, S. Ganapathiappan, X. Li, D. A. A. Ohlberg, D. L. Olynick, Y. Chen, W. M. Tong, and R. S. Williams. Fabrication of molecular-electronic circuits by nanoimprint lithography at low temperatures and pressures. *Applied Physics A: Materials Science & Processing*, 78(8):1169–1173, 2004.
- [10] J. T. Robinson, P. G. Evans, J. A. Liddle, and O. D. Dubon. Chemical nanomachining of silicon by gold-catalyzed oxidation. *Nano Letters*, 7(7):2009–2013, 2007.
- [11] M. Schulz. The end of the road for silicon? *Nature*, 399(6738):729–730, 1999.
- [12] Arie Aviram and Mark A. Ratner. Molecular rectifiers. *Chemical Physics Letters*, 29(2):277–283, 1974.
- [13] D. M. Eigler and E. K. Schweizer. Positioning single atoms with a scanning tunneling microscope. *Nature*, 344(6266):524–526, 1990.

-
- [14] F. Rosei. Nanostructured surfaces: challenges and frontiers in nanotechnology. *Journal of Physics-Condensed Matter*, 16(17):S1373–S1436, 2004.
- [15] J.V. Barth, G. Costantini, and K. Kern. Engineering atomic and molecular nanostructures on surfaces. *Nature*, 437:671–679, 2005.
- [16] A. Klug. From macromolecules to biological assemblies (Nobel lecture). *Angew. Chem. Int. Ed.*, 22:565–582, 1983.
- [17] A. Klug. The tobacco mosaic virus particle: structure and assembly. *Philosophical Transactions of the Royal Society of London Series B-Biological Sciences*, 354(1383):531–535, 1999.
- [18] L. J. Prins, D. N. Reinhoudt, and P. Timmerman. Non-covalent synthesis using hydrogen bonding. *Angewandte Chemie-International Edition*, 40(13):2383–2426, 2001.
- [19] D. J. Kushner. Self-assembly of biological structures. *Bacteriological Reviews*, 33(2):302, 1969.
- [20] M. Eigen. Self-organization of matter and evolution of biological macromolecules. *Naturwissenschaften*, 58(10):465, 1971.
- [21] K. Namba. Roles of partly unfolded conformations in macromolecular self-assembly. *Genes to Cells*, 6(1):1–12, 2001.
- [22] G. Lebeurier, A. Nicolaieff, and K. E. Richards. Inside-out model for self-assembly of tobacco mosaic-virus. *Proceedings of the National*

-
- Academy of Sciences of the United States of America*, 74(1):149–153, 1977.
- [23] J. M. Lehn. Supramolecular chemistry - receptors, catalysts, and carriers. *Science*, 227(4689):849–856, 1985.
- [24] J. S. Lindsey. Self-assembly in synthetic routes to molecular devices - biological principles and chemical perspectives - a review. *New Journal of Chemistry*, 15(2-3):153–180, 1991.
- [25] G. M. Whitesides, J. P. Mathias, and C. T. Seto. Molecular self-assembly and nanochemistry - a chemical strategy for the synthesis of nanostructures. *Science*, 254(5036):1312–1319, 1991.
- [26] J. M. Lehn. Supramolecular chemistry. *Science*, 260(5115):1762–1763, 1993.
- [27] D. Philp and J. F. Stoddart. Self-assembly in natural and unnatural systems. *Angewandte Chemie-International Edition in English*, 35(11):1155–1196, 1996.
- [28] M. Sarikaya, C. Tamerler, A. K. Y. Jen, K. Schulten, and F. Baneyx. Molecular biomimetics: nanotechnology through biology. *Nature Materials*, 2(9):577–585, 2003.
- [29] C. Valery, M. Paternostre, B. Robert, T. Gulik-Krzywicki, T. Narayanan, J. C. Dedieu, G. Keller, M. L. Torres, R. Cherif-Cheikh, P. Calvo, and F. Artzner. Biomimetic organization: Octapeptide self-assembly into nanotubes of viral capsid-like dimension. *Proceedings*

-
- of the National Academy of Sciences of the United States of America*, 100(18):10258–10262, 2003.
- [30] J. A. Liddle, Y. Cui, and P. Alivisatos. Lithographically directed self-assembly of nanostructures. *Journal of Vacuum Science & Technology B*, 22(6):3409–3414, 2004.
- [31] K. Tanaka, G. H. Clever, Y. Takezawa, Y. Yamada, C. Kaul, M. Shionoya, and T. Carell. Programmable self-assembly of metal ions inside artificial DNA duplexes. *Nature Nanotechnology*, 1(3):190–194, 2006.
- [32] G. H. Clever, C. Kaul, and T. Carell. DNA-metal base pairs. *Angewandte Chemie-International Edition*, 46(33):6226–6236, 2007.
- [33] B. Kasemo. Biological surface science. *Surf. Sci.*, 500:656–677, 2002.
- [34] J. Wintterlin, S. Volkening, T. V. W. Janssens, T. Zambelli, and G. Ertl. Atomic and macroscopic reaction rates of a surface-catalyzed reaction. *Science*, 278(5345):1931–1934, 1997.
- [35] G. Ertl. Oscillatory kinetics and spatiotemporal self-organization in reactions at solid-surfaces. *Science*, 254(5039):1750–1755, 1991.
- [36] G. Binnig and H. Rohrer. Scanning tunneling microscopy. *Helv. Phys. Acta*, 55:726, 1982.
- [37] A. Zangwill. *Physics at Surfaces*. Cambridge University Press, 1988.
- [38] G. Binnig, H. Rohrer, C. Gerber, and E. Weibel. (7x7) reconstruction on Si(111) resolved in real space. *Physical Review Letters*, 50(2):120–123, 1983.

-
- [39] H. Ohtani, R. J. Wilson, S. Chiang, and C. M. Mate. Scanning tunneling microscopy observations of benzene molecules on the Rh(111)-(3 × 3)(C₆H₆+2CO) surface. *Physical Review Letters*, 60(23):2398–2401, 1988.
- [40] B. C. Stipe, M. A. Rezaei, and W. Ho. Single-molecule vibrational spectroscopy and microscopy. *Science*, 280(5370):1732–1735, 1998.
- [41] C. S. Atwood, G. Perry, H. Zeng, Y. Kato, W. D. Jones, K. Q. Ling, X. D. Huang, R. D. Moir, D. D. Wang, L. M. Sayre, M. A. Smith, S. G. Chen, and A. I. Bush. Copper mediates dityrosine cross-linking of Alzheimer’s amyloid-beta. *Biochemistry*, 43(2):560–568, 2004.
- [42] S. Varadarajan, S. Yatin, J. Kanski, F. Jahanshahi, and D. A. Butterfield. Methionine residue 35 is important in amyloid beta-peptide-associated free radical oxidative stress. *Brain Research Bulletin*, 50(2):133–141, 1999.
- [43] S. Varadarajan, J. Kanski, M. Aksenova, C. Lauderback, and D. A. Butterfield. Different mechanisms of oxidative stress and neurotoxicity for Alzheimer’s a beta(1-42) and a beta(25-35). *Journal of the American Chemical Society*, 123(24):5625–5631, 2001.
- [44] L. Floreano, G. Naletto, D. Cvetko, Gotter R, M. Malvezzi, L. Marassi, A. Morgante, A. Santaniello, A. Verdini, F. Tommasini, and G. Tonello. Performance of the grating-crystal monochromator of the ALOISA beamline at the Elettra Synchrotron. *Rev. Sci. Instr.*, 70:3855, 1999.

-
- [45] G. Binnig, H. Rohrer, C. Gerber, and E. Weibel. Tunneling through a controllable vacuum gap. *Applied Physics Letters*, 40(2):178–180, 1982.
- [46] J. Tersoff and D. R. Hamann. Theory and application for the scanning tunneling microscope. *Physical Review Letters*, 50(25):1998–2001, 1983.
- [47] J. Tersoff and D. R. Hamann. Theory of the scanning tunneling microscope. *Physical Review B*, 31(2), 1985.
- [48] J. Bardeen. Tunnelling from a many-particle point of view. *Physical Review Letters*, 6(2):57 – 59, 1961.
- [49] C. J. Chen. Microscopic view of scanning tunneling microscopy. *Journal of Vacuum Science & Technology a-Vacuum Surfaces and Films*, 9(1):44–50, 1991.
- [50] A. Selloni, P. Carnevali, E. Tosatti, and C. D. Chen. Voltage-dependent scanning-tunneling microscopy of a crystal-surface - graphite. *Physical Review B*, 31(4):2602–2605, 1985.
- [51] C. Kittel. *Introduction to Solid State Physics*. John Wiley & Sons. Inc., 7th edition edition, 1996.
- [52] G. Doyen, D. Drakova, and M. Scheffler. Green-function theory of scanning tunneling microscopy - tunnel current and current-density for clean metal-surfaces. *Physical Review B*, 47(15):9778–9790, 1993.
- [53] N. D. Lang. Spectroscopy of single atoms in the scanning tunneling microscope. *Physical Review B*, 34(8):5947–5950, 1986.

-
- [54] J. A. Stroscio, R. M. Feenstra, and A. P. Fein. Electronic-structure of the Si(111)-(2x1) surface by scanning tunneling microscopy. *Physical Review Letters*, 57(20):2579–2582, 1986.
- [55] R. M. Feenstra and P. Martensson. Fermi-level pinning at the Sb/GaAs(110) surface studied by scanning tunneling spectroscopy. *Physical Review Letters*, 61(4):447–450, 1988.
- [56] J. T. Li, W. D. Schneider, and R. Berndt. Local density of states from spectroscopic scanning-tunneling-microscope images: Ag(111). *Physical Review B*, 56(12):7656–7659, 1997.
- [57] M. F. Crommie, C. P. Lutz, and D. M. Eigler. Confinement of electrons to quantum corrals on a metal-surface. *Science*, 262(5131):218–220, 1993.
- [58] L. Burgi, O. Jeandupeux, A. Hirstein, H. Brune, and K. Kern. Confinement of surface state electrons in fabry-pérot resonators. *Physical Review Letters*, 81(24):5370–5373, 1998.
- [59] S. Heinze, M. Bode, A. Kubetzka, O. Pietzsch, X. Nie, S. Blugel, and R. Wiesendanger. Real-space imaging of two-dimensional antiferromagnetism on the atomic scale. *Science*, 288(5472):1805–1808, 2000.
- [60] O. Pietzsch, A. Kubetzka, M. Bode, and R. Wiesendanger. Observation of magnetic hysteresis at the nanometer scale by spin-polarized scanning tunneling spectroscopy. *Science*, 292(5524):2053–2056, 2001.
- [61] W. Ho. Single-molecule chemistry. *J. Chem. Phys.*, 117:11033–11061, 2002.

-
- [62] H. Proehl, M. Toerker, F. Sellam, T. Fritz, K. Leo, C. Simpson, and K. Mullen. Comparison of ultraviolet photoelectron spectroscopy and scanning tunneling spectroscopy measurements on highly ordered ultrathin films of hexa-peri-hexabenzocoronene on Au(111). *Physical Review B*, 6320(20):205409, 2001.
- [63] L. Limot, T. Maroutian, P. Johansson, and R. Berndt. Surface-state Stark shift in a scanning tunneling microscope. *Physical Review Letters*, 91(19):196801, 2003.
- [64] J. A. Venables, G. D. T. Spiller, and M. Hanbucken. Nucleation and growth of thin-films. *Reports on Progress in Physics*, 47(4):399–459, 1984.
- [65] J. V. Barth. Transport of adsorbates at metal surfaces: From thermal migration to hot precursors. *Surface Science Reports*, 40(3-5):75–149, 2000.
- [66] D. M. Eigler, P. S. Weiss, E. K. Schweizer, and N. D. Lang. Imaging Xe with a low-temperature scanning tunneling microscope. *Physical Review Letters*, 66(9):1189–1192, 1991.
- [67] J. Winterlin, H. Brune, H. Hofer, and R. J. Behm. Atomic scale characterization of oxygen adsorbates on Al(111) by scanning tunneling microscopy. *Applied Physics a-Materials Science & Processing*, 47(1):99–102, 1988.
- [68] E. Kopatzki and R. J. Behm. STM imaging and local order of oxygen adlayers on Ni(100). *Surface Science*, 245(3):255–262, 1991.

-
- [69] L. Wenzel, D. Arvanitis, W. Daum, H. H. Rotermund, J. Stohr, K. Baberschke, and H. Ibach. Structural determination of an adsorbate-induced surface reconstruction: $p4g(2\times 2)N$ versus $c(2\times 2)O$ on Ni(100). *Physical Review B*, 36(14):7689–7692, 1987.
- [70] P. H. Lippel, R. J. Wilson, M. D. Miller, C. Woll, and S. Chiang. High-resolution imaging of copper-phthalocyanine by scanning tunneling microscopy. *Physical Review Letters*, 62(2):171–174, 1989.
- [71] J. A. Stroscio and D. M. Eigler. Atomic and molecular manipulation with the scanning tunneling microscope. *Science*, 254(5036):1319–1326, 1991.
- [72] A. Kuhnle, T.R. Linderoth, B. Hammer, and F. Besenbacher. Chiral recognition in dimerization of adsorbed cysteine observed by scanning tunneling microscopy. *Nature*, 415:891–893, 2002.
- [73] S.M. Barlow and R. Raval. Complex organic molecules at metal surfaces: bonding, organisation and chirality. *Surf. Sci. Rep.*, 50:201–341, 2003.
- [74] Q. Chen and N.V. Richardson. Enantiomeric interactions between nucleic acid bases and amino acids on solid surfaces. *Nature Materials*, 2:324 – 328, 2003.
- [75] N. D. Lang. Theory of single-atom imaging in the scanning tunneling microscope. *Physical Review Letters*, 56(11):1164–1167, 1986.

-
- [76] N. D. Lang. Apparent size of an atom in the scanning tunneling microscope as a function of bias. *Physical Review Letters*, 58(1):45–48, 1987.
- [77] P. Sautet. Images of adsorbates with the scanning tunneling microscope: Theoretical approaches to the contrast mechanism. *Chemical Reviews*, 97(4):1097–1116, 1997.
- [78] D. Alfe, S. de Gironcoli, and S. Baroni. The reconstruction of Rh(001) upon oxygen adsorption. *Surface Science*, 410(2-3):151–157, 1998.
- [79] T. Zambelli, J. Trost, J. Wintterlin, and G. Ertl. Diffusion and atomic hopping of N atoms on Ru(0001) studied by scanning tunneling microscopy. *Physical Review Letters*, 76(5):795–798, 1996.
- [80] N. Knorr, H. Brune, M. Epple, A. Hirstein, M. A. Schneider, and K. Kern. Long-range adsorbate interactions mediated by a two-dimensional electron gas. *Physical Review B*, 65(11), 2002.
- [81] M. Schunack, T. R. Linderoth, F. Rosei, E. Laegsgaard, I. Stensgaard, and F. Besenbacher. Long jumps in the surface diffusion of large molecules. *Physical Review Letters*, 88(15):156102, 2002.
- [82] T. Zambelli, J. Wintterlin, J. Trost, and G. Ertl. Identification of the 'active sites' of a surface-catalyzed reaction. *Science*, 273(5282):1688–1690, 1996.
- [83] K. Besocke. An easily operable scanning tunneling microscope. *Surface Science*, 181(1-2):145–153, 1987.

-
- [84] G. Meyer. A simple low temperature ultra-high vacuum scanning tunneling microscope capable of atomic manipulation. *Rev. Sci. Instrum.*, 67:2960, 1996.
- [85] K.F. Braun. *Manipulation mit einem Rastertunnelmikroskop bei tiefen Temperaturen*. PhD thesis, Freie Universitaet Berlin, 2000.
- [86] I. Horcas, R. Fernandez, J. M. Gomez-Rodriguez, J. Colchero, J. Gomez-Herrero, and A. M. Baro. WSxM: A software for scanning probe microscopy and a tool for nanotechnology. *Review of Scientific Instruments*, 78(1):013705, 2007.
- [87] D. Cvetko, A. Lausi, A. Morgante, F. Tommasini, K. C. Prince, and M. Sastry. Compact He beam scattering apparatus for surface studies. *Measurement Science and Technology*, 3(10):997–1000, 1992.
- [88] S. Hufner. *Photoelectron Spectroscopy: Principles and Applications*. Springer-Verlag, 2nd edition edition, 1996.
- [89] P. Feulner, T. Niedermayer, K. Eberle, R. Schneider, D. Menzel, A. Baumer, E. Schmich, A. Shaporenko, Y. Tai, and M. Zharnikov. Strong temperature dependence of irradiation effects in organic layers. *Phys. Rev. Lett.*, 93:178302, 2004.
- [90] J.F. Moulder, W.F. Stickle, P.E. Sobol, and K.D. Bomben. *Handbook of X-ray Photoelectron Spectroscopy*. Physical Electronics, Inc., 1995.
- [91] J. C. Fuggle and N. Martensson. Core-level binding-energies in metals. *Journal of Electron Spectroscopy and Related Phenomena*, 21(3):275–281, 1980.

-
- [92] J. Stohr. *NEXAFS Spectroscopy*. Springer, 1992.
- [93] M. Bohringer, K. Morgenstern, W.-D. Schneider, R. Berndt, F. Mauri, A. De Vita, and R. Car. Two-dimensional self-assembly of supramolecular clusters and chains. *Phys. Rev. Lett.*, 83:324 – 327, 1999.
- [94] T. Yokoyama, S. Yokoyama, T. Kamikado, Y. Okuno, and S. Mashiko. Selective assembly on a surface of supramolecular aggregates of controlled size and shape. *Nature*, 413:619 – 621, 2001.
- [95] J.V. Barth, J. Weckesser, C. Cai, P. Günter, L. Burgi, O. Jeandupeux, and K. Kern. Building supramolecular nanostructures at surfaces by hydrogen bonding. *Angew. Chem. Int. Ed.*, 39:1230–1234, 2000.
- [96] J.A. Theobald, N.S. Oxtoby, M.A. Phillips, N.R. Champness, and P.H. Beton. Controlling molecular deposition and layer structure with supramolecular surface assemblies. *Nature*, 424:1029 – 1031, 2003.
- [97] S. Stepanow, M. Lingenfelder, A. Dmitriev, H. Spillmann, E. Delvigne, N. Lin, X. Deng, C. Cai, J.V. Barth, and K. Kern. Steering molecular organization and host-guest interactions using tailor-made two-dimensional nanoporous coordination systems. *Nature Mat.*, 3:229–233, 2004.
- [98] J. V. Barth. Molecular architectonic on metal surfaces. *Annu. Rev. Phys. Chem.*, 58:375407, 2007.
- [99] J.V. Barth, J. Weckesser, G. Trimarchi, M. Vladimirova, A. De Vita, C. Cai, H. Brune, P. Gunter, and K. Kern. Stereochemical effects

-
- in supramolecular self-assembly at surfaces: 1D vs. 2D enantiomorphic ordering for PVBA and PEBA on Ag(111). *J. Am. Chem. Soc.*, 124:7991–8000, 2002.
- [100] A. Dmitriev, N. Lin, J. Weckesser, J.V. Barth, and K. Kern. Supramolecular assemblies of trimesic acid on a Cu(100) surface. *J. Phys. Chem. B*, 106:6907 – 6912, 2002.
- [101] T. Yokoyama, T. Kamikado, S. Yokoyama, and S. Mashiko. Conformation selective assembly of carboxyphenyl substituted porphyrins on Au(111). *J. Chem. Phys.*, 121:11993–11997, 2004.
- [102] C. Miller, P. Cuendet, and M. Gratzel. Adsorbed omega-hydroxy thiol monolayers on gold electrodes - evidence for electron-tunneling to redox species in solution. *Journal of Physical Chemistry*, 95(2):877–886, 1991.
- [103] A. Dmitriev, H. Spillmann, N. Lin, J.V. Barth, and K. Kern. Modular assembly of two-dimensional metal-organic coordination networks at a metal surface. *Angew. Chem. Int. Ed.*, 41:2670 – 2673, 2003.
- [104] S. Clair, S. Pons, H. Brune, K. Kern, and J.V. Barth. Mesoscopic metallosupramolecular texturing through hierarchic assembly. *Angew. Chem. Int. Ed.*, 44:7294, 2005.
- [105] S. Clair, S. Pons, S. Fabris, S. Baroni, H. Brune, K. Kern, and J.V. Barth. Monitoring two-dimensional coordination reactions: Directed assembly of Co-terephthalate nanosystems on Au(111). *J. Phys. Chem. B*, 110:5627, 2006.

-
- [106] A.P. Seitsonen, M. Lingenfelder, H. Spillmann, A. Dmitriev, S. Stepanow, N. Lin, K. Kern, and J.V. Barth. Density functional theory analysis of metallosupramolecular architecture at surfaces : The Fediterephthalate nanoarray on Cu(100). *J. Am. Chem. Soc.*, 126:5634–5635, 2006.
- [107] T. Kawai, H. Tanaka, and T. Nakagawa. Low dimensional self-organization of DNA-base molecules on Cu(111) surfaces. *Surf. Sci.*, 386:124 – 136, 1997.
- [108] R. Otero, M. Schock, L.M. Molina, E. Laegsgaard, I. Stensgaard, B. Hammer, and F. Besenbacher. Guanine quartet networks stabilized by cooperative hydrogen bonds. *Angew. Chem. Int. Ed.*, 44:2–6, 2004.
- [109] R. E. A. Kelly and L. N. Kantorovich. Planar nucleic acid base superstructures. *J. Mater. Chem.*, 16:1894–1905, 2006.
- [110] M. Preuss, W.G. Schmidt, and F. Bechstedt. Coulombic amino group-metal bonding: adsorption of adenine on Cu(110). *Phys. Rev. Lett.*, 94:236102, 2005.
- [111] L.M. Ghiringhelli, P. Schravendijk, and L. Delle Sitte. Adsorption of alanine on a Ni(111) surface: A multiscale modeling oriented density functional study. *Phys. Rev. B*, 74:035437, 2006.
- [112] B. Schade and J.-H. Fuhrhop. Amino acid networks. *New J. Chem.*, 22:97–104, 1998.

-
- [113] B. Dalhus and C.H. Görbitz. Crystal structures of hydrophobic amino acids: interaction energies of hydrogen-bonded layers revealed by *ab initio* calculations. *J. Mol. Struct. (Theochem)*, 675:47–52, 2004.
- [114] N. Banno, T. Nakanishi, M. Matsunaga, T. Asahi, and T. Osaka. Enantioselective crystal growth of leucine on a self-assembled monolayer with covalently attached leucine molecules. *J. Am. Chem. Soc.*, 126:428–429, 2004.
- [115] C.F.J. Faul and M. Antonietti. Ionic self-assembly: Facile synthesis of supramolecular materials. *Adv. Mater.*, 15:673–683, 2003.
- [116] B. Dalhus and C.H. Gorbitz. Molecular aggregation in selected crystalline 1:1 complexes of hydrophobic *D*- and *L*-amino acids. ii. the *D*-norleucine series. *Acta Cryst.*, C55:1105–1112, 1999.
- [117] O. Cavalleri, G. Gonella, S. Terreni, M. Vignolo, L. Floreano, A. Morgante, M. Canepa, and R. Rolandi. High resolution X-ray photoelectron spectroscopy of *L*-cysteine self-assembled films. *Phys. Chem. Chem. Phys.*, 6:4042, 2004.
- [118] O. Cavalleri, G. Gonella, S. Terreni, M. Vignolo, P. Pelori, L. Floreano, A. Morgante, M. Canepa, and R. Rolandi. High resolution XPS of the S 2p core level region of the *L*-cysteine/gold interface. *J. Phys. Cond. Matt.*, 16:S2477, 2004.
- [119] Hyperchem, 2002.

-
- [120] W. Thiel and A. A. Voityuk. Extension of MNDO to d orbitals: Parameters and results for the second-row elements and for the zinc group. *Journal of Physical Chemistry*, 100(2):616–626, 1996.
- [121] W. Thiel. Perspectives on semiempirical molecular orbital theory. *Advances in Chemical Physics*, Vol Xciii, 93:703–757, 1996.
- [122] N. L. Allinger. Conformational-analysis .130. MM2 - hydrocarbon force-field utilizing v1 and v2 torsional terms. *Journal of the American Chemical Society*, 99(25):8127–8134, 1977.
- [123] Y. Pennec, W. Auwarter, A. Schiffrin, A. Weber-Bargioni, A. Riemann, and J. V. Barth. Supramolecular gratings for tunable confinement of electrons on metal surfaces. *Nature Nanotechnology*, 2(2):99–103, 2007.
- [124] M.L. Merrick, W. Luo, and K.A. Fichthorn. Substrate-mediated interactions on solid surfaces: Theory, experiment and consequences for thin film morphology. *Prog. Surf. Sci.*, 72:117–134, 2003.
- [125] F. Silly, M. Pivetta, M. Ternes, F. Patthey, J.P. Pelz, and W.-D. Schneider. Creation of an atomic superlattice by immersing metallic adatoms in a two-dimensional electron sea. *Phys. Rev. Lett.*, 92:16101, 2004.
- [126] E.C.H. Sykes, P. Han, S.A. Kandel, K.F. Kelly, G.S. McCarty, and P.S. Weiss. Substrate-mediated interactions and intermolecular forces between molecules adsorbed on surfaces. *Acc. Chem. Res.*, 36:945–953, 2003.
- [127] R. Otero, Y. Naitoh, F. Rosei, P. Jiang, P. Thostrup, A. Gourdon, E. Laegsgaard, I. Stensgaard, Ch. Joachim, and F. Besenbacher. One-

- dimensional assembly and selective orientation of larder molecules on an O-Cu template. *Angew. Chem. Int. Ed.*, 43:2092 – 2095, 2004.
- [128] G. Gonella, S. Terreni, D. Cvetko, A. Cossaro, L. Mattera, O. Cavalleri, R. Rolandi, A. Morgante, L. Floreano, and Canepa M. Ultrahigh vacuum deposition of *L*-cysteine on Au(110) studied by high-resolution x-ray photoemission: From early stages of adsorption to molecular organization. *J. Phys. Chem. B*, 109:18003–18009, 2005.
- [129] A. Cossaro, S. Terreni, O. Cavalleri, M. Prato, D. Cvetko, A. Morgante, L. Floreano, and M. Canepa. Electronic and geometric characterization of the *L*-cysteine paired-row phase on Au(110). *Langmuir*, 22(26):11193–11198, 2006.
- [130] A. Kuhnle, L.M. Molina, T.R. Linderoth, B. Hammer, and F. Besenbacher. Growth of unidirectional rows of cysteine on Au(110)-(1 × 2) driven by adsorbate-substrate interactions. *Phys. Rev. Lett.*, 93:086101, 2004.
- [131] P. Lofgren, A. Krozer, J. Lausmaa, and B. Kasemo. Glycine on Pt(111): a TDS and XPS study. *Surf. Sci.*, 370:277–292, 1997.
- [132] E. Podstawka, Y. Ozaki, and L. M. Proniewicz. Part i: Surface-enhanced raman spectroscopy investigation of amino acids and their homodipeptides adsorbed on colloidal silver. *Applied Spectroscopy*, 58(5):570–580, 2004.
- [133] E. Podstawka, Y. Ozaki, and L. M. Proniewicz. Part ii: Surface-enhanced raman spectroscopy investigation of methionine containing

-
- fleterodipeptides adsorbed on colloidal silver. *Applied Spectroscopy*, 58(5):581–590, 2004.
- [134] H. Lee, M. S. Kim, and S. W. Suh. Raman-spectroscopy of sulfur-containing amino-acids and their derivatives adsorbed on silver. *Journal of Raman Spectroscopy*, 22(2):91–96, 1991.
- [135] K. Kaznatcheyev, A. Osanna, C. Jacobsen, O. Plashkevych, O. Vahtras, H.A Agren, V. Carravetta, and A.P. Hitchcock. Innershell absorption spectroscopy of amino acids. *J. Phys. Chem. A*, 106(13):3153–3168, 2002.
- [136] Y. Zubavichus, A. Shaporenko, M. Grunze, and M. Zharnikov. Inner-shell absorption spectroscopy of amino acids at all relevant absorption edges. *Journal of Physical Chemistry A*, 109(32):6998–7000, 2005.
- [137] J. Weckesser, A. De Vita, J.V. Barth, C. Cai, and K. Kern. Mesoscopic correlation of supramolecular chirality in one-dimensional hydrogen-bonded assemblies. *Phys. Rev. Lett.*, 87:096101, 2001.
- [138] S. Weigelt, Carsten Busse, L. Petersen, E. Rauls, B. Hammer, K.V. Gothelf, F. Besenbacher, and T. R. Linderoth. Chiral switching by spontaneous conformational change in adsorbed organic molecules. *Nature Mat.*, 5:112–117, 2005.
- [139] S. Clair, S. Pons, A.P. Seitsonen, H. Brune, K. Kern, and J.V. Barth. STM study of terephthalic acid self-assembly on Au(111): Hydrogen-bonded sheets on an inhomogenous substrate. *J. Phys. Chem. B*, 108:19392–19397, 2004.

-
- [140] K. Torii and Y. Iitaka. Crystal-structures of *L*-methionine and *L*-norleucine. *Acta Crystallographica Section A*, 28:S39–S39, 1972.
- [141] A. Schiffrin, A. Riemann, W. Auwärter, Y. Pennec, A. Weber-Bargioni, D. Cvetko, A. Cossaro, M. Alberto, and J. V. Barth. Zwitterionic self-assembly of *L*-methionine nanogratings on the Ag(111) surface. *Proceedings of the National Academy of Sciences of the United States of America*, 104(13):5279–5284, 2007.
- [142] N. Nilius, T. M. Wallis, and W. Ho. Development of one-dimensional band structure in artificial gold chains. *Science*, 297(5588):1853–1856, 2002.
- [143] C. F. Hirjibehedin, C. P. Lutz, and A. J. Heinrich. Spin coupling in engineered atomic structures. *Science*, 312(5776):1021–1024, 2006.
- [144] F. J. Himpsel, J. E. Ortega, G. J. Mankey, and R. F. Willis. Magnetic nanostructures. *Advances in Physics*, 47(4):511–597, 1998.
- [145] M.A. Nielsen and I.L. Chuang. *Quantum Computation and Quantum Information*. Cambridge University Press, Cambridge, 2000.
- [146] N.W. Ashcroft and N.D. Mermin. *Solid State Physics*. Holt, Rinehart and Winston, 1976.
- [147] Norbert Memmel. Monitoring and modifying properties of metal surfaces by electronic surface states. *Surface Science Reports*, 32(3-4):91–163, 1998.

-
- [148] M. F. Crommie, C. P. Lutz, and D. M. Eigler. Imaging standing waves in a 2-dimensional electron-gas. *Nature*, 363(6429):524–527, 1993.
- [149] G. A. Fiete and E. J. Heller. Colloquium: Theory of quantum corrals and quantum mirages. *Reviews of Modern Physics*, 75(3):933–948, 2003.
- [150] A. A. Correa, F. A. Reboredo, and C. A. Balseiro. Quantum corral wave-function engineering. *Physical Review B*, 71(3):035418, 2005.
- [151] H. C. Manoharan, C. P. Lutz, and D. M. Eigler. Quantum mirages formed by coherent projection of electronic structure. *Nature*, 403(6769):512–515, 2000.
- [152] J. Kliewer, R. Berndt, and S. Crampin. Controlled modification of individual adsorbate electronic structure. *Physical Review Letters*, 85(23):4936–4939, 2000.
- [153] K. F. Braun and K. H. Rieder. Engineering electronic lifetimes in artificial atomic structures. *Physical Review Letters*, 88(9):096801, 2002.
- [154] P. Avouris and I. W. Lyo. Observation of quantum-size effects at room-temperature on metal-surfaces with STM. *Science*, 264(5161):942–945, 1994.
- [155] A. Mugarza, A. Mascaraque, V. Perez-Dieste, V. Repain, S. Rousset, F. J. G. de Abajo, and J. E. Ortega. Electron confinement in surface states on a stepped gold surface revealed by angle-resolved photoemission. *Physical Review Letters*, 87(10):107601, 2001.

-
- [156] S. Shiraki, H. Fujisawa, M. Nantoh, and M. Kawai. Confining barriers for surface state electrons tailored by monatomic Fe rows on vicinal Au(111) surfaces. *Physical Review Letters*, 92(9):096102, 2004.
- [157] F. Baumberger, M. Hengsberger, M. Muntwiler, M. Shi, J. Krem-pasky, L. Patthey, J. Osterwalder, and T. Greber. Localization of surface states in disordered step lattices. *Physical Review Letters*, 92(19):196805, 2004.
- [158] Y. Hasegawa and P. Avouris. Direct observation of standing-wave formation at surface steps using scanning tunneling spectroscopy. *Physical Review Letters*, 71(7):1071–1074, 1993.
- [159] H. Jensen, J. Kroger, R. Berndt, and S. Crampin. Electron dynamics in vacancy islands: Scanning tunneling spectroscopy on Ag(111). *Physical Review B*, 71(15):155417, 2005.
- [160] V. S. Stepanyuk, N. N. Negulyaev, L. Niebergall, R. C. Longo, and P. Bruno. Adatom self-organization induced by quantum confinement of surface electrons. *Physical Review Letters*, 97(18):186403, 2006.
- [161] L. Gross, F. Moresco, L. Savio, A. Gourdon, C. Joachim, and K. H. Rieder. Scattering of surface state electrons at large organic molecules. *Physical Review Letters*, 93(5):056103, 2004.
- [162] F. Baumberger, T. Greber, B. Delley, and J. Osterwalder. Tailoring confining barriers for surface states by step decoration: CO/vicinal Cu(111). *Physical Review Letters*, 88(23):–, 2002.

-
- [163] K. Morgenstern, K. F. Braun, and K. H. Rieder. Surface-state depopulation on small Ag(111) terraces. *Physical Review Letters*, 89(22):226801, 2002.
- [164] P. T. Sprunger, L. Petersen, E. W. Plummer, E. Laegsgaard, and F. Besenbacher. Giant Friedel oscillations on the beryllium(0001) surface. *Science*, 275(5307):1764–1767, 1997.
- [165] M. Hansmann, J. I. Pascual, G. Ceballos, H. P. Rust, and K. Horn. Scanning tunneling spectroscopy study of Cu(554): Confinement and dimensionality at a stepped surface. *Physical Review B*, 67(12):121409, 2003.
- [166] U. Schlickum, R. Decker, F. Klappenberger, G. Zoppellaro, S. Klyatskaya, M. Ruben, I. Silanes, A. Arnau, K. Kern, H. Brune, and J.V. Barth. Metal-organic honeycomb nanomeshes with tunable cavity size. *Nano Lett.*, 7(12):3813–3817, 2007.
- [167] H. F. Ding, V. S. Stepanyuk, P. A. Ignatiev, N. N. Negulyaev, L. Niebergall, M. Wasniowska, C. L. Gao, P. Bruno, and J. Kirschner. Self-organized long-period adatom strings on stepped metal surfaces: Scanning tunneling microscopy, *ab initio* calculations, and kinetic Monte Carlo simulations. *Physical Review B*, 76(3):033409, 2007.
- [168] J. Repp, F. Moresco, G. Meyer, K. H. Rieder, P. Hyldgaard, and M. Persson. Substrate mediated long-range oscillatory interaction between adatoms: Cu/Cu(111). *Physical Review Letters*, 85(14):2981–2984, 2000.

-
- [169] G. Hormandinger. Imaging of the Cu(111) surface-state in scanning tunneling microscopy. *Physical Review B*, 49(19):13897–13905, 1994.
- [170] G. Hormandinger and J. B. Pendry. Interaction of surface-states with rows of adsorbed atoms and other one-dimensional scatterers. *Physical Review B*, 50(24):18607–18620, 1994.
- [171] V. S. Stepanyuk, A. N. Baranov, D. V. Tsvilin, W. Hergert, P. Bruno, N. Knorr, M. A. Schneider, and K. Kern. Quantum interference and long-range adsorbate-adsorbate interactions. *Physical Review B*, 68(20):205410, 2003.
- [172] N. N. Negulyaev, V. S. Stepanyuk, L. Niebergall, W. Hergert, H. Fangohr, and P. Bruno. Self-organization of Ce adatoms on Ag(111): A kinetic Monte Carlo study. *Physical Review B*, 74(3):035421, 2006.
- [173] N. N. Negulyaev, V. S. Stepanyuk, W. Hergert, H. Fangohr, and P. Bruno. Effect of the long-range adsorbate interactions on the atomic self-assembly on metal surfaces. *Surface Science*, 600(5):L58–L61, 2006.
- [174] Michael L. Merrick, Weiwei Luo, and Kristen A. Fichthorn. Substrate-mediated interactions on solid surfaces: theory, experiment, and consequences for thin-film morphology. *Progress in Surface Science*, 72(5-8):117–134, 2003.
- [175] A. Bogicevic, S. Ovesson, P. Hyldgaard, B. I. Lundqvist, H. Brune, and D. R. Jennison. Nature, strength, and consequences of indirect adsorbate interactions on metals. *Physical Review Letters*, 85(9):1910–1913, 2000.

-
- [176] W. Auwarter, A. Weber-Bargioni, A. Riemann, A. Schiffrin, O. Groning, R. Fasel, and J. V. Barth. Self-assembly and conformation of tetrapyrrolyl-porphyrin molecules on Ag(111). *Journal of Chemical Physics*, 124(19), 2006.
- [177] W. Auwarter, F. Klappenberger, A. Weber-Bargioni, A. Schiffrin, T. Strunskus, C. Woll, Y. Pennec, A. Riemann, and J. V. Barth. Conformational adaptation and selective adatom capturing of tetrapyrrolyl-porphyrin molecules on a copper (111) surface. *Journal of the American Chemical Society*, 129(36):11279–11285, 2007.
- [178] S. Stepanow, N. Lin, F. Vidal, A. Landa, M. Ruben, J. V. Barth, and K. Kern. Programming supramolecular assembly and chirality in two-dimensional dicarboxylate networks on a Cu(100) surface. *Nano Letters*, 5(5):901–904, 2005.
- [179] S. M. Barlow, S. Louafi, D. Le Roux, J. Williams, C. Muryn, S. Haq, and R. Raval. Polymorphism in supramolecular chiral structures of R- and S-alanine on Cu(110). *Surface Science*, 590(2-3):243–263, 2005.
- [180] M. Lingenfelder, G. Tomba, G. Costantini, L. C. Ciacchi, A. De Vita, and K. Kern. Tracking the chiral recognition of adsorbed dipeptides at the single-molecule level. *Angewandte Chemie-International Edition*, 46(24):4492–4495, 2007.
- [181] S. M. Barlow, K. J. Kitching, S. Haq, and N. V. Richardson. A study of glycine adsorption on a Cu(110) surface using reflection absorption infrared spectroscopy. *Surface Science*, 401(3):322–335, 1998.

-
- [182] J. H. Kang, R. L. Toomes, M. Polcik, M. Kittel, J. T. Hoeft, V. Efsthathiou, D. P. Woodruff, and A. M. Bradshaw. Structural investigation of glycine on Cu(100) and comparison to glycine on Cu(110). *Journal of Chemical Physics*, 118(13):6059–6071, 2003.
- [183] D. I. Sayago, M. Polcik, G. Nisbet, C. L. A. Lamont, and D. P. Woodruff. Local structure determination of a chiral adsorbate: alanine on Cu(110). *Surface Science*, 590(1):76–87, 2005.
- [184] Q. Chen, D. J. Frankel, and N. V. Richardson. Chemisorption induced chirality: glycine on Cu(110). *Surface Science*, 497(1-3):37–46, 2002.
- [185] X. Zhao. Fabricating homochiral facets on Cu(001) with *L*-lysine. *J. Am. Chem. Soc.*, 122(50):12584–12585, 2000.
- [186] K. Kanazawa, A. Taninaka, O. Takeuchi, and H. Shigekawa. What orchestrates the self-assembly of glycine molecules on Cu(100)? *Physical Review Letters*, 99(21):216102, 2007.
- [187] J. I. Pascual, J. V. Barth, G. Ceballos, G. Trimarchi, A. De Vita, K. Kern, and H. P. Rust. Mesoscopic chiral reshaping of the Ag(110) surface induced by the organic molecule PVBA. *Journal of Chemical Physics*, 120(24):11367–11370, 2004.
- [188] R. B. Rankin and D. S. Sholl. Assessment of heterochiral and homochiral glycine adlayers on Cu(110) using density functional theory. *Surface Science*, 548(1-3):301–308, 2004.
- [189] R. B. Rankin and D. S. Sholl. Structure of enantiopure and racemic alanine adlayers on Cu(110). *Surface Science*, 574(1):L1–L8, 2005.

-
- [190] M. Kirschner and T. Mitchison. Beyond self-assembly - from microtubules to morphogenesis. *Cell*, 45(3):329–342, 1986.
- [191] T. Misteli. The concept of self-organization in cellular architecture. *Journal of Cell Biology*, 155(2):181–185, 2001.
- [192] T. A. Jung, R. R. Schlittler, and J. K. Gimzewski. Conformational identification of individual adsorbed molecules with the STM. *Nature*, 386(6626):696–698, 1997.
- [193] T. Yokoyama, S. Yokoyama, T. Kamikado, and S. Mashiko. Nonplanar adsorption and orientational ordering of porphyrin molecules on Au(111). *Journal of Chemical Physics*, 115(8):3814–3818, 2001.
- [194] F. Klappenberger, M. E. Canas-Ventura, S. Clair, S. Pons, U. Schlickum, Z. R. Qu, H. Brune, K. Kern, T. Strunskus, C. Woll, A. Comisso, A. De Vita, M. Ruben, and J. V. Barth. Conformational adaptation in supramolecular assembly on surfaces. *Chemphyschem*, 8(12):1782–1786, 2007.
- [195] M. Furukawa, H. Tanaka, K. Sugiura, Y. Sakata, and T. Kawai. Fabrication of molecular alignment at the specific sites on Cu(111) surfaces using self-assembly phenomena. *Surface Science*, 445(1):L58–L63, 2000.
- [196] M. A. Lingenfelder, H. Spillmann, A. Dmitriev, S. Stepanow, N. Lin, J. V. Barth, and K. Kern. Towards surface-supported supramolecular architectures: tailored coordination assembly of 1,4-

- benzenedicarboxylate and Fe on Cu(100). *Chemistry-a European Journal*, 10(8):1913–1919, 2004.
- [197] F. Rosei, M. Schunack, Y. Naitoh, P. Jiang, A. Gourdon, E. Laegsgaard, I. Stensgaard, Ch. Joachim, and F. Besenbacher. Properties of large organic molecules at surfaces. *Prog. Surf. Sci.*, 71:95–146, 2003.
- [198] L. L. Liu and K. J. Franz. Phosphorylation-dependent metal binding by alpha-synuclein peptide fragments. *Journal of Biological Inorganic Chemistry*, 12(2):234–247, 2007.
- [199] D. Wang, Q. M. Xu, L. J. Wan, C. L. Bai, and G. Jin. Adsorption of enantiomeric and racemic tyrosine on Cu(111): A scanning tunneling microscopy study. *Langmuir*, 19(6):1958–1962, 2003.
- [200] M. Nyberg, J. Hasselstrom, O. Karis, N. Wassdahl, M. Weinelt, A. Nilsson, and L. G. M. Pettersson. The electronic structure and surface chemistry of glycine adsorbed on Cu(110). *Journal of Chemical Physics*, 112(12):5420–5427, 2000.
- [201] Y. Zubavichus, O. Fuchs, L. Weinhardt, C. Heske, E. Umbach, J. D. Denlinger, and M. Grunze. Soft x-ray-induced decomposition of amino acids: An XPS, mass spectrometry, and NEXAFS study. *Radiation Research*, 161(3):346–358, 2004.
- [202] Y. Zubavichus, M. Zharnikov, A. Shaporenko, O. Fuchs, L. Weinhardt, C. Heske, E. Umbach, J. D. Denlinger, and M. Grunze. Soft x-ray induced decomposition of phenylalanine and tyrosine: A comparative study. *Journal of Physical Chemistry A*, 108(20):4557–4565, 2004.

-
- [203] J. Boese, A. Osanna, C. Jacobsen, and J. Kirz. Carbon edge XANES spectroscopy of amino acids and peptides. *Journal of Electron Spectroscopy and Related Phenomena*, 85(1-2):9–15, 1997.
- [204] J. Hasselstrom, O. Karis, M. Weinelt, N. Wassdahl, A. Nilsson, M. Nyberg, L. G. M. Pettersson, M. G. Samant, and J. Stohr. The adsorption structure of glycine adsorbed on Cu(110); comparison with formate and acetate/Cu(110). *Surface Science*, 407(1-3):221–236, 1998.
- [205] B. C. Stipe, H. A. Rezaei, and W. Ho. Localization of inelastic tunneling and the determination of atomic-scale structure with chemical specificity. *Physical Review Letters*, 82(8):1724–1727, 1999.
- [206] M. Moskovits. Surface-enhanced spectroscopy. *Reviews of Modern Physics*, 57(3):783–826, 1985.
- [207] H. C. Kang, J. Maser, G. B. Stephenson, C. Liu, R. Conley, A. T. Macrander, and S. Vogt. Nanometer linear focusing of hard x-rays by a multilayer Laue lens. *Physical Review Letters*, 96(12):127401, 2006.
- [208] H. Mimura, H. Yumoto, S. Matsuyama, Y. Sano, K. Yamamura, Y. Mori, M. Yabashi, Y. Nishino, K. Tamasaku, T. Ishikawa, and K. Yamauchi. Efficient focusing of hard x-rays to 25 nm by a total reflection mirror. *Applied Physics Letters*, 90(5):051903, 2007.
- [209] E. Betzig and R. J. Chichester. Single molecules observed by near-field scanning optical microscopy. *Science*, 262(5138):1422–1425, 1993.

-
- [210] J. Repp, G. Meyer, F. E. Olsson, and M. Persson. Controlling the charge state of individual gold adatoms. *Science*, 305(5683):493–495, 2004.
- [211] J. Repp, G. Meyer, S. M. Stojkovic, A. Gourdon, and C. Joachim. Molecules on insulating films: Scanning tunneling microscopy imaging of individual molecular orbitals. *Physical Review Letters*, 94(2):026803, 2005.
- [212] J. Repp, G. Meyer, S. Paavilainen, F. E. Olsson, and M. Persson. Imaging bond formation between a gold atom and pentacene on an insulating surface. *Science*, 312(5777):1196–1199, 2006.